

Università degli studi di Napoli

“Federico II”

Dipartimento di Ingegneria Industriale



Dottorato di Ricerca in

Ingegneria Aerospaziale, Navale e della Qualità

XXVI Ciclo

Tesi di Dottorato

***“Calibration activity in support of GIADA, part of the
ESA/Rosetta Spacecraft payload.”***

Candidato

Roberto Sordini

Tutor

Ing. V. Della Corte

Prof.ssa A. Rotundi

Coordinatore

Prof. L. de Luca

Anno Accademico

2013- 2014

| | |
|---|-----------|
| 1. Abstract | 3 |
| 2. The ESA/Rosetta mission | 7 |
| 2.1 Comets and their exploration | 9 |
| 2.2 The Rosetta spacecraft | 16 |
| 2.3 The Target | 20 |
| 3. GIADA - Grain Impact Analyser and Dust Accumulator – on board Rosetta | 22 |
| 3.1 GIADA contribution to the scientific goal of the Rosetta space mission | 22 |
| 3.2 GIADA: instrument description | 23 |
| 3.2.1 Grain Detection System | 24 |
| The GDS Proximity Electronic | 29 |
| The working principle | 30 |
| 3.2.2 Impact Sensor | 31 |
| The IS Proximity Electronic | 33 |
| The working principle | 35 |
| 3.2.3 Micro-Balances System | 36 |
| 3.3 Main Electronics | 37 |
| 4. GIADA state of health during the Rosetta Cruise Phase | 41 |
| 4.1 The Rosetta Cruise Phase | 41 |
| 4.2 Payload Checkouts Analysis | 43 |
| 4.2.1 Cover activation analysis | 44 |
| 4.2.2 Data Analysis | 48 |
| Micro Balances System | 49 |
| Impact Sensor subsystem | 52 |
| Grain Detection System | 53 |
| GDS+IS Cruise Phase events | 57 |
| 5. Calibration Activity on GIADA Proto-Flight Model | 58 |
| 5.1 GIADA Calibration Setup | 60 |
| 5.1.1 The Electrostatic Micromanipulator | 61 |
| 5.1.2 Working Principle of the Electrostatic Micromanipulator | 62 |
| 5.1.3 Electrostatic Micromanipulator Tests | 63 |
| 5.2 Preparatory analyses on the IS and GDS | 66 |
| 5.2.1 Analyses on the IS sub-system | 67 |
| 5.2.2 The Time Delays Map | 73 |
| 5.2.3 Preparatory activity on the GDS sub-system | 79 |
| 5.3 Calibration of GDS using cometary dust analogues | 84 |
| 6. Conclusions | 88 |
| 7. REFERENCES | 92 |

1. Abstract

Comets formed about 4.6 billion years ago from the Pre-Solar Nebula and spent most of their existence in the outer and colder regions of the Solar System, beyond the Neptune's orbit. These small celestial bodies, with masses ranging between 10^{14} g and 10^{21} g, could be considered the cosmo-chemical record of the primordial Solar Nebula. Therefore studying comets means investigating the physico-chemical properties of the material that formed the Solar System. With the aim of exploring the nature and the composition of these fascinating objects, several cometary space missions have been realized since the 1980's. The first comet to be observed by a space probe, the NASA/ISEE 3 spacecraft, was comet 21P/Giacobini-Zimmer in 1985. One year after comet 1P/Halley was deeply studied by five different space probes: Vega 1 and Vega 2 (Soviet Union), Sakigake and Suisei (Japan), and GIOTTO (ESA). More recently two NASA missions, Deep Space 1 and Stardust, observed comet 19P/Borrelly and 81P/Wild 2, respectively, showing a considerable and unexpected mineral diversity in these objects. Despite the improvements provided by all these space missions, our knowledge about cometary nuclei, comae and activity remains rather primitive in many aspects.

An incredible opportunity to make a critical step forward in cometary science and more in general in the knowledge of the Solar System origin is represented by the ESA space mission, Rosetta (Chapter 1). Thanks to the encounter with 67P/Churyumov-Gerasimenko (67P/CG), Rosetta will allow an extensive study of the mineral variety present in this Jupiter Family comet. Moreover this mission, for the first time, will undertake a comet long-term monitoring at close quarters along its orbit, allowing the study of the comet behaviour from the moment the cometary activity will start, when it will reach its maximum at perihelion and after it when it will slowly decrease.

Among the instruments mounted on-board Rosetta, there is the Grain Impact Analyser and Dust Accumulator (GIADA) developed with the aim of studying the cometary dust environment, the evolution of the dust flow and the dynamics of each single grain as a function of time and position, i.e. at variable distances of the spacecraft from the nucleus and of the comet from the Sun.

GIADA is designed as a single instrument composed of three different detection sub-systems:

2. Grain Detection System (GDS): detects each incoming grain, providing its optical equivalent size and measuring its speed, without affecting its dynamical properties.
3. Impact Sensor (IS): measures the momentum released from each grain impacting its sensitive surface.

4. Micro-Balances System (MBS): a network of five Quartz Crystal Microbalances, pointing toward different directions, that measure the cumulative dust deposition in time and monitor the dust flux ejected from the comet.

Thanks to its features, described in Chapter 2, GIADA will contribute to the achievement of two of the five Main Goals assigned to the Rosetta space mission:

- Define the physical properties and interrelation of volatiles and refractories in a cometary nucleus;
- Study the development of cometary activity and processes in the surface layer of the nucleus and in the inner coma (dust-gas interaction).

Rosetta was launched on the 2nd March 2004 and will reach, at a distance of 4 AU from the Sun, the comet 67P/CG on May 2014, after a long trek lasted 10 years around the Sun. In order to limit power and fuel consumption, and to minimise operating costs, Rosetta was put in hibernation on the 8th of January 2011. The seven years after launch and prior to hibernation are called Cruise Phase. During the Cruise Phase 13 Payload Checkouts (PCs) have been executed in order to verify the instruments functionalities and to perform the maintenance. GIADA detection sub-systems were switched on to monitor their health state and verify their performances. The results of the analysis of the data collected by GIADA during these tests, reported in Chapter 3, show that GIADA functionalities and performances have maintained their nominal behaviour; only the cover mechanism showed a non-nominal behaviour, which had a small impact on the microbalance sub-system: contamination deposited on the QCM because of the cover remained open caused a small decrease of their dynamical range. This will not affect the GIADA measurement capability during the Rosetta comet encounter and escort phase.

Rosetta has awakened from hibernation on the 20th January 2014 and now its payloads are undergoing the post-hibernation commissioning, a phase devoted to the instruments re-activation-maintenance and checkout activities in preparation to the rendez-vous with comet 67P/CG. GIADA has successfully executed its first post-hibernation commissioning on the 27th March 2014.

In preparation to comet encounter, the GIADA Team planned an extended calibration activity (Chapter 4) devoted to create a database of the sub-systems response to different kind of cometary dust analogue grains (composition, mineralogy, ice and carbon coatings) that will be used to support the analysis of the data that GIADA will collect during the comet phase. This activity was planned taking into account the new knowledge on cometary dust composition reached after the

NASA/Stardust space mission. In order to well characterize the instrument responsivity with respect to realistic cometary analogue materials, some dust samples were prepared, taking into account the GIADA sub-systems sensitivities (GDS and IS), in four distinct size classes: $20 \mu\text{m} < \emptyset < 50 \mu\text{m}$, $50 \mu\text{m} < \emptyset < 100 \mu\text{m}$, $100 \mu\text{m} < \emptyset < 250 \mu\text{m}$ and $250 \mu\text{m} < \emptyset < 500 \mu\text{m}$. Single grains of these selected materials were shot into the GIADA Proto Flight Model, i.e. the spare of the instrument on board Rosetta operating in a clean room in our laboratory, with velocities in the range $1\text{-}100 \text{ms}^{-1}$. In order to capture, manipulate and shoot these small grains, an innovative Electrostatic Micromanipulator has been developed. The use of this tool resulted to be very useful during the calibration activities. In addition, two new empirical methods were developed with the aim to improve the capability of reconstructing the IS impact position and the GDS crossing position of each single grain entering into GIADA. These are key issues to scale the signal detected by the two sub-systems using the sensitivity maps measured during the pre-launch calibrations. The method developed for the GDS measurements was used during the present calibration activity with cometary dust analogues that led to the assembly of the calibration curves for each different material.

In the present thesis we illustrate the work performed during the three years of PhD course, which represent a significant step forward within the GIADA project. The performed work will critically contribute to make GIADA performances, data acquisition and reduction a success.

*If science teaches us anything,
it teaches us to accept our failures,
as well as our success,
with quiet dignity and grace.
Gene Wilder*

2. The ESA/Rosetta mission

The International Rosetta space Mission, which was approved in 1993 by the "Science Programme Committee" of the European Space Agency (ESA), was defined as planetary mission Cornerstone in the ESA long-term program Horizon 2000 (Bonnet, 1985). We can consider Rosetta the following step of the GIOTTO space missions, the first successful ESA mission, launched toward the comet 1P/Halley (Reinhard, 1986). Rosetta was launched on the 1st March 2004 with an Ariane 5 rocket from the Guyana Space Center, in Kourou (French Guyana). The principal aim of Rosetta is to investigate the origin of the Solar System, by means of an in depth study of the 67P/Churyumov-Gerasimenko (67P/CG) coma and nucleus.

The name of the Mission derives from the Rosetta Stone, discovered in 1799 in Egypt.

On this granodiorite stele was found the text of a decree, issued at Memphis in 196 BC on behalf of King Ptolemy V, written in three different languages: Ancient Egyptian hieroglyphs, Demotic and Ancient Greek. The presence of the same text in three different languages, one of which, the ancient Greek, well known, provided the key to the modern understanding of Egyptian hieroglyphs. In analogy with what Rosetta Stone has been represented in the knowledge of the ancient civilization, the ESA's Rosetta space mission will shed light on the origin and composition of the oldest "building blocks" of our Solar System: the comets.

The Rosetta probe has the rendez-vous with the comet 67P/CG in May 2014 when will start a critical series of manoeuvres that will steadily bring Rosetta in line with the comet. The approaching Rosetta trajectory (Figure 1) will allow a passage at a distance of approximately 50 000 km from the comet with a relative velocity of 800 m/s. Deep space manoeuvres are planned to further reduce Rosetta's relative velocity to 1 m/s at about 100 km from the comet on the 6th August 2014 when the close orbits phase will start for the comet nucleus characterization (see Table 1). From mid-August to late September, Rosetta will be in the Global Mapping Phase and then to the Close Observation Phase to perform accurate nucleus surface observations dedicated to the landing selection site. The selected landing sites will be announced on the 30th of September 2014. The Lander delivery is planned for the 11th of November 2014 when the comet will be at about 3AU from the Sun. Once anchored to the surface of the comet, the Lander will start its First Science Sequence (FSS) using only the primary battery for at least about 60 hours. After this primary phase Philae will use the solar panels to recharge the batteries in order to perform additional measurement periods, each one lasting about 60 hours. During the FSS the Rosetta Orbiter will be in an optimized

orbit to receive the data transmitted from the lander to be transferred to the Earth, such a service will be guaranteed until the lander will be operative.

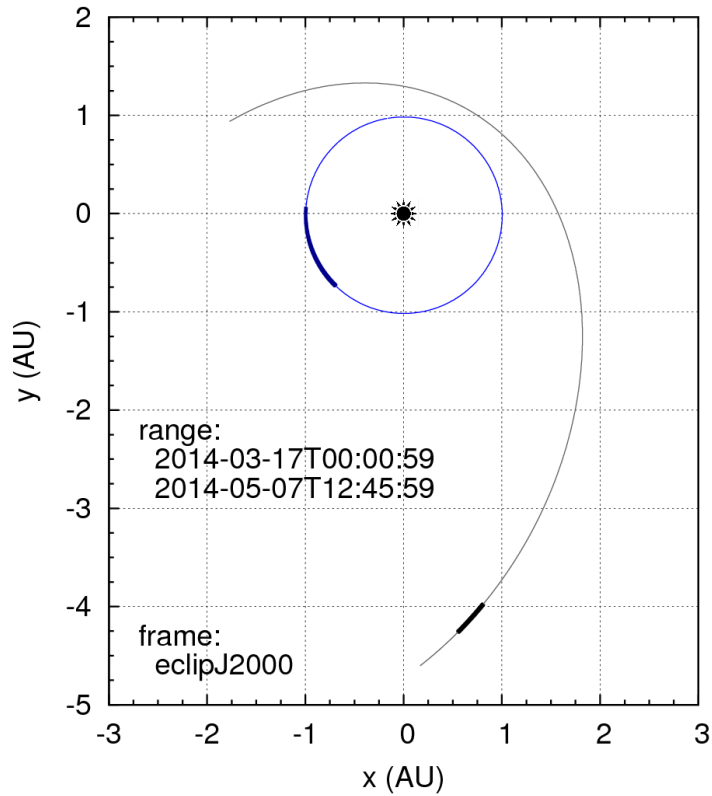


Figure 1: Rosetta (black) and Earth (blue) Orbit before the rendez-vous with the comet 67P/CG.

Once the phase linked to the primary Lander mission is completed, the Rosetta Orbiter will begin the Extended Monitoring Phase, fully dedicated to monitor the nucleus and the active regions, the jets of gas and dust, to analyse gas, dust and plasma in the inner coma from the beginning of the comet activity till its high peak, expected in August 2015 when the comet will achieve its perihelion. The end of this escort phase coincides with the nominal end of the mission, scheduled for the 31st of December 2015. In Table 1 are reported the mission phases defined for the comet phase.

| Mission Phase | Description |
|--|---|
| Near Comet Drift (NCD) | Relative distance Comet-Spacecraft reduced from ca 10^6 km to 10^5 km, relative velocity reduced from ca 780 m/s to 100 m/s |
| Far Approach Trajectory (FAT) | Relative distance reduced to ca 2000 km, relative speed reduced to ca 3 m/s |
| Close Approach Trajectory (CAT) | Used to enter in the sphere of influence of the comet and perform its characterization (typically 100 km distance and relative speed 0.8 m/s) Potential landing areas can already be identified in this phase. This phase will also be designed such that observations at relatively small phase angles (ca 30-40 deg) and distance (ca 50 km) will be performed with the aim of producing high resolution DTMs. This will be used for the ranking of the identified landing sites. |
| Transition to Global Mapping (TGM) | Intermediate phase used to set spacecraft in proper comet orbit, relative speed 0.3 m/s. |
| Global Mapping Phase (GMP) | Orbital phase used to perform a global mapping of comet surface, typically 30-20 km radius orbit, relative speed 0.3 m/s |
| Close Observation Phase (COP) | Orbital phase used to perform more detailed observation and accurate analysis of the top ranked potential landing areas. The feasibility of orbits with a radius equal or lower than 20 km is not confirmed by the navigation analysis when assuming a high comet activity level; exceptional navigation measures could be taken for unique cases as the lander delivery. The actual orbit strategy will be defined only after having flown the GMP and will aim at granting access to a minimum orbital radius of 10 km. |
| Separation, Descent and Landing (SDL) | Mission phase dedicated to landing preparation, execution, and the First Science Sequence (FSS, primary Lander mission) with the link to next phase. Sun distance 3 AU. |
| Extended Monitoring Phase (EMP) | Post landing phase fully dedicated to comet monitoring |

Table 1: Rosetta Space Mission phases defined by ESA.

2.1 Comets and their exploration

Comets can be considered the most fascinating objects in the Solar System. Since ancient times, they have intrigued and attracted the mankind. The spectacle created by a comet that crosses the dark night sky and the inability to predict their appearance have helped to create a mystery aura and superstition around them, whereby their appearance was often associated to positive or negative

events, as documented by numerous ancient documents. For centuries, astronomers recorded their appearance without being able to determine whether comets were atmospheric effects or interplanetary objects.

The Danish astronomer Tycho Brahe obtained the first scientific result on the study of comets in the sixteenth century. Studying comet C/1577 V1 he established that its horizontal parallax was smaller than 15 arc-minutes, therefore the comet was orbiting at a distance greater with respect to the Moon orbit. This demonstrated definitively the interplanetary nature of comets. The formulation of the gravitational theory by Isaac Newton, published in the seventeenth century in *Principia*, allowed the English astronomer Edmond Halley to calculate the orbits of some comets and he demonstrated that one of them, comet P1/1682 Q1 had a periodic nature: returned periodically at close distances to the Sun every 76 years. This periodicity was confirmed in 1758 when, as predicted by Halley, the German astronomer Johann Georg Palitzsch observed this comet. In honour to the scientist who predicted its return, this periodic comet became famous as the "Halley's Comet".

The second comet recognized as periodic was the "Encke's Comet" (1821), named after its discoverer, the German mathematician and physicist Johann Franz Encke. Comet "2P/Encke" has the shortest known period, about 3.3 years, so it has appeared the greatest number of times since 1786 with respect to any other comet. Studying its short orbit it was found out that comet 2P/Encke was reaching its perihelion about 0.1 days in advance every return. This aspect was not simply explainable considering the planetary perturbations. At the beginning of the nineteenth century the German mathematician Friedrich Wilhelm Bessel developed a theory according to which the brightness of a comet would flow from the evaporation of a solid object. The non-gravitational forces acting on comet 2P/Encke were the result of thrust caused by jet subject to this evaporation (Bessel 1936). Therefore comet 2P/Encke was the first one for which it was found that the orbit was influenced by non-gravitational forces.

A significant step forward in cometary science occurred in the period 1950-1951. Indeed in 1950 Fred Lawrence Whipple proposed that the nucleus of a comet was basically a "dirty snowball" (Whipple, 1950). This model describes the nucleus of a comet as a cluster of rocks, dust and ice. In this model the presence of the gasses is due to the sublimation of the ice occurring with the approaching of the comet to the Sun and the resultant increase of nucleus temperature. The ices sublimation involves also the release of dust grain from the nucleus. This model was widely accepted, because provided the explanation for a series of cometary phenomena observed (Festou et al., 2004):

- The high gas production rates, e.g. 200 Kg/s of C₂ for 1P/Halley (measured by Wurm in 1943), not justified by the desorption phenomenon;
- The irregular coma activity, e.g. the presence of jets;
- The presence of non-gravitational forces, due to gas outflow, affecting the orbital motion;
- The ability of the comets to survive despite the repeated passages near the Sun;
- Comets are the sources of meteor streams.

The presence of ice in comet nuclei suggested that they might have formed in the coldest regions of the Solar System. In 1950 the Dutch astronomer Jan Hendrik Oort, using observational results, predicted the existence of a vast cloud of comets orbiting in a region at about 50.000 UA from the Sun, or at about halfway to the nearest star (Oort, 1950). Oort estimated that this source of comets had to have a mass of about 10^{24} kg, containing approximately 2×10^{11} comets. This theorized region became known as the “Oort cloud”.

In 1951 the American astronomer Gerard Kuiper hypothesized the existence of a region, a belt, external to the one in which the planets were formed, where objects similar to comets resided. This belt would be formed early in the evolution of the Solar System. Kuiper suggested that this belt of inactive comets was beyond the orbits of the giant planets, between 30 and 100 AU from the Sun. The existence of this region was confirmed in 1992, when David C. Jewitt and Jane X. Luu observed the first trans-Neptunian object 1992QB1 (Jewitt and Luu, 1993). This region, now known as the “Kuiper Belt”, is the source of comets that orbit around the Sun with an orbital period relatively short, $T < 200$ years, so they are called short period comets. Comets belonging to the Oort Cloud are, instead, defined as long-period comets, $T > 200$ years. The orbits of the bodies that populate both regions are very unstable and can be perturbed by the external planets, in the case of Kuiper belt, or by gravitational interactions with a star, in the case of the Oort cloud. These interactions capture the comet and place it on an orbit with high eccentricity that runs through the inner Solar System.

Both the Oort Cloud and the Kuiper Belt have been formed about 4.6 billion years ago, in the early proto-Solar Nebula. So, the comets were born from the same rotating nebula that formed the Solar System and have spent most of their existence in its colder outer regions.

These primitive small bodies are characterized by a mass between 10^{14} g and 10^{21} g. When a comet approaches the Sun, the nucleus heats up and the ice sublimates dragging solid particles (ranging in size from few μ m to few cm). This process produces a diffuse coma of dust and gasses (Figure 2). When the comet starts to produce the coma, the gas begin to absorb ultraviolet radiation and

becomes fluorescent. This fluorescence, generally, becomes significant at about 5 AU from the Sun (Doody and Stephan, 1993).

Due to the absorption of ultraviolet radiation, chemical processes are triggered, leading the release of hydrogen that escapes to the gravity of the comet and create a hydrogen envelope. The dust particles, expanded in the coma, are accelerated by solar radiation pressure¹ in the antisolar direction.

Therefore, the dust moves along orbits whose semi-major axes increases progressively. This implies a decrease of their Keplerian speed with respect to the nucleus and the consequent formation of a *Dust Tail* or *Type Tails II*. Since the effectiveness of the radiation pressure is a function of surface-to-mass ratio of the individual grains, these particles are arranged in the tail according to the mass and dimensions.



Figure 2: Comet Hale-Bopp image taken by Loke Kun Tan on March 30, 1997 from the Red Rock Canyon Park in California. The Coma, the Ion Tail (bluish color) and the Dust Tail are distinguished.

The *Ions Tail (Type Tails I)* is formed closer to the Sun (<1.5 AU), by ionized molecules and radicals present in the coma, which interact with the charged particles of the solar wind (Biermann, 1951). The solar magnetic field interacts with these ions by means of the Lorentz force: this force accelerates the ions in the opposite direction to the Sun so rapidly as to produce a nearly linear tail. Due to the presence of CO^+ ions, the plasma tails appear of bluish colour.

As explained before, the large distances from the Sun and the low temperatures at which comets

¹ The Solar radiation pressure is the largest non-gravitational force (Sengoku, 1998) and is the flux of momentum carried by solar photons per unit area and per unit of time.

reside imply that their constituent elements are the less thermally processed elements in the Solar System. Therefore the comets can be considered the cosmo-chemical record of the primordial Solar Nebula; studying them means investigating the composition of the early Solar System.

With the purpose of studying the nature of comets and their constituents, in the 1980's several space missions were developed and launched.

The first space mission devoted to the study of a comet was ISEE 3 (NASA), in 1985 (Von Roseninge et al., 1986). It flew by 21P/Giacobini-Zinner, at ~ 8000 km from the nucleus, and confirmed the Ions Tail model identifying the ions' composition and detecting a neutral current sheet at the centre of the tail. In 1986, comet 1P/Halley was observed by five international space probes: Missions Vega 1 and Vega 2 (Soviet Union), closest approach distance of 8890 km and 8030 km, respectively; Sakigake and Suisei (Japan), closest approach of $1.5 \cdot 10^5$ km and $7 \cdot 10^6$ km; GIOTTO (ESA), that reached the minimum distance of 600 km from the nucleus (Grewing et al., 1988).

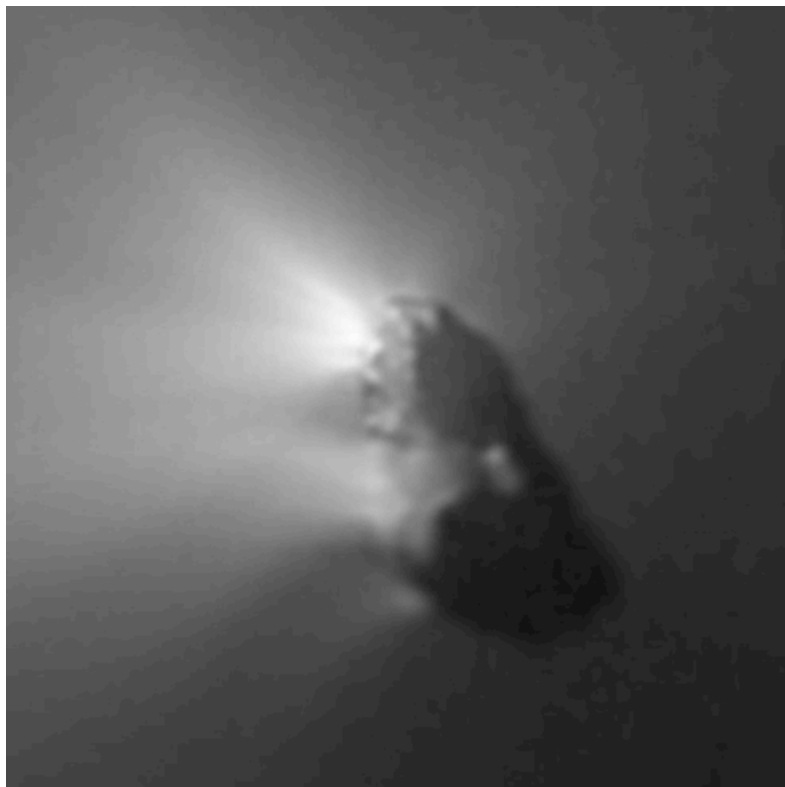


Figure 3: Composite *GIOTTO* image taken on 13th and 14th March, 1986 (© Max-Planck Institute for Aeronomy) (Weissman et al. 2004).

The observation of the comet nucleus at close range led to a surprising discovery: the nucleus, an irregular body of $(16 \times 8 \times 7)$ km³, appeared darker than expected with an albedo of about 4%. In

particular the GIOTTO mission photographed the surface structures of the nucleus and the source regions (Keller et al., 1988), pointing out that the active zones were only those exposed to sunlight. A further step forward in the understanding of the structures of the cometary nucleus was made in 1992, when comet Shoemaker-Levy 9 was fragmented (Figure 4) by tidal forces during the approach to Jupiter, and was destroyed during the subsequent impact on the planet (Weaver et al. 1995).

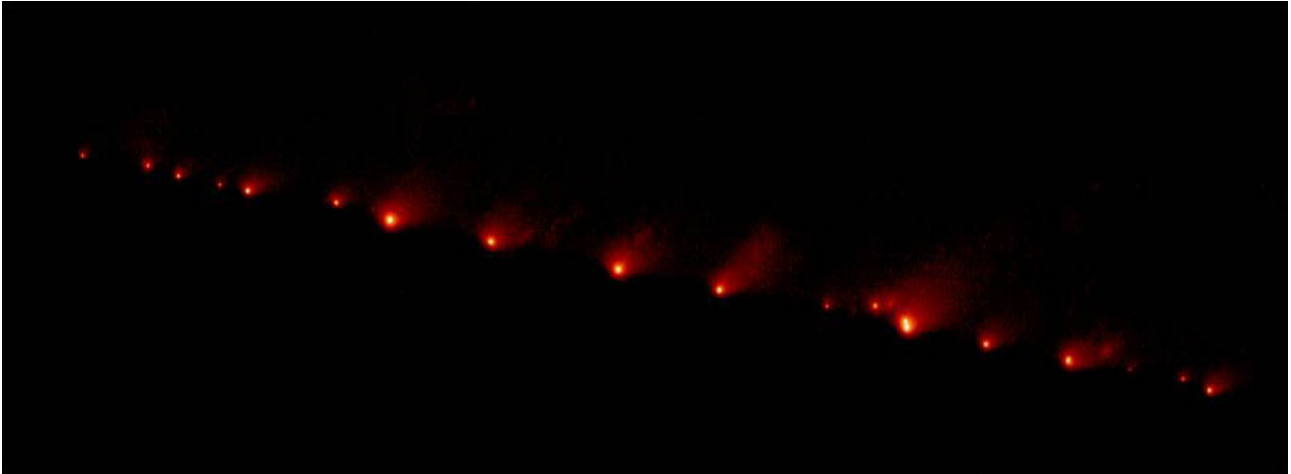


Figure 4: A NASA Hubble Space Telescope (HST) image of comet P/Shoemaker-Levy 9, taken on May 17, 1994, with the Wide Field Planetary Camera-2 (WFPC-2) in wide field mode. When the comet was observed, its train of 21 icy fragments stretched across 1.1 million km of space, or 3 times the distance between Earth and the Moon. This required 6 WFPC exposures spaced along the comet train to include all the nuclei. The image was taken in red light. The comet was approximately 660 million km from Earth when the picture was taken, on a mid-July collision course with the gas giant planet Jupiter. PHOTO RELEASE NO.: STScI-PR94-26c, FOR RELEASE: Thursday, July 7, 1994. Credit: H.A. Weaver, T. E. Smith (Space Telescope Science Institute), and NASA.

This event, in conjunction with other observational evidences, led to modify the Whipple model suggesting that weakly bound agglomerates of many dirty snowballs could form the structure of the nucleus. This modification of the theory of Whipple is called primordial rubble pile (Weissman 1998) and today is the most accredited in the scientific community. Indeed this is able to explain the behaviour of comet Shoemaker-Levy 9 and of many comets that occasionally disintegrate spontaneously. It can also justify the outburst observed in several comets, due to the breakdown of some nucleus agglomerates and the resulting exposure to solar radiation of new icy volatiles.

Since 2001 the Jupiter Family (J-F) comets have become the main target of several space missions, starting with the NASA missions Deep Space 1 that made its closest approach to comet 19P/Borrelly at 2171 km (Rayman 2003). In 2004 the Stardust mission (NASA) performed a closest approach, 250 km, on comet 81P/Wild 2 and for the first time brought back to Earth more than 10,000 grains from the comet, in the size range 1-300 μm (Brownlee et al 2006). The observation of 81P/Wild 2 nucleus showed that the comet has lost its original surface due to cometary activity.

Therefore the particles collected and returned to Earth were formed in the primordial nebular and not as consequence of recent solar processes. In 2005 another NASA mission, Deep Impact, flew over comet 9P/Tempel 1 with closest approach of 500 km, releasing a 370 kg copper projectile into comet in order to cause the ejection of cometary matter from the interior of the nucleus (Wissler et al 2005). Both Stardust and Deep Impact missions showed a considerable mineral diversity in the probed comets, much higher than expected. Laboratory analyses of 81P/Wild2 dust samples revealed in particular a wide variety of silicate minerals, allowing the size measure for each mineral grain and a high degree of compositional and structural inhomogeneity within the grains (Flynn et al., 2006; Zolensky et al., 2006; Keller et al., 2006, Brownlee et al., 2006; Rotundi et al., 2008; Rotundi et al., 2014). In particular, it was found that the majority of the particles collected contain Forsterite and Enstatite, in addition high-temperature minerals were found. These discoveries opened new questions on the Solar System formation process: some of the cometary building blocks did not necessarily form at distances from the Sun closer than Mercury orbit and not as always thought at the edge of the protosolar nebula. The presence of few grains mineralogically and isotopically linked to meteoritic calcium-aluminium-rich inclusions (CAIs) highlighted an analogy between the constituents of J-F comets and asteroid belt objects. Indeed the CAIs, the oldest samples of the Solar System that were formed in the hottest portion of the Solar Nebula, were found in carbonaceous chondrite meteorites, coming from the asteroid belt.

In 2010 another J-F comet, 103P/Hartley 2, was the target of the EPOXI NASA mission that performed a close fly-by at a distance of 700 km (Snodgrass et al., 2010). In 2011 NEXT, the Stardust extended mission, flew by Tempel 1 with a closest approach within 250 km.

All these space missions have improved our knowledge on the comets, but the characterization of cometary activity, nuclei and coma environments remain rather primitive in many aspects. We notice that the cometary environment characterization has been improved due to the gradual reduction of the closest approach distance (Table 2), however the knowledge of the coma dust and gas evolution is still limited by the short duration of the flown missions, i.e. all flybys.

| Comet Mission | Year | Comet | Closest Approach (Km) |
|-------------------------------------|------|-----------------------|-----------------------|
| ISEE 3 (NASA) ⁽¹⁾ | 1985 | 21 P/Giacobini-Zinner | 8×10^3 |
| Vega1 (Soviet Union) ⁽²⁾ | 1986 | Halley | 8890 |
| Vega2 (Soviet Union) ⁽²⁾ | 1986 | Halley | 8030 |
| Sakigake (Japan) ⁽²⁾ | 1986 | Halley | 7×10^6 |
| Suisei (Japan) ⁽²⁾ | 1986 | Halley | $1,5 \times 10^5$ |
| Giotto (ESA) ⁽²⁾ | 1986 | Halley | 600 |
| Deep Space 1 (NASA) ⁽³⁾ | 2001 | 19P/Borrelly | 2171 |
| Stardust (NASA) ⁽⁴⁾ | 2004 | 81P/Wild | 250 |
| Deep Impact (NASA) ⁽⁵⁾ | 2005 | 9P/Tempel 1 | 500 |
| EXOPY (NASA) ⁽⁶⁾ | 2010 | 103P/Hartley 2 | 700 |
| Stardust-NExT (NASA) ⁽⁷⁾ | 2011 | 9P/Tempel 1 | 200 |

Table 2: An overview of the different comet space missions. References: (1) Von Roseninge et al., 1986; (2) Grewing et al., 1988; (3) Rayman, 2003; (4) Brownlee et al., 2006; (5) Wissler et al., 2005; (6) Snodgrass et al., 2010; (7).

An incredible opportunity to increase the knowledge of J-F comets, thus on the origin of Solar System, is represented by the on going Rosetta space mission. Thanks to the encounter with the J-F comet 67P/Churyumov-Gerasimenko (67P/CG), this mission, for the first time, will undertake the long-term monitoring of a J-F comet at close quarters along its orbit, allowing the study of the comet behaviour from the beginning of the cometary activity until it reaches its maximum at perihelion.

2.2 The Rosetta spacecraft

Rosetta, originally conceived as a sample return mission, was later developed as a mission that could closely study a comet for a long time and able to analyse the comet's behaviour as it approaches perihelion.

It is composed by two elements: an Orbiter and a Lander, called PHILAE.

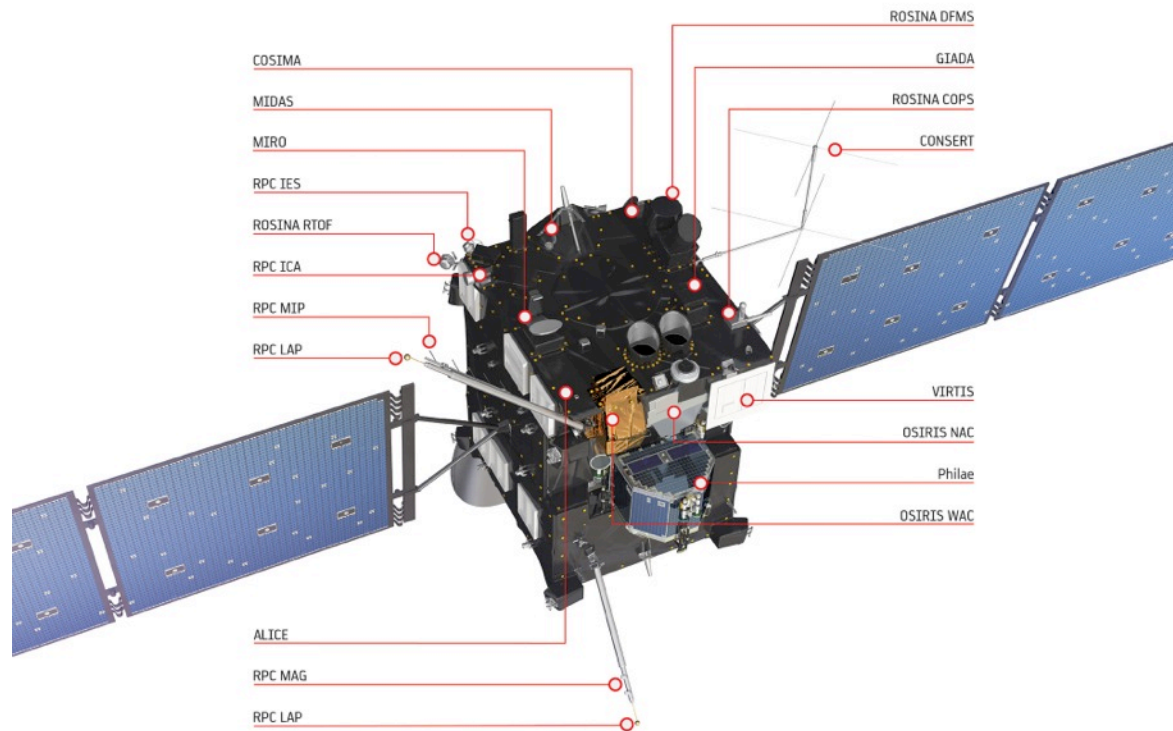


Figure 5: The placement of instruments and Lander on the Rosetta spacecraft (ESA courtesy)

The Orbiter design is based on a box-type central aluminium structure with dimensions of 2.8 x 2.1 x 2.0 m. on top of which are mounted the scientific instruments (Figure 5) whose main features are reported in Table 4. Among these payload there is the *Grain Impact Analyser and Dust Accumulator (GIADA)*, an instrument designed to study the coma in terms of dust flux and dust dynamics as a function of time and comet position along the orbit. In addition, GIADA was selected as monitoring instrument to check the dust environment as an hazard for the optics of the remote sensing instruments (e.g. dust coverages) and of the solar panels.

PHILAE is mounted on the spacecraft side parallel to the solar panels; on the opposite side the steerable high-gain antenna, composed by a 2.2m diameter communications dish, is mounted. The power supply is provided by two enormous solar panel “wings”. These wings, each formed by five panels of about 32 m², have a total span of about 32 m tip to tip. The solar arrays may be rotated through +/-180° to catch the maximum amount of sunlight.

The main propulsion system of the spacecraft is constituted by vertical thrust and two large propellant tanks; the upper one containing fuel and the lower one containing the oxidiser.

The spacecraft is a 3-axis stabilized structure, i.e. its attitude is constantly adjusted by rotating the satellite only around the three principal axes of inertia in order to avoid nutation effects. The orientation is controlled by 24 small thrusters, each one capable of a 10 N boost.

The spacecraft attitude, monitored by means of 2 star trackers, a solar sensor, a navigation camera and 3 laser gyroscopes, is controlled by means of 4 reaction wheels. In Table 3 are reported the key features of the spacecraft.

| Spacecraft vital statistics | |
|-----------------------------|-----------------------------------|
| Size | |
| Main structure | 2.8 x 2.1 x 2.0 m |
| Solar arrays Total Length | 32 m |
| Launch mass | |
| Total | ≈3,000 kg |
| Propellant | ≈1,670 kg |
| Science payload | 165 kg |
| Lander | 100 kg |
| Solar array output | 850 W at 3.4 AU, 395 W at 5.25 AU |
| Propulsion subsystem | 24 bipropellant 10N thrusters |
| Operational mission | 12 years |

Table 3: Vital statistics of the Rosetta Spacecraft (ESA courtesy)

The 11 scientific instruments installed on the Rosetta Orbiter and their scientific objectives are summarized in Table 4.

| Instrument Name | Scientific Objectives | Principal Investigator |
|--|--|---|
| <i>ALICE</i> | Ultraviolet Imaging Spectrometer (70nm-205nm) | Alan Stern, Southwest Research Institute, Boulder, Colorado, USA. |
| <i>CONCERT (Comet Nucleus Sounding Experiment by Radiowave Transmission)</i> | Radio sounding and nucleus tomography | Wlodek Kofman, Institut de Planétologie et d'Astrophysique de Grenoble, Grenoble, France. |
| <i>COSIMA (Cometary Secondary Ion Mass Analyser)</i> | Dust mass spectrometer (SIM, m/μm≈2,000) | Martin Hilchenbach, Max-Planck-Institut für Sonnensystemforschung, Katlenburg-Lindau, Germany |
| <i>GIADA (Grain Impact Analyser and Dust Accumulator)</i> | Dust flux measurement. Study of the dynamical properties of individual grains ejected by the comet. | Alessandra Rotundi, Università degli Studi di Napoli "Parthenope", Naples, Italy. |
| <i>MIDAS (Micro-Imaging Dust Analysis System)</i> | Grain morphology with an atomic force microscopy at nm resolution | Mark Bentley, Institut für Weltraumforschung, Graz, Austria. |
| <i>MIRO (Microwave Instrument for the Rosetta Orbiter)</i> | Microwave spectroscopy (1.3mm and 0.5mm) | Samuel Gulkis, Jet Propulsion Laboratory, Pasadena, California, USA. |
| <i>OSIRIS (Optical, Spectroscopic and Infrared Remote Imaging System)</i> | Multi-colour imaging with a narrow and a wide angle camera | Holger Sierks, Max-Planck-Institut für Sonnensystemforschung, Katlenburg-Lindau, Germany |

| | | |
|---|---|---|
| <i>ROSINA (Rosetta Orbiter Spectrometer for Ion and Neutral Analysis)</i> | Neutral Gas and ion mass spectroscopy DFMS:12-200AMU, M/ΔM≈3,000 RTOF12-350 AMU, M/ΔM>1,000 incl. Gas pressure sensor | Kathrin Altwegg, Universität Bern, Switzerland |
| <i>RPC (Rosetta Plasma Consortium).</i> | Ion composition analyser (ICA) Ion and Electron Sensor (IES) Langmuir Probe (LAP) Fluxgate magnetometer (MAG) Mutual Impedance Probe (MIP) Plasma Interface Unit (PIU) | Hans Nilsson, Institutet för rymdfysik, Kiruna, Sweden James Burch, Southwest Research Institute, San Antonio, Texas, USA Anders Eriksson, Institutet för rymdfysik, Uppsala, Sweden Karl-Heinz Glassmeier, Technische Universität, Braunschweig, Germany Jean-Pierre Lebreton, LPCE, Orléans, France Christopher Carr, Imperial College of Science, Technology and Medicine, London, United Kingdom |
| <i>RSI (Radio Science Investigation)</i> | Radio science experiment | Martin Pätzold, Universität zu Köln, Cologne, Germany. |
| <i>VIRTIS (Visible and Infrared Thermal Imaging Spectrometer)</i> | VIS and IR mapping spectroscopy (0.25-5 μm) | Fabrizio Capaccioni, Istituto di Astrofisica e Planetologia Spaziali, Rome, Italy. |

Table 4: Payload on board Rosetta Orbiter. In green is given the subject of this work: GIADA instrument

PHILAE, which will be released on 67P/CG nucleus, will allow in-situ measurements thanks to its 10 scientific instruments (Table 5). For a more detailed description of PHILAE see Bibring et al. (2007).

| Instrument Name | Scientific Objectives | Principal Investigator |
|--|---|--|
| <i>APXS (Alpha X-ray Spectrometer)</i> | A-p-X-Ray spectrometer | Göstar Klingelhöfer, Johannes Gutenberg-Universität, Mainz, Germany |
| <i>ÇIVA</i> | Panoramic camera an IR microscope | Jean-Pierre Bibring, IAS,Orsay, France. |
| <i>CONSERT (Comet Nucleus Sounding Experiment by Radiowave Transmission)</i> | Comet nucleus sounding | Wlodek Kofman, IPAG, Grenoble, France. |
| <i>COSAC (Cometary Sampling and Composition experiment)</i> | Evolved gas analyser: elemental and molecular composition | Fred Goesmann, Max-Planck-Institut für Sonnensystemforschung, Katlenburg-Lindau, Germany. |
| <i>MODULUS PTOLEMY</i> | Evolved gas analyser: isotopic composition | Ian Wright, Open University, Milton Keynes, UK. |
| <i>MUPUS</i> | Multi-Purpose Sensors for Surface and Subsurface Science | Tilman Spohn, Institut für Planetenforschung, Deutsches Zentrum für Luft- und Raumfahrt, Berlin, Germany |
| <i>ROLIS (Rosetta Lander Imaging System)</i> | Descent Camera | Stefano Mottola, DLR, Berlin, Germany |
| <i>ROMAP (Rosetta Lander</i> | RoLand magnetometer (ROMAG) | Hans-Ulrich Auster, TUB, Germany |

| | | |
|---|---|--|
| <i>Magnetometer and Plasma Monitor)</i> | Plasma monitor (SPM) | István Apáthy, KFKI , Budapest, Hungary. |
| <i>SD2 (Sample and Distribution Device</i> | Drill, sample, and distribution system | Amalia Ercoli-Finzi, Politecnico di Milano, Milan, Italy. |
| <i>SESAME (Surface Electrical Sounding and Acoustic Monitoring Experiments)</i> | Comet Acoustic Surface Sounding Experiment (CASSE) Dust Impact Monitor (DIM) Permittivity probe | Klaus Seidensticker, German Aerospace Center, Institute of Planetary Research, Asteroids and Comets, Berlin, Germany Harald Krueger MPI, Göttingen, Germany Walter Schmidt, FMI, Helsinki, Finland |

Table 5: Instruments on board PHILAE lander.

2.3 The Target

Originally the target selected for the Rosetta mission was comet 46P/Wirtanen. A problem occurred in December 2002 on an Ariane 5 rocket forced ESA to postpone the launch date, initially scheduled for January 2003. The launch postponement made necessary to change the “target” of the mission. The new selected target was comet 67P/CG a short period comet belonging to the Jupiter Family (J-F) comets (Lamy et al 2007). It was discovered on the 11th of September 1969, by Klim Ivanovic Churyumov and Svetlana Ivanova Gerasimenko who were actually studying comet 35P/Comas-Solas on photographic plates produced with the 50cm f2/4 Maksutov telescope of the Alma Ata Observatory (Kazakistan). J-F comets were formed by fragments generated by collisions of the larger Kuiper Belt Objects (Farinella and Davis, 1996; Duncan et al 2004). As explained above, J-F comets are thrust toward the inner Solar System by means of repeated gravitational perturbations performed by the giant planets and are then captured by Jupiter on nearly elliptical short-period orbits around the Sun (Morbidelli and Brown, 2004; Duncan et al., 2004).

Jupiter currently controls the evolution of the 67P/CG orbit. Calculation based on the evolutionary models has revealed that, over the past 200 years, the comet had many “encounters” with the giant planet. The encounter occurred on 4th February 1959, 10 years before the comet discovery, was the closest to the planet at a distance of 0.0518 UA (Belyaev et al., 1986). This close encounter has significantly modified the comet’s orbit dropping the distance at perihelion from 2.74 AU to 1.28 UA, modifying the eccentricity from 0.36 to 0.63 and also reducing its orbital period from 8.97 to 6.55 years (Lamy et al. 2007). Therefore this close encounter makes the 67P/CG available for Rosetta mission.

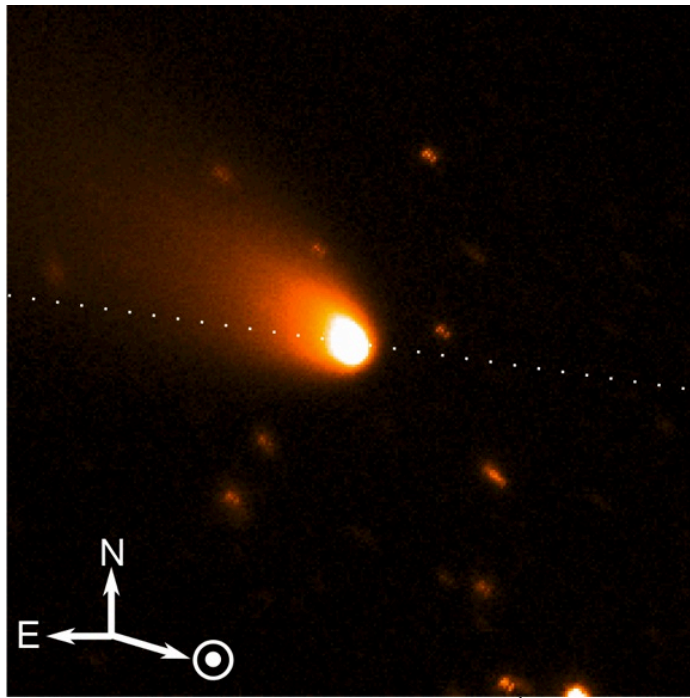


Figure 6: An image of the dust coma of 67P/CG acquired on 22th October 2008, during its last appearance at heliocentric distance of 1.90 AU. The image was taken with the 8.2 m Unit Telescope of Very Large Telescope (VLT) at the European Southern Observatory, Chile. Orientation: north is up and east is left. Field of view: 195×195 arcsec = 273 000 km at the comet (Vincent et al 2013).

The J-F comet 67P/CG has been largely studied (e.g. Lamy et al., 2009, Kelley et al.; 2009, and references therein). Table 6 summarizes the main physical characteristics of 67P/CG. By means astronomical observations, several dynamical models of the dust coma and tail of 67P/CG have been developed recently (Ishiguro, 2008; Kelley et al., 2009). In Fulle et al. (2010) is developed a more coherent model, able to fit all available coma, tail, neckline and trail data using a selection of observations representative of all ground-based and IR (thermal infrared) Spitzer data, collected during the last three perihelion passages.

| Comet 67P/Churyumov-Gerasimenko | |
|--|------------------------|
| Nucleus radius | (2.38 ± 0.04) km |
| Large-to-small axis ratio | $> 1.45 \pm 0.09$ |
| Rotational period | (12.705 ± 0.001) h |
| Orbital Period | 6.55 yr |
| Albedo | 0.045 – 0.060 |
| Aphelion distance | 5.71 A.U. |
| Perihelion distance | 1.25 A.U. |

Table 6: Physical characteristics of the comet 67P Churyumov-Gerasimenko derived from astronomical observations.

3. GIADA - Grain Impact Analyser and Dust Accumulator – on board Rosetta

3.1 GIADA contribution to the scientific goal of the Rosetta space mission

Cometary activity is the reason of forming a relatively dense coma of dust and gas and long dust and plasma tails extended of the tens of millions of km away from the nucleus. Main aims of past and current comet space missions are: 1) Determining the source of active regions on the nucleus; 2) Studying the link between the circumnuclear coma (i.e. the unbound, free-expanding gas + dust envelope embedding the nucleus up to distances of about 50 km) and the physico-chemical properties of the nucleus surface (i.e. the coma source); 3) Monitoring cometary activity events, such as dust jets, that can give clues on the rotational state of the nucleus and the size distribution of the particles. The evolution of the coma driven by gas and dust motion can only be well understood by studying the dynamical properties of the particles: their velocity, density and size distribution. In-situ analyses in the coma of comet Halley have shown dust size distribution from sub μm to cm in size range. Beside the data obtained by former space missions to comets as GIOTTO (Halley), VEGA (Halley), STARDUST (Wild2), EPOXI (Hartley 2) etc., there is still room for investigating physical properties of cometary dust. There are no direct measurements of in-situ dust velocities in the close vicinity of the nucleus so far, so that any current estimation of the cometary mass losses remains hardly reliable. GIADA onboard the Rosetta spacecraft is on its way to fill the gap of missing knowledge on the dynamical properties of cometary dust. Thanks to its characteristics, described in the following paragraphs, GIADA will contribute to the achievement of two of the five Prime Goals assigned to the Rosetta space mission:

- Define the physical properties and interrelation of volatiles and refractories in a cometary nucleus;
- Study the development of cometary activity and the processes in the surface layer of the nucleus and in the inner coma (dust-gas interaction).

GIADA was developed to study: 1) the cometary dust environment; 2) the evolution of the dust flow and the dynamics of single grains in the coma as a function of time and position. In addition, GIADA was selected as “monitoring instrument” to screen the cometary dust environment to communicate alarming condition that could affect the performance of other instruments (e.g. optics dust coverage). The specific physical quantities that GIADA will measure directly, those that will

be derived from the measurements and those that will be derived with the combination of GIADA results plus information coming from other Rosetta Payloads are reported in Table 7

| Physical Quality | Direct Measurement | Derived Measurement | Derived with Auxiliary data from other instruments | Range |
|---------------------------|--------------------|---------------------|--|--|
| Speed | x | | | 1-100 [m/s] |
| Momentum | x | | | $6.5 \cdot 10^{-10}$ - $4 \cdot 10^{-4}$ [Kg·m/s] |
| Fluence of dust Particles | x | | | $1.9 \cdot 10^{-9}$ - $2.9 \cdot 10^{-4}$ [g/cm ²] |
| Optical Cross Section | x | | | Function of optical properties of DUST particles |
| Mass | | x | | $2.2 \cdot 10^{-12}$ - $4 \cdot 10^{-4}$ [Kg] |
| Flux | | x | | $6 \cdot 10^{-12}$ [g·cm ⁻² ·s ⁻¹] |
| Size | | | x | Derived from Optical Cross-Section and Dust Grains Composition |

Table 7: Physical quantities measured by GIADA; derived from GIADA measurements; derived from the combination of GIADA results plus information coming from other Rosetta Payloads

3.2 GIADA: instrument description

GIADA is designed as a single instrument using three different detection sub systems:

1. Grain Detection System (GDS): a device detecting each incoming grain without affecting its dynamical properties. The GDS detects the grain and providing its optical equivalent size and measuring the grain speed.
2. Impact Sensor (IS): measures the momentum released from each grain that impacts its sensitive surface.
3. Micro-Balances System (MBS): a network of five Quartz Crystal Microbalances, pointing toward different directions, that measure the cumulative dust deposition in time, allowing the monitoring of the dust flux ejected by the comet.

When a grain is detected sequentially by GDS and IS (“GDS+IS event”), the time of flight between the two sub-systems is measured and thus the grain speed is calculated. The grain speed combined with the measure of the grain momentum by IS, allows to derive the grain mass.

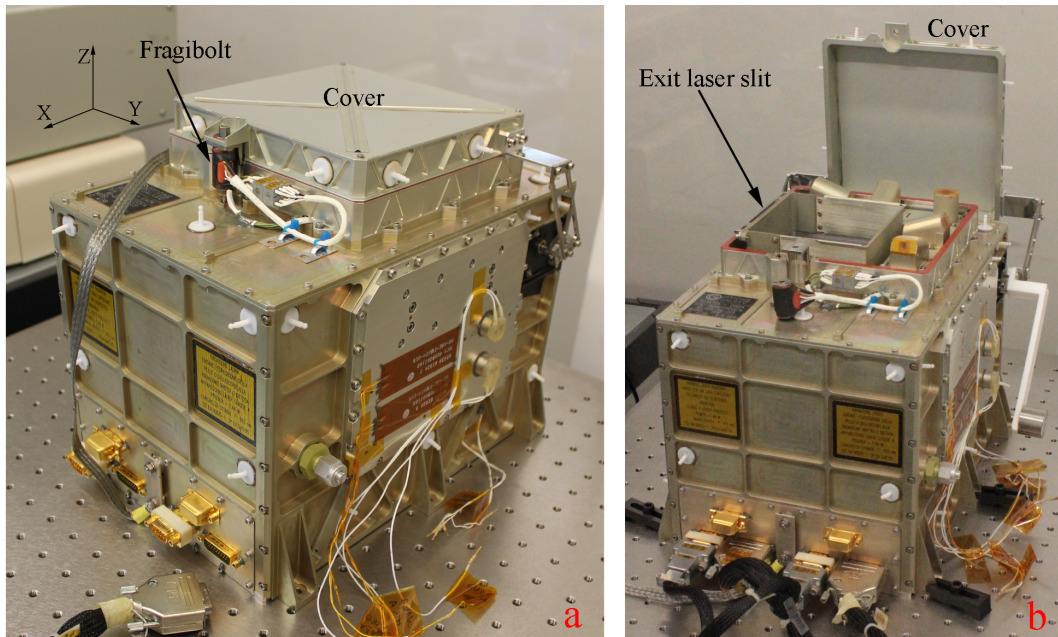


Figure 7: GIADA: (a) closed cover configuration with the instrument reference frame; (b) open cover configuration (Della Corte et al., 2014)

These three sub-systems are protected by a multi shot cover mechanism (Figure 7) that prevents contamination during the non operating phases. The cover was kept locked during the Rosetta launch by means of a Frangibolt. This has been activated during the first inflight commissioning, unlocking the cover.

3.2.1 Grain Detection System

The Grain Detection System is a sub-system able to detect optically the crossing of each single grain entering GIADA without affecting its dynamical properties. This is a crucial feature for the coupled use of the GDS with the Impact Sensor, as we will see later.

The working principle of the GDS is based on optical detection of grains entering the baffle of GIADA and crossing a laser curtain generated on the XY plane by an illumination-collimation system (Figure 8). The light scattered or reflected by the grain is collected by two series of receivers placed at 90° with respect the light propagation direction in the plane of illuminated area. The recorded signal and the measure of the crossing time of the laser curtain allow estimating the size and the speed of the particle.

The illumination system is obtained by 4 Laser diodes mod. SDL-4001 equipped with optical fibre. The electromagnetic wave emitted by the four lasers is picked at $\lambda_0 = 915\text{nm}$. In the “nominal” operative conditions the power emitted is $P = 0.5\text{W}$, depending on the temperature and the operating current.

The four lasers are pulsed with a frequency of 100kHz and are matched two by two; when the lasers #1 and #3 are switched on, the #2 and #4 are switched off, and vice versa. The choice of this

sequence was made to reduce the electromagnetic noise due to on/off sequence of the lasers (Colangeli et al., 2009).

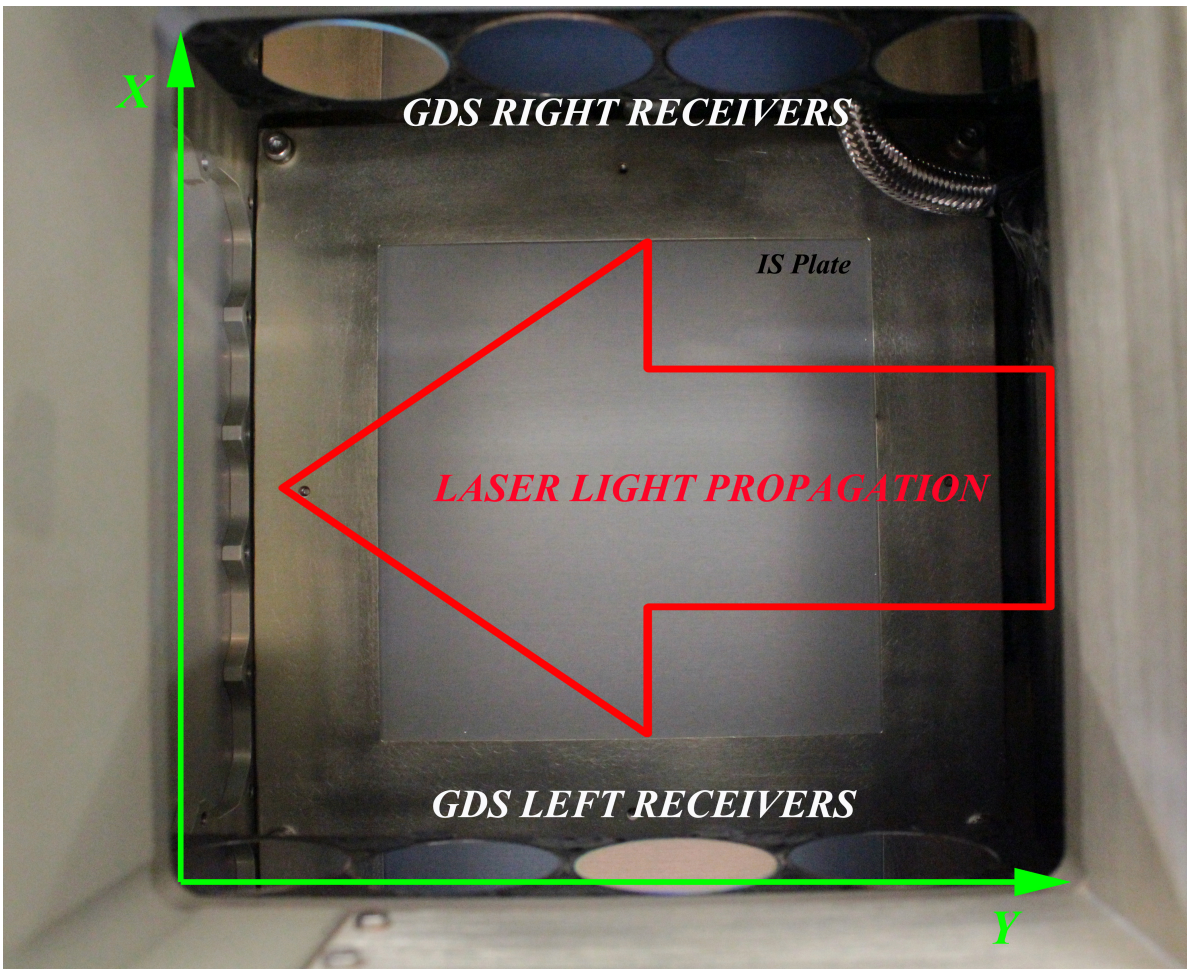


Figure 8: Laser propagation direction and positioning of the photodiodes receivers composing the GDS subsystem

The illumination system is coupled with a collimation optic, both are placed vertically inside GIADA, as shown in Figure 9. The collimation system is composed of two convergent cylindrical lenses (curvature radius of 10mm), one divergent cylindrical lens (curvature radius of 33.5mm) and a total internal reflection prism (curvature radius of 26.5mm), placed at 10.3 mm from the divergent lens (Figure 10). This prism allows to collimate and simultaneously tilt the laser beam at 90° with respect to the Z-axis (Figure 9), to form the laser curtain in the plane XY. The laser light propagation results in the Y - direction. Each laser creates a collimated beam with a rectangular shape 23 mm wide, along X-axis, and 3 mm thick along Z-axis. A system of mirrors, mounted at the end of the GDS illuminated area, deflects the laser beam through a slit outside GIADA toward the deep space. This allows to eliminate reflections of the laser beam inside GIADA and to minimize any possible stray light. When the cover of GIADA is closed, also the exit slit of the laser is closed (Figure 7).

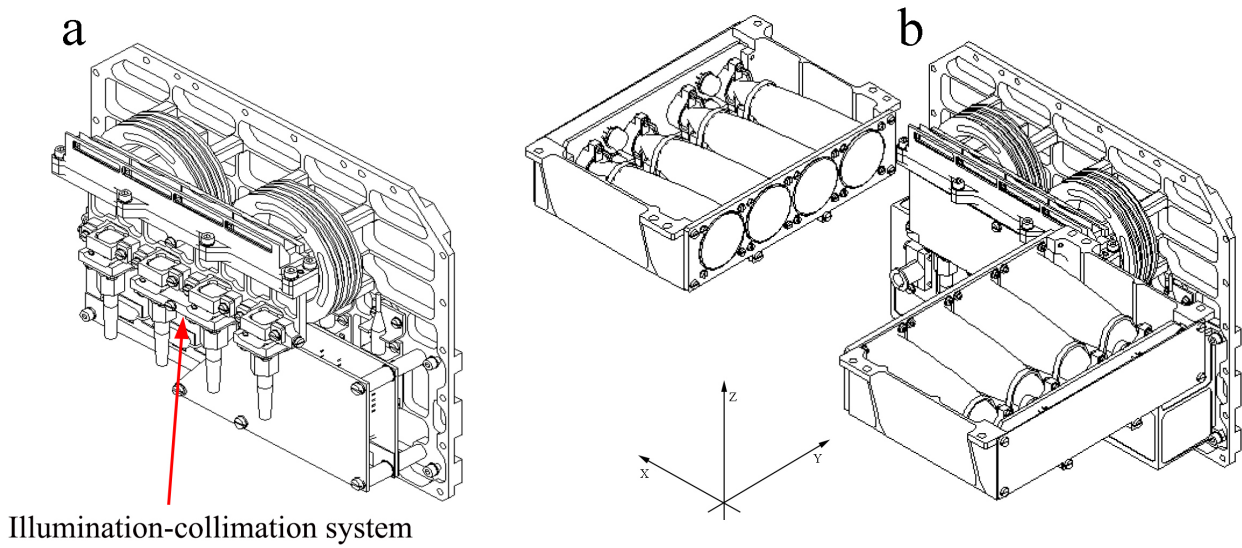


Figure 9: Mechanical schemes of (a) the plate on which the illumination-collimation system is vertically installed, (b) the configuration of in flight GDS. The reference system used to describe the sub-system is reported in the sketch.

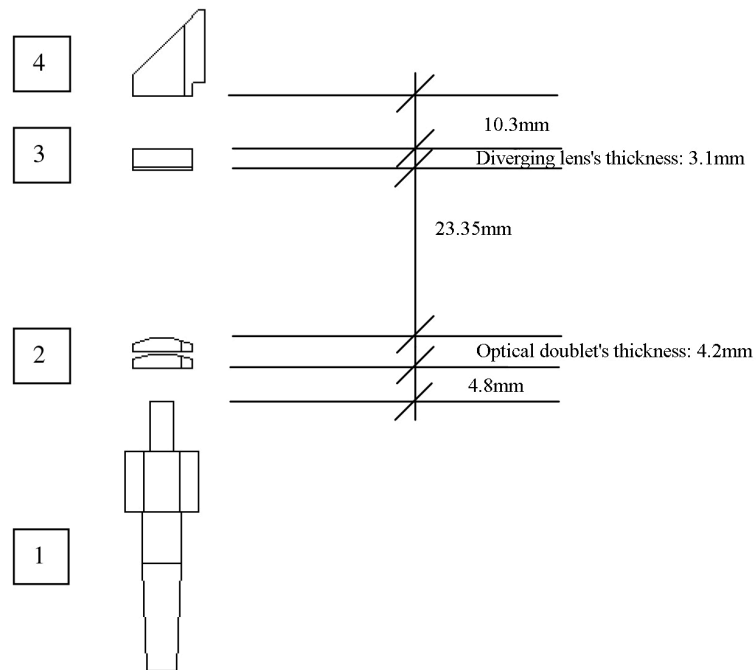


Figure 10: The collimator optical system for each laser beam: (1) the SMA connector for the optical fiber, (2) the optical cylinder lens, composed by two identical cylindrical lens with curvature's radius $r_1=10\text{mm}$ and thickness at centre of 2mm , placed at a distance of 0.2mm ; (3) the negative cylindrical lens, with curvature's radius $r_2=33.5\text{mm}$ and thickness at centre of 2mm ; (4) the total internal reflection collimator prism, with curvature's radius $r_3=26.5\text{mm}$.

The detection area results to be of $100 \times 100 \text{ mm}^2$, and identify the XY plane, the light scattered by the dust particles is collected by two separate detection units placed on opposite sides, at 90° with respect to the light propagation direction.

The choice of the detector placement has been the subject of a detailed study during the development phase of the subsystem (Mazzotta–Epifani, 2000), following the Mie scattering theory. This theory provides a mathematical rigorous solution of the Rayleigh theory for the scattering and absorption of electromagnetic radiation by spherical particles with dimensions comparable or larger than the incident wavelength (Bohren and Huffman, 1983). Particularly, considering spherical particles, the distribution of scattered intensity, as reported in Barber and Hill (1990), shows a minimum around 90° with respect the direction of light propagation (Figure 11). As displayed in Figure 11, the light is scattered mainly forward; therefore, the placement of the receivers at 90° , with respect to the direction of propagation of the laser, gives the disadvantage of collecting the scattered light with the lowest intensity. Nevertheless, this solution allows to eliminate problems arising with the placement of the detectors at angles smaller than 90° , in which case we would get a relevant background light signal coming directly from the source. This background signal would produce the degradation of the sub-system performances. Comparing the analysis of the advantages with respect to the issues related to the positioning of the detectors, the configuration with the detectors at 90° with respect to the direction of light was selected.

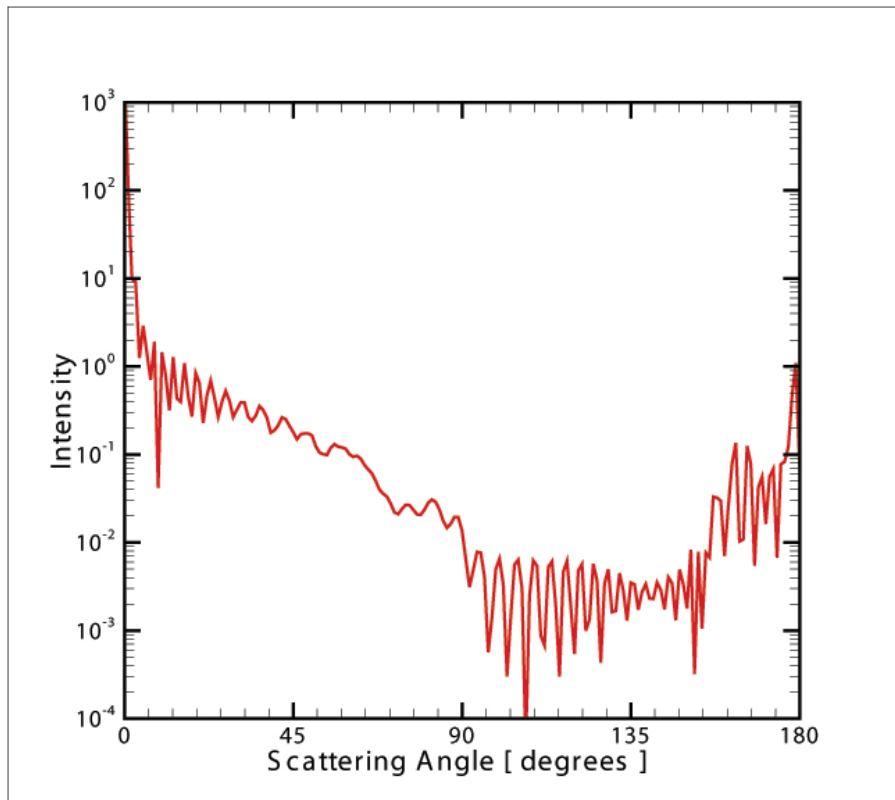


Figure 11: Angular scattered intensity for a spherical particle of bytownite (refractive index: $n_{\text{real}}=1.5$ $n_{\text{im}}=0.13 \cdot 10^{-4}$) with diameter of $50 \mu\text{m}$, calculated for an incident radiation ($\lambda=0.9$) polarized parallel, and obtained using the code published in the “Light Scattering by Particles: Computational Methods” (Barber and Hill, 1990)

Once defined the receivers placement, the detection system was optimized to obtain a uniform response over the whole sensitive surface, and to collect the maximum of the scattered radiation from the grains that pass through the laser curtain. These requirements were achieved using eight Winston cones in the detection system, four at each opposite side. These Compound Parabolic Concentrators (CPCs) (Winston, 1970; Welford and Winston, 1989) are non-conventional optical systems used to concentrate a large amount of radiation on a little detection surface. Their main feature is the high self-baffling property; the angular transmission of the radiation is constant within the maximum acceptance angle, ϑ_{max} , determined by the geometrical characteristics of the cone:

$$\sin \vartheta_{max} = \frac{a}{A} \quad (3.1)$$

$$L = \left(\frac{a + A}{2} \right) \cdot \cot \vartheta_{max} \quad (3.2)$$

$$l = \frac{\frac{A}{2}}{\tan \vartheta_{max}} \quad (3.3)$$

Where a is diameter of the exit pupil, A is the diameter of the entrance pupil, L is the length of the cone and l is the length of active area (see Figure 12).

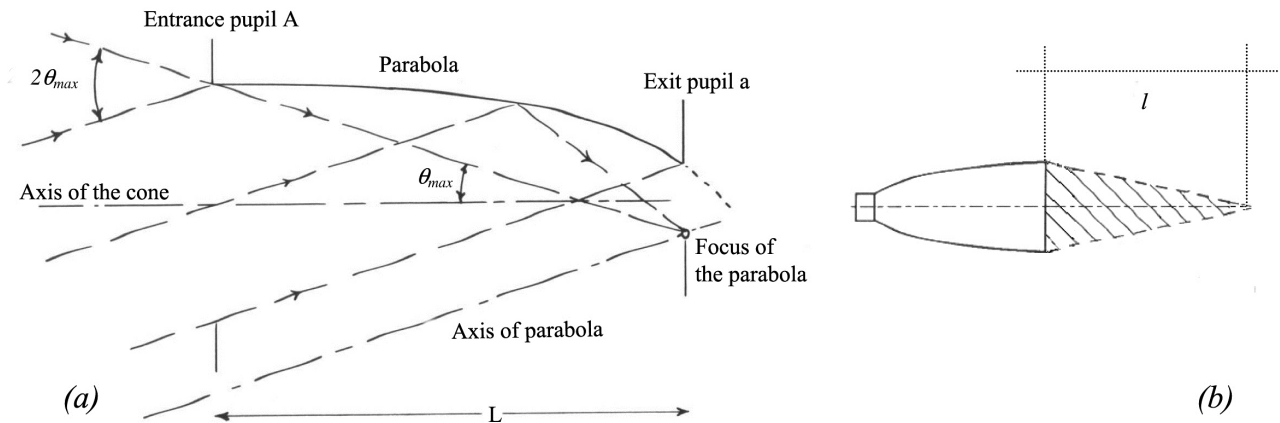


Figure 12: (a) 2D profile of a Winston cone, its geometric characteristics are reported: the diameter of the entrance pupil (A) and of the exit pupil (a), the length (L) and the maximum angle of acceptance (ϑ_{max}); (b) the projection (dashed area) on the plane of the sheet of the constant efficiency of the cone with half-opening of the triangle equal to ϑ_{max} and area length equal to l (Welford and Winston, 1989).

The rays of light entering the cone with angles greater than ϑ_{max} are re-emitted through the entrance pupil, after repeated reflections. This determines an area of constant detection efficiency, which in 2D is a triangle with the vertex on the axis of the concentrator and length l , obtained by equation (3.3).

In order to save space and mass without degrading the optical properties, described above, for GIADA truncated cones, characterised by a maximum angle of acceptance $\vartheta_{max} = 7.07^\circ$, are used. Each cones is equipped with an interference filter, designed to optimise the transmission in the operative band, peaked at $\lambda_0 = 915nm$ with $\Delta\lambda = 70nm$ at 0.9 Bandwidth (Mazzotta Epifani et al. 2002). The detector used in each cone is a PIN photodiode mod. AME AE-945, optimally coupled to the cone exit pupil. To improve the efficiency of the cone-photodiode system, the photodiodes active area is greater than the cone exit pupil.

The GDS Proximity Electronic

The signal detected by the GDS is read from Proximity Electronic (PE); the working principle of PE is the differential reading between two adjacent photodiodes. As shown in Figure 13 the current read by each photodiode is converted into voltage by a resistor $49.9 k\Omega$ before arriving at the amplifier input; for each *Ampere* generated by the photodiode we have a voltage of $49.9 kV$.

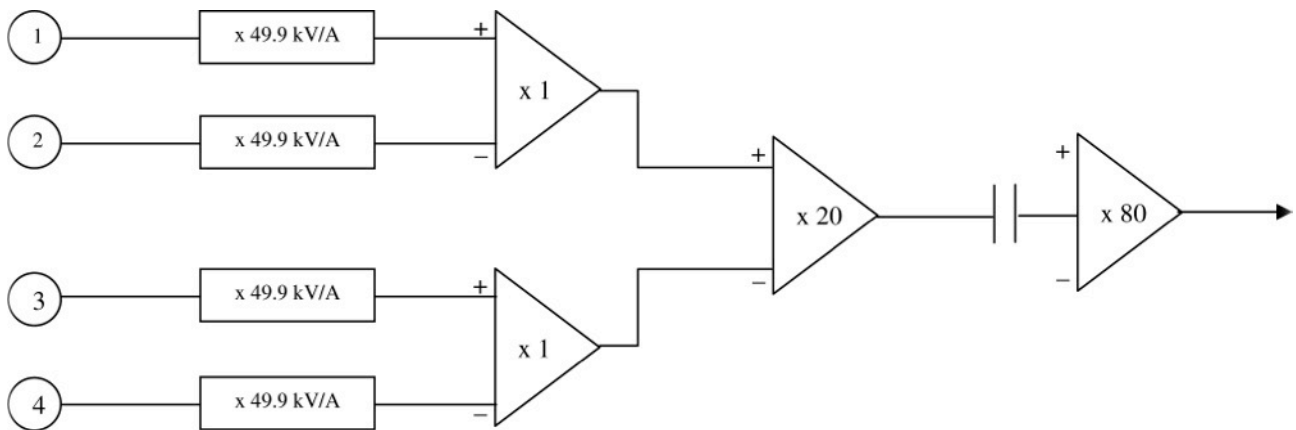


Figure 13: Diagram of the GDS Proximity Electronic. It is schematically shown the reading circuit of one of the two sides of the detector systems (Mazzotta Epifani, 2000).

The differential reading is operated in pairs: the signal of a photodiode is subtracted from that of the adjacent photodiode, then the two resulting voltages are subtracted in their turn at the second amplification stage, where the signal is amplified 20 times. Between the second and the third stage, the AC coupling is present; which has the aim of eliminating the DC component of the signal, keeping only the component pulsed to $100 kHz$, generated by the scattering of a particle that passes through the laser curtain. With this configuration the Proximity Electronics is able to separate the light scattered by the dust particle crossing the laser pulsed curtain from the light coming from external continuous sources.

The signal passes to the third stage, where it is amplified 80 times for a total value of $8 \times 10^7 V/A$, and enters the Main Electronics (ME); there the signal is compared with a threshold value. That can

be defined by means of the control software of the instrument from $0 V$ to $10 V$, with $40 mV$ resolution. The Main Electronic records the signal as an “event” corresponding to the crossing of a particle, only if this exceeds the threshold value a number of times n . The values of n can be changed by software from 1 to 3 .

The number of pulses recordable ranges from 1 to 1023 ; this means that the system is able to record the crossing times of the laser curtain between $10 \mu s$ to $10 ms$.

The ME can measures signals in the range $0mV$ e $6.9375V$ with a resolution of $3.4 mV$. Actually the lower limit is determined by the RMS noise of the PE, that was estimated in $40mV$.

The possibility of being able to set the number of revelations n in order to define an *event*, involves variations on the maximum speed detectable by the GDS. Indeed, considering the thickness of the curtain laser ($3 mm$) and $n = 3$, we obtain $v_{max} = 100ms^{-1}$. If we accept $n=2$, the maximum speed detectable by GDS became $v_{max} = 150ms^{-1}$.

On the other hand, we would point out that the decrease of n , raises the uncertainty on the detection of real event: i.e. electronic spikes could be registered as dust particles.

The working principle

A cometary grain entering into GIADA crosses the GDS laser curtain scattering radiation. The radiation is collected by the detection units and, as described above, is elaborated by the Proximity Electronics and Main Electronics. The voltage signal S , recorded by the detector, is correlated to the optical grain cross section by the equations:

$$S = F_A \cdot F_C \cdot E_{det} \cdot E_{filt} \cdot L \cdot \sigma \quad (3.4)$$

Where:

F_A is the amplification factor of the Proximity Electronics: $F_A = 8.2 \times 10^7 V/A$

F_C is the amplification factor of the photodiode: $F_C = 0.55 A/W$

E_{det} is the efficiency of the detection system [CPC+photodiode]: $E_{det} = 0.7$

E_{filt} is the transmission factor of the interference filter $E_{filt} = 0.9$ in its band

σ is the equivalent cross section of the grain at λ_0

L is the irradiance in the laser curtain

The irradiance L in the laser curtain depends on: 1) the temperature of the lasers; 2) the current of the power supply; 3) the efficiency of concentration and attenuation of the optics. The optical power

emitted by the laser is strictly dependent on the operating conditions. The mean irradiance in the laser curtain was measured during the calibration performed in 2002, the value obtained is $L=0.47W/cm^2$ in nominal conditions (Mazzotta Epifani et al., 2002).

The equivalent laser cross section of the particle can be determined by measuring the signal S detected by the GDS. From the particle cross section information on its dimension can be derived by means of calibration curves and information from other Rosetta payload. Taking into account the thickness of the curtain ($3mm$), the crossing time of the curtain laser gives us information about the speed of the particle. This is a redundant information that can be compared to the particle speed measured by GDS+IS (see section 2.2).

3.2.2 Impact Sensor

Under the GDS is positioned the Impact Sensor (IS), an impact detection system able to measure the momentum released by a single grain impacting on it. The IS is composed of a 100 cm^2 square aluminium plate mounted parallel to the GDS sensitive area at a distance of 100 mm . This plate is connected, at the four corners and in its center, to five lead zirconate titanate ceramic piezoelectrics transducers (PZT). An impacting grain creates a bending wave that propagates along the plate at a frequency of 200 kHz ; this is detected by the PZT sensors and converted in an electrical signal. In order to avoid the measurements of the reflected wave along the plate, the signal amplitude measure is performed within $39\text{ }\mu\text{s}$ after the wave reaches the PZTs. In this time interval there is no overlap between the main wave and the waves that are reflected on the IS edges (Esposito, 2001). The amplitudes of the signals are directly related to the momentum released by the impacting grain. The IS was designed to measure the momentum of cometary grains in the range $3 \times 10^{-11}\text{ Ns} - 3 \times 10^{-5}\text{ Ns}$.

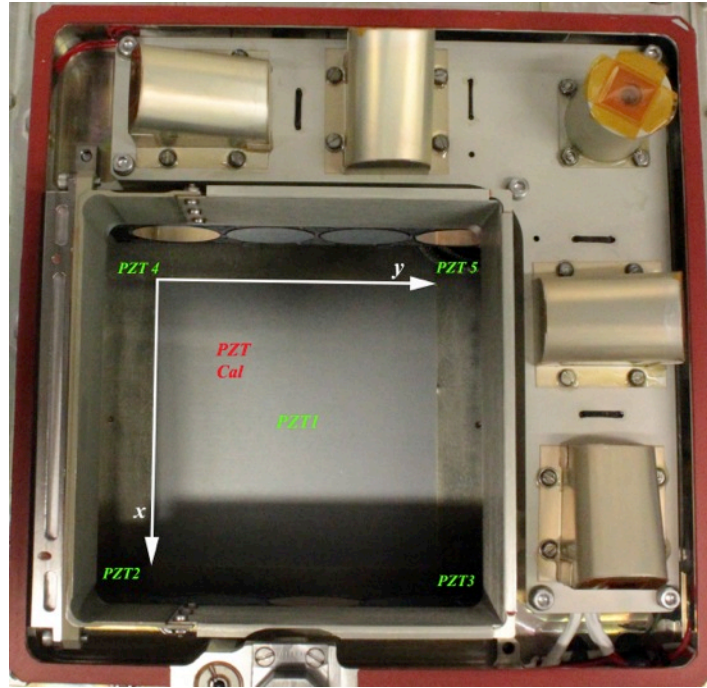


Figure 14: The IS sub-system mounted inside GIADA is shown together with the reference system and the positions of the PZTs.

The IS sensitive surface is a square aluminium plate of $124\text{ mm} \times 124\text{ mm}$ with a thickness of 0.5 mm . The edges of the plate are glued, with the exception of 5 mm for each edge, on a support equipped with anti-vibration pads isolating the plate acoustically from the spacecraft. A protection frame reduces the sensitive surface to a square area of $100 \times 100\text{ mm}^2$.

Five piezoelectric sensors PZT5A, discs with a diameter of 5 mm of diameter produced by Morgan Matroc and resonant at frequency of 200 kHz , are placed under the four corners and at the centre of the Al plate, as shown in Figure 14. The PZT are numbered from 1 to 5. An additional PZT, placed under the Al plate between PZT1 and PZT5, acts as an internal calibrator (PZT Calibrator).

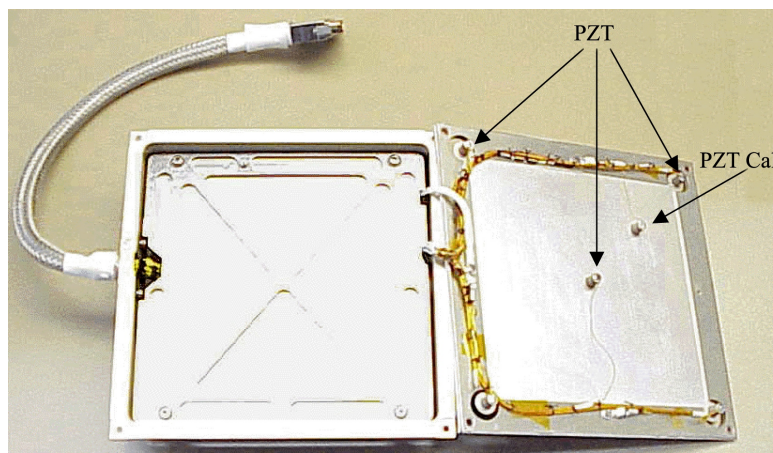


Figure 15: The IS in open configuration showing the position of the five Piezoelectric sensors plus the Piezoelectric Calibrator.

The IS Proximity Electronic

The IS Proximity Electronic provides an amplification channel for each PZT. Two PZTs (*PZT2* and *PZT3*) channels are set to a fixed gain, High (H), in order to increase the measurement precision of the grain arrival time. The *PZT4* and *PZT5* channels can be set on two different gains: High (H) or Low (L). The switch from one to the other is controlled by a dedicated command. The central sensor, *PZT1*, has a double channel: it is connected both to a chain of L gain and one of H gain. In this case the Main Electronic read the signal of the H channel and when saturated it is automatically switched on the channel L. In addition it was included an attenuation network, the *Range*, which halves the gain of the switchable channels when they are set on H, vice versa, it does not act when they are set on L.

In the channels with fixed gain (*PZT2* and *PZT3*) the signal coming from the sensor passes through a three-stage active pass band filter with gain A_v , centred at the resonance frequency of the transducer, 200 kHz (see Figure 16). At the filter output, a peak detector records the maximum value of the acquired signal in response to a digital command of *Hold*. This command disconnects the filter output from the input of the peak detector, and subsequently starts a cycle of conversion A/D. A digital *Reset* command set to zero the channel value. . After the *Reset* command, the peak detector is ready for a new acquisition.

For the channels with variable gains, (*PZT4* and *PZT5*) the signal coming from the PZT is attenuated, through a balanced divider, by factor of 1 or A_v , depending on the *Gain* settings (Figure 17).

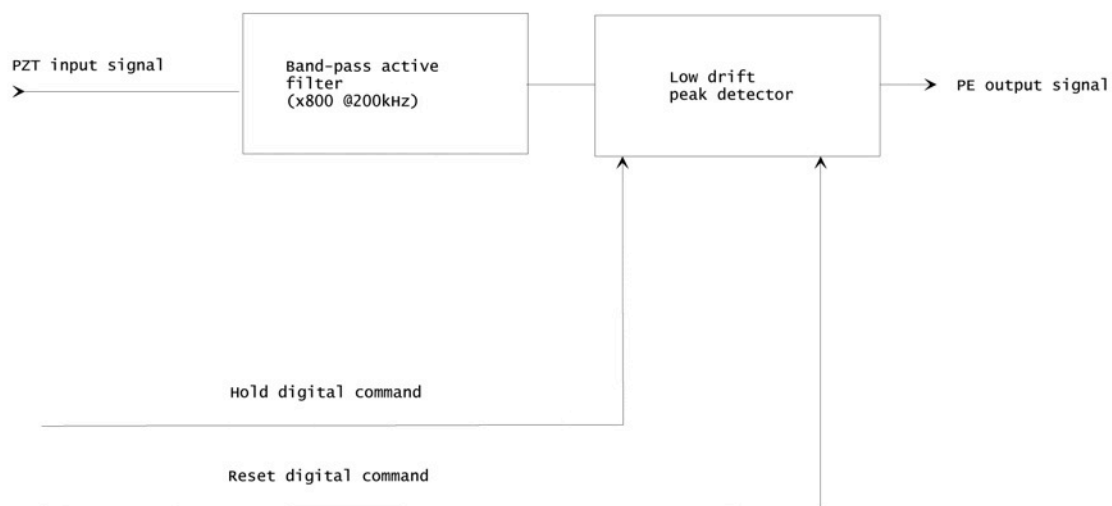


Figure 16: Operation scheme for the channels with a fixed gain.

At the output of the first attenuator network there is a further balanced divider, that by mean of the digital control signal *Range*, passes either the entire signal or the halve of it. The remaining part of the circuit is identical to that of the channels with fixed gain. This configuration allows us to pre-set the overall gain of the chain to the values 1, A_v or $A_v/2$.

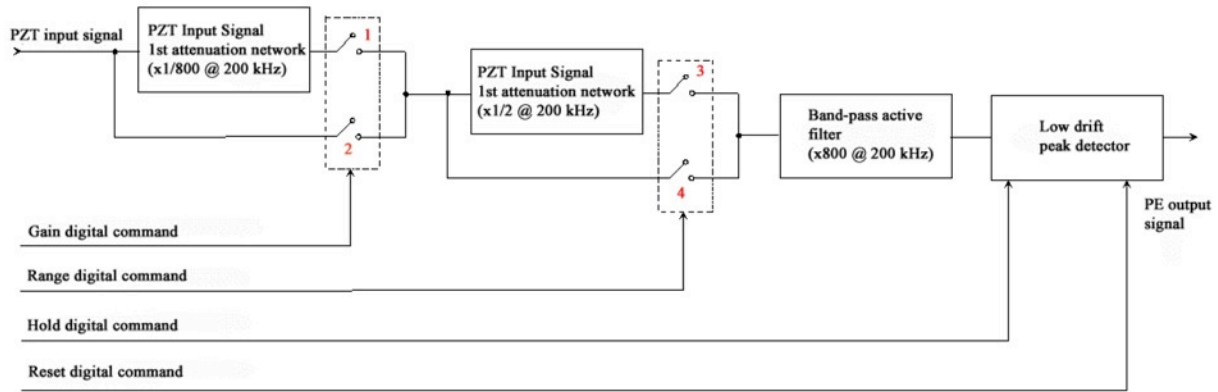


Figure 17: Operation scheme for channels with variable gain.

The scheme of the *PZTA* (Figure 18) differs from that of the variable gain channels: in this case there are two different chains of filtering and amplification, one with an A_v gain and the other with a gain of 1, each with a dedicated peak detector. The *Gain* signal controls which one of the two outputs has to be acquired. The signal *Range* is used in this case as for the channels with variable gain.

For channels L the gain is set to 1, while for the H-channels the gain is set to $A_v = 800$.

For the variable channels, thanks to the use of the signal *Range*, are possible three different gain values: $x1$, $x400$, $x800$.

The Officine Galileo (now called SELEX SES), manufacturer of the subsystems, estimated a noise of about 30 mV produced by a channel with a gain of $x800$, while the saturation level for all channels is about 11.5 V (Esposito, 2001).

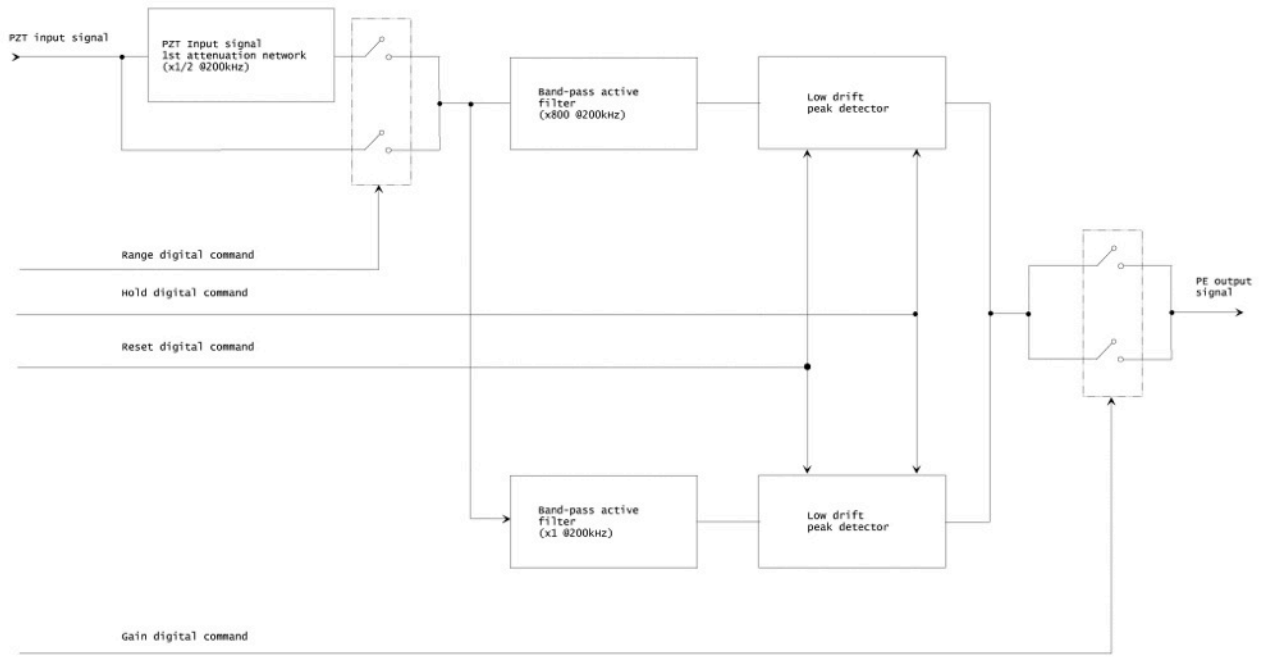


Figure 18: Operation scheme for channel with “double gain”.

The working principle

Clapp (1963) and McDonnell (1969) have shown that, after a grain impact on a thin lamina, multiple modes of wave propagation occur, but the dominant component is the transverse bending wave; the velocity of this flexural wave depends on the frequency. For a free lamina we can estimate the theoretical group velocity (Landau and Lifšits, 1995):

$$U = f^{1/2} h^{1/2} \sqrt[4]{\frac{16\pi^2 E}{3\rho(1 - \sigma^2)}} \quad (3.5)$$

where :

f = the wave frequency

h = lamina thickness

E = Young's modulus

ρ = lamina density

σ = Poisson's ratio

For the Impact Sensor used on GIADA we have $E=6.7 \times 10^{10} \text{ Nm}^{-2}$, $\rho \approx 2750 \text{ kgm}^{-3}$, $\sigma \approx 0.33$, $h \approx 0.5 \times 10^{-3} \text{ m}$ and $f \approx 200 \text{ kHz}$, therefore the theoretical group velocity is $U=1948 \text{ ms}^{-1}$. We stress that this values is for a free lamina without any piezoelectric sensor. The experimental values of the

group velocity was estimated on the laboratory model of the Impact Sensor (Esposito et al., 2002), stimulating the plate in different positions and measuring the relative time delays with which the signal arrives at one of the PZT sensors. The value obtained is $U=(1711 \pm 60) \text{ ms}^{-1}$.

The test performed during the pre-flight calibrations (Esposito, 2000; Esposito et al., 2002) shows that the IS response depends on the impact positions.

3.2.3 Micro-Balances System

The Micro-Balances System (MBS) consists of a network of five Quartz Crystal Microbalances (QCM), model QCM MK21, by *QCM Research*, oriented towards five different directions, in particular: *QCM1*, *QCM2*, *QCM3*, *QCM4* and *QCM5* are oriented along the $+X$, $+Y$, $-X$, $-Y$ and $+Z$, respectively. Each QCM has a field of view of 40° . The QCMs are installed on top of the GIADA structure, as shown in Figure 19, and, with the exception of *QCM5*, are all tilted upwards the X - Y plane by 20° in order to reduce possible obstructions in the field of view.

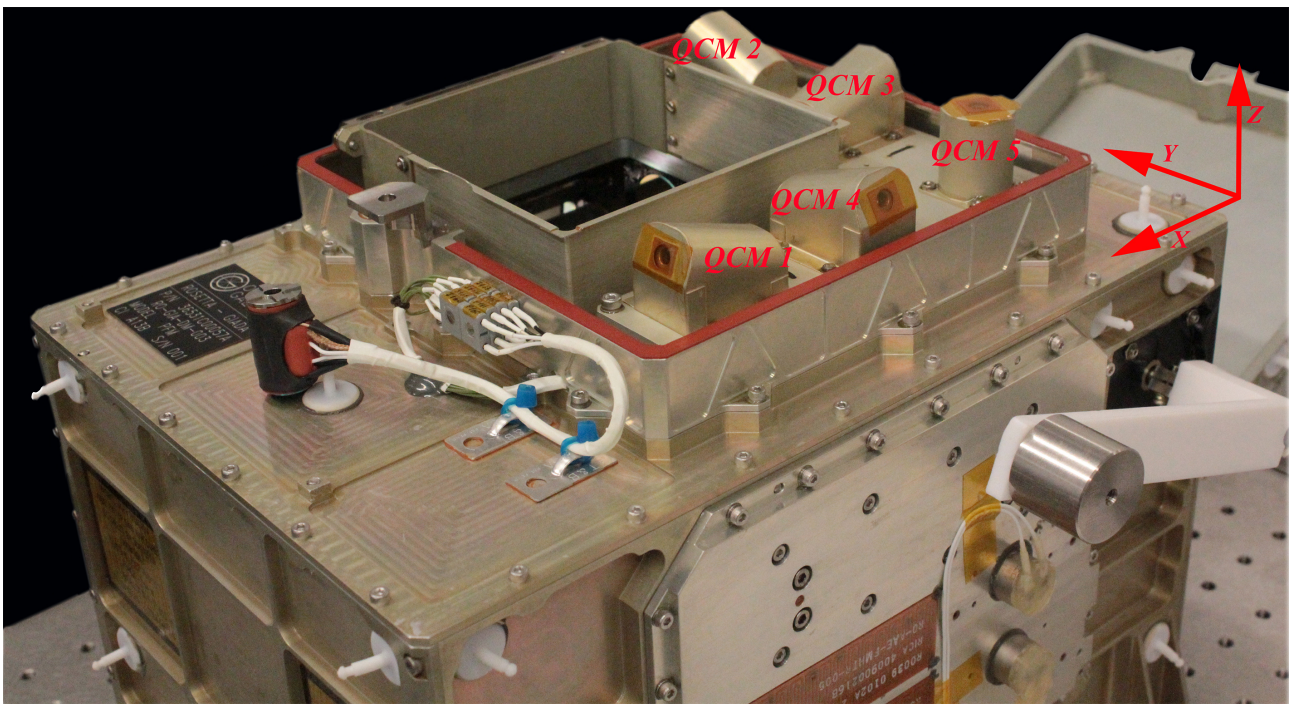


Figure 19: An image of the 5 QCMs placed on top of the GIADA Proto-Flight Model., with the relative number and the reference system.

Each microbalance is composed of two quartz crystals oscillating at 15 MHz , one is acting as the sensor, (exposed to the dust environment) and the other is the reference. The two crystals are shifted in frequency of approximately 1 kHz , in particular the reference has a frequency $f_r > f_s$, where f_s is

the frequency of the sensor. The beating frequency between the two crystals, $f=f_r-f_s$, is proportional to the mass deposited on the sensor. Indeed, when the mass accumulates on the sensor, f_s decreases, while f_r remains constant, therefore f increases. The beating frequency of the GIADA QCMs, whose dependence from the temperature and power supply fluctuations has been characterized (Palomba et al., 2002), is actually measured and by means of the proximity electronics included in each QCM. This is the input of the main electronics.

The nominal mass sensitivity of the QCMs is $5.09 \cdot 10^8$ Hz/g/cm², considering that each one has an exposed sensing surface of about 10^{-5} m², the resulting mass sensibility is equal to $5.09 \cdot 10^{-9}$ g/Hz. This factor connects the collected amount of mass with the frequency change. The saturation of the sensor occurs when the beating frequency reaches about 1% of the resonant frequency. The GIADA QCMs have the saturation limit fixed at 1×10^{-4} g and measure the cumulative deposition for dust grains smaller than 10 μm, indeed larger particles have a poor mechanical coupling with the crystal surface with respect to smaller particles and do not produce any detectable frequency variation (Palomba et al., 2002).

Each QCM is equipped with a heating device, that has a threefold purpose: 1) to remove volatile materials from the sensitive surface; 2) to check the frequency vs. temperature behaviour; 3) to perform, for temperature lower than 100°C, thermo – gravimetry² analysis on the collected dust.

3.3 Main Electronics

The whole instrument is controlled by the Main Electronics.

The ME interfaces with the spacecraft and the proximity electronics of the three GIADA subsystems, also acquires and pre-processes the data. GIADA is a cold-redundant instrument³: the GIADA ME is based on two complete sets of interfaces with the spacecraft (data and power). The ME includes: the microprocessor, the memory and some digital-analogue circuits, which are in cold redundancy for low power operation. The switch between the main and the redundant Electronic is under control of the spacecraft by switching from the Main to the Redundant power lines; this

² Thermo-gravimetry is a method of analysis that study the variation in mass of a sample as a function of temperature or time, by means of continuous recording of this variation in a controlled atmosphere.

³ The redundancy is a common approach to improve the reliability and availability of a system, often used in space missions and instruments to increase their ability to survive. In cold-redundancy the secondary unit is powered off, thus preserving the reliability of the unit and to switch between main and redundant configurations the system has to be power off.

switch over can be executed by a GIADA power cycle: Switch-off of the Main followed by a Switch-on of the Redundant, and vice versa.

The Main and Redundant interfaces with the spacecraft, i.e. the CPU (Central Processing Unit, based on a 80C86 microprocessor) and the Power supplies (PSU), are physically separated in two boards (CPU-PSU) located side by side at the bottom of the IS sub-system.

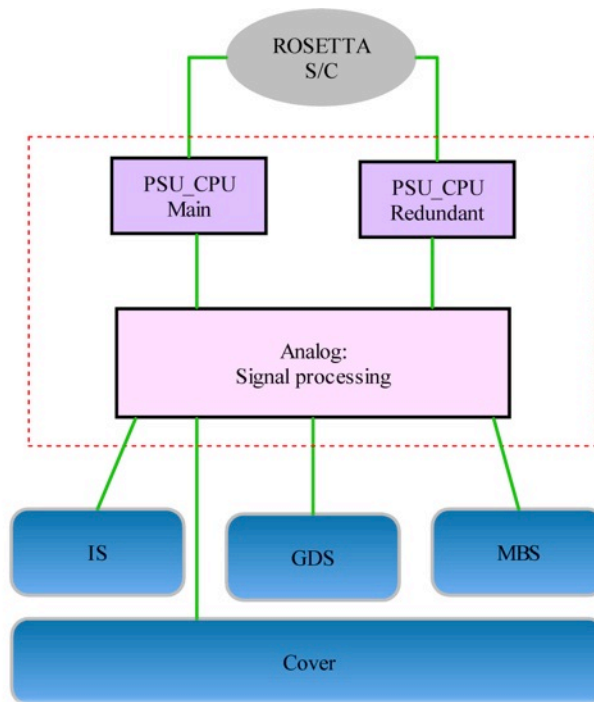


Figure 20: Block diagram of the GIADA Main Electronics.

The Analog Signal Processing (ASP) block controls and manages GIADA functionalities (including the Cover activation), manages the ME internal calibration, monitors the current on the different power lines and collects the housekeeping read from different GIADA sensor (Colangeli et al., 2007). The APS acts also on the three detection sub-systems of GIADA.

When an event is detected by the GDS, the ASP acquires the peak amplitude, measures the crossing time of the grain in the laser curtain, and starts the clock to measure the time of flight between GDS and IS. This clock is stopped either when one of the PZTs detects the grain or after 330ms (reset time). In consequence of a grain impact detected by a PZT, the ASP starts the clocks related to each PZT to measure the propagation time of the flexural wave generated in the IS plate. These clocks are stopped when the corresponding PZTs detect the event. For all piezoelectric sensors ASP generates the protocol to acquire the peak amplitude of the PZT signal. Also the PZT Calibrator is controlled by the ASP.

About the MBS sub-system the ASP measures the frequency of each QCM and, by means of a specific tele-command request, activates the heater for the heating cycle of microbalances, one at time.

Analog Signal Processing controls the power supply of the lasers in the illumination system.

The measurement sensors are intrinsically redundant; in fact both the GDS, the IS and MBS's are composed by several sources or detectors working in parallel. About GDS, if two of the four laser light sources or some of the eight-photodiode detectors fail, the sub-system is still operating, but the sensitive area will be reduced. Similarly, for the IS are sufficient 3 PZT detecting sensors to obtain the particle momentum measurement. Finally, in case of malfunction of one or more microbalances, the measurement of the dust flux is however achieved on the remaining directions.

The GIADA on-board software foresees 4 operational modes for the instrument:

- **Safe:** is the mode the Main Electronics is initialised. In this mode all the GIADA subsystems are off (GDS, IS, MBS) and cannot be switched On.
- **Cover:** this mode allows working with the Cover (Open and Close), the Frangibolt (test and activation) and testing the paired heaters (Cover-Frangibolt and Cover-Motor). In this mode all the GIADA subsystems are off (GDS, IS, MBS) and cannot be switched On
- **Normal:** it is the mode where all the sensors are active by default, is the baseline to be used in nominal S/C and instrument operational conditions. In case of contingency, a sub-set of the GIADA sensors can be disabled. In this mode it will be possible to perform auto-calibrations and to manage contingencies, either autonomously or by OBCPs.
- **Flux:** this mode is designed to be used during the “mapping” phase of the mission, both for power saving reasons and because the expected event rate does not justify the switching-on of the single grain detection (GDS + IS) sub-systems. This is the mode in which by default MBS is ON and the other subsystems cannot be switched ON.

The software has been developed in order to switch from one Mode to another should always go through the Safe Mode, as shown in Figure 21:

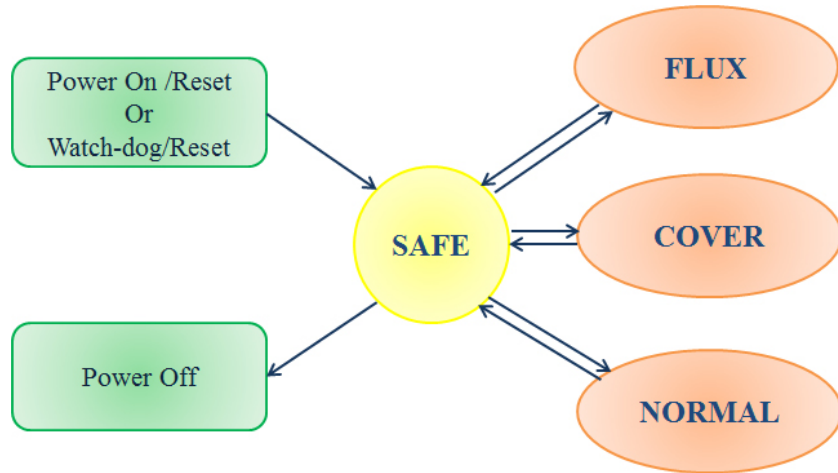


Figure 21: The structure of the GIADA operation modes (Colangeli et al., 2007)

In **Table 8** are reported the power instrument for the four GIADA operational Mode, while in **Table 9** are reported the main configurable measurements and operational parameters for each GIADA sub system.

| <i>Interface</i> | <i>Primary instrument power</i> |
|------------------------------------|---|
| Maximum Average Input Current @28V | |
| Safe Mode | I=0.154A |
| Cover Mode | I=0.950A (During Frangibolt Activation) I=0.700A(during closed/open Cover operation) |
| Flux Mode | I=0.240A |
| Normal Mode | I=0.740A (Laser Nominal power, i.e. Medium power) |

Table 8: Operational Power Interface characteristics

| <i>Subsystems</i> | <i>Configurable parameters</i> |
|-------------------|--|
| GDS | Laser Power configuration (Medium or Low) Receivers Thresholds AC coupling |
| IS | PZTs Range PZT 4 and PZT5 gain PZTs Thresholds |
| MBS | Heating |
| COVER | Cover Motor Heater Steps to open or close the cover |

Table 9: Configurable parameters for the GIADA sub systems .

4. GIADA state of health during the Rosetta Cruise Phase

The analysis of the data produced by GIADA during the Cruise Phase allowed us to evaluate the health's status of the instrument and to characterize the instrument behaviour with respect to some environmental conditions (e.g. temperatures, solar irradiation). The results of these detailed analyses, performed in the framework of my PhD research, are reported in this chapter.

4.1 The Rosetta Cruise Phase

The *Cruise Phase* is the seven-year period from the Rosetta launch, on the 2nd of March 2004, to the beginning of the spacecraft hibernation. Rosetta travelled 10 years around the inner Solar System and, in order to reach comet 67P/CG with the right velocity and trajectory has been accelerated by a sequence of gravity assist manoeuvres, three at Earth (Earth Swing-by) and one at Mars (Mars Swing-by). The details of the Cruise Phase are shown in Table 10 and Figure 23.

| Phase | Start Date | End Date | Duration (days) | SunDistance (AU) |
|-------------------------------------|------------|------------|-----------------|------------------|
| Launch and Early Orbit Phase (LEOP) | 02/03/2004 | 04/03/2004 | 3 | |
| Commissioning1 | 05/03/2004 | 06/06/2004 | 94 | 0.89-0.99 |
| Cruise 1 | 07/06/2004 | 05/09/2004 | 91 | 0.89-1.04 |
| Commissioning2 | 06/09/2004 | 16/10/2004 | 41 | 1.04-1.09 |
| Earth Swing-by1 | 17/10/2004 | 04/04/2005 | 170 | 0.99-1.11 |
| Cruise 2 | 05/04/2005 | 28/07/2006 | 480 | 1.04-1.76 |
| Mars Swing-by | 29/07/2006 | 28/05/2007 | 304 | 0.99-1.59 |
| Cruise 3 | 29/05/2007 | 12/09/2007 | 107 | 1.32-1.58 |
| Earth Swing-by2 | 13/09/2007 | 27/01/2008 | 137 | 0.91-1.32 |
| Cruise 4-1 | 28/01/2008 | 03/08/2008 | 189 | 1.02-2.03 |
| Steins Flyby | 04/08/2008 | 05/10/2008 | 63 | 2.03-2.19 |
| Cruise 4-2 | 06/10/2008 | 13/09/2009 | 343 | 1.35-2.26 |
| Earth Swing-by3 | 14/09/2009 | 13/12/2009 | 92 | 0.98-1.35 |
| Cruise 5 | 14/12/2009 | 16/05/2010 | 154 | 1.03-2.45 |
| Lutetia Flyby | 17/05/2010 | 03/09/2010 | 111 | 2.45-3.14 |
| Rendez-vousMan1 | 04/09/2010 | 13/07/2011 | 313 | 3.15-4.58 |

Table 10: Detailed description of Rosetta Cruise Phase

On the 8th of January 2011 Rosetta was put in hibernation in order to limit power and fuel consumption, and to minimise operating costs; in fact the high distance from the Sun and the weakness of the sunlight on Rosetta solar panels, would have not allowed to produce enough power to fully operate the spacecraft at distances greater than 4.5 AU. During the hibernation phase only the computer, the command decoders, the radio receivers, and the survival heaters remained active

and automatically controlled to ensure that the entire satellite did not freeze when beyond the orbit of Jupiter, at a maximum distance of about 790 million of km. On the 20th of January 2014 at 10.00 CET, after 31 months of deep sleep at a distance of 673×10^6 km from the Sun, an internal clock has awakened automatically Rosetta. Subsequently the spacecraft oriented itself by means of a star tracker and pointed its antenna toward the Earth sending the signal that confirmed the awake. At 19:18 CET this signal has been received at Mission controllers at ESOC, ESA's Space Operations Centre, Darmstadt, (Figure 22).

Currently Rosetta and its payloads are in the Post-hibernation commissioning, a phase devoted to the re-activation-maintenance and checkout activities for all the instruments in preparation to the rendez-vous with comet 67P/CG. The GIADA post hibernation commissioning started on the 27th of March 2014.



Figure 22: The signal emitted by Rosetta and received by both NASA's Goldstone and Canberra ground stations at 18:18 GMT/ 19:18 CET, during the first window of opportunity the spacecraft had to communicate with Earth. It was immediately confirmed in ESA's Space Operations Centre in Darmstadt and the successful wake-up (by courtesy of ESA).

As reported in table 3, few days after the launch a dedicate section was performed to test the instruments functionality, called Commissioning 1. A further commissioning section, Commissioning 2, was performed with the aim to investigate interference issues among the instruments, and to check instruments pointing.

During the whole Cruise Phase 13 tests, called Payload Checkouts (PCs), have been performed for instruments verification and maintenance. Payload Checkouts, performed at different heliocentric distances (see Figure 23) were named Passive or Active.

The Passive PCs, devoted to check the global instruments status following standard procedures, were performed every six months during the whole cruise phase. The Active PCs were devoted to test the instruments behaviour in different configurations and the possible interference among payloads. These tests were performed before the execution of each critical operation of Rosetta, e.g. scientific phases such as the swing-by of Earth or Mars and the fly-by of asteroids.

Figure 23 reports the Active and Passive Checkouts (PCs) dates Vs heliocentric distances.

The GIADA subsystems behaviour was monitored by means of the self-calibration data collected during the different PCs. The analyses of functional parameters stored by GIADA provide information about the instrument's health status.

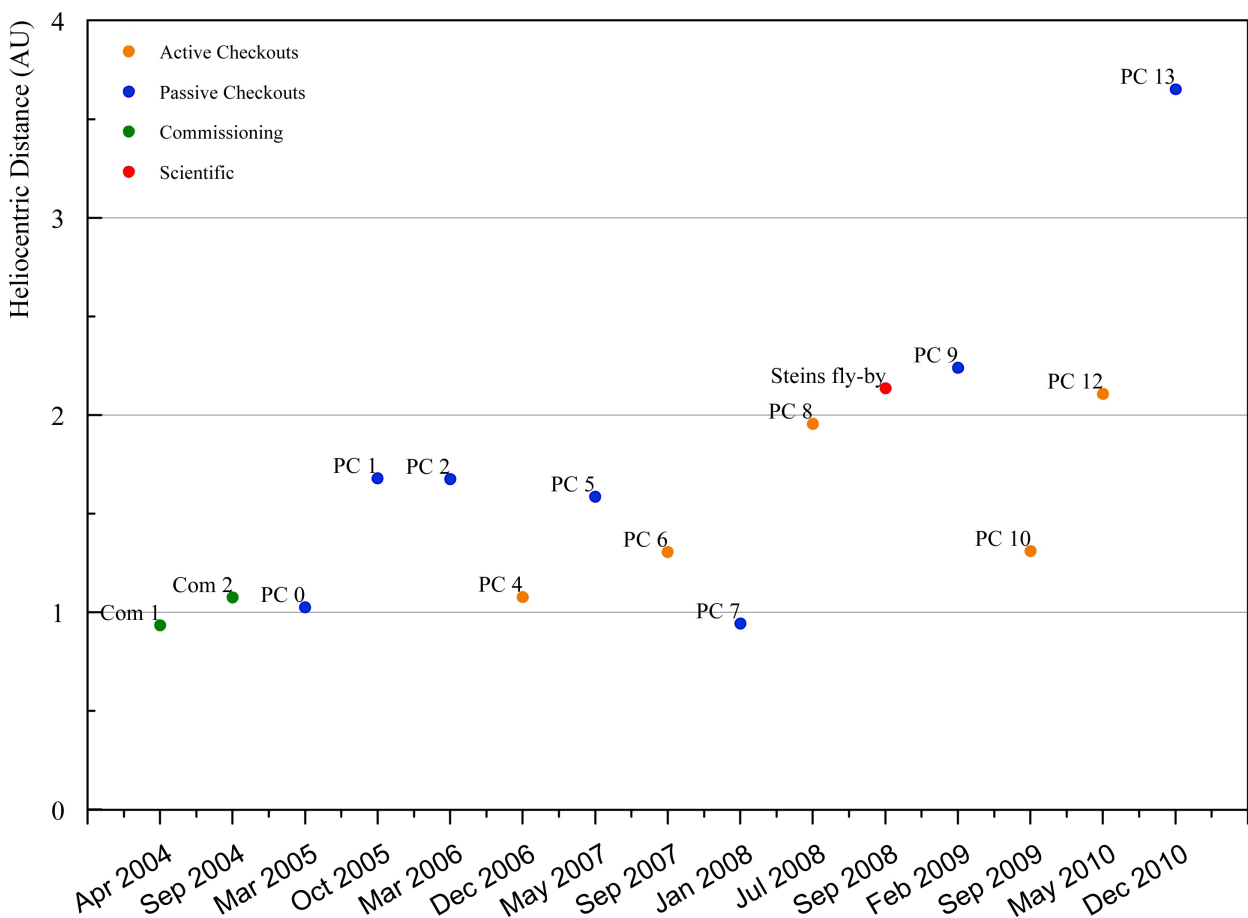


Figure 23: Satellite operations during Cruise Phase, which GIADA was activated, collecting data

4.2 Payload Checkouts Analysis

In order to verify GIADA health status from Commissioning 1 to Payload Checkout 13, the calibration data produced by the three GIADA sub-systems GDS, IS and MBS were analysed.

In addition, the cover mechanism behaviour and the functional parameters (e.g. power consumption, temperatures, etc.) were monitored and carefully analysed. All the tests were performed using sequentially the two instrument interfaces: Main and Redundant.

The Power Consumption trend, starting from the Commissioning till the last PC before the hibernation phase, is reported in Table 11. It is evident that the Power Consumption in Normal Mode (see section 2.4) remains nominal and stable during the whole Cruise Phase.

| Mission Phase | Power Consumption (W) |
|----------------------|----------------------------------|
| Commissioning | 23.4 |
| PC 0 | 22.9 |
| PC 2 | 21.9 |
| PC 6 | 22.1 |
| PC 9 | 22.0 |
| PC 13 | 22.0 |

Table 11: Power Consumption of GIADA instrument in Normal Mode configuration with all subsystems ON, during some PCs

4.2.1 Cover activation analysis

The Cover is a critical component of the instrument; in fact its malfunction may compromise the ability of GIADA to collect data. Therefore during the Cruise Phase, the cover mechanism behaviour has been well characterized. Some non-nominal conditions for the mechanism have been observed.

The analysis of the housekeeping during activations, obtained by the reed switch monitoring the cover positions (open/close), allowed a full understanding of the mechanism behaviour.

Assuming that the cover is in the closed position, after the COVER OPEN command, the expected trend for the reed switch data should be:

- The reed switch (named RW_CLOSE), which indicates the Cover-Close position, is activated (the signal raises to the high level) after the start of the opening operation and for a short number of steps (29 steps expected), then the signal falls to the low level (see red line in Figure 24a).
- The reed switch (named RW_OPEN), which indicates the Cover-Open position, is activated after an expected number of steps (nominally 125), as blue line indicates in Figure 24a.

Assuming the cover in open position, after the COVER CLOSE command, the expected trend for the two reed switch data should be exactly the same, swapping RW_CLOSE with RW_OPEN, as shown in Figure 24b.

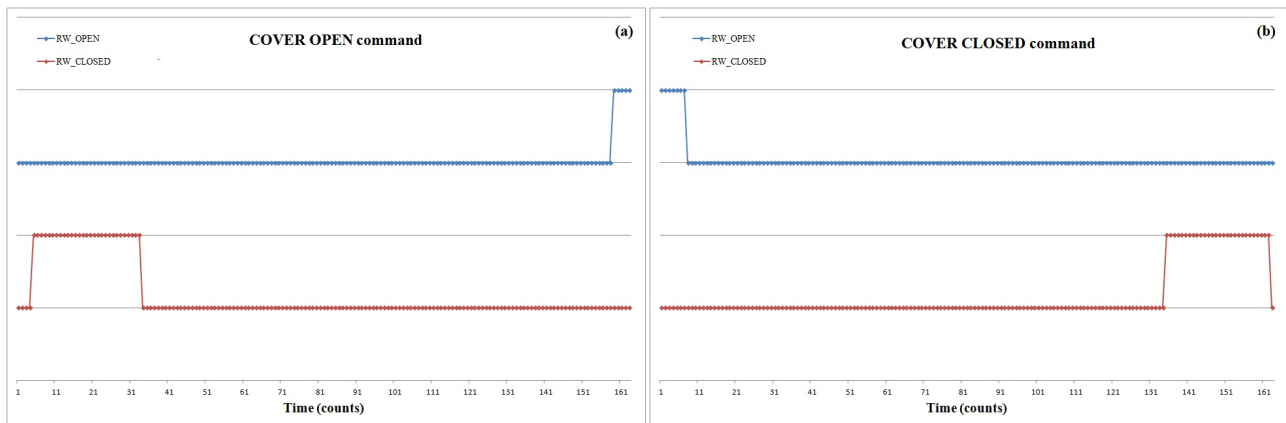


Figure 24: Typical signals produced by the correct OPEN (a) and CLOSED (b) Cover activation for GIADA. RW_OPEN is active when its value is equal to 2, RW_CLOSED is active when its value is equal to 1.

The cover mechanism activations that show anomalies or non-nominal behaviour are described in the following.

Commissioning 1: At the first COVER_OPEN command, the cover resulted not completely open, as it can be inferred from Figure 25a. In fact, the housekeeping reports an activation of the RW_CLOSED not followed by the activation of the RW_OPEN, as expected for nominal behaviour shown in Figure 24a. In order to reach a complete opening of the cover, a further COVER_OPEN command has been sent (Figure 25b).

At the end of the operation used for the Redundant Interface testing in the Commissioning 1, two consecutive COVER_CLOSED commands have been sent to the instrument. The first provided directly by the timeline procedure; the second as part of an automatic procedure to switch off GIADA. The reed switch behaviour is shown in Figure 25c and Figure 25d. Moreover, a second switch on with main interface, foreseen in the test sequence, and the following automatic procedure to switch off GIADA commanded a third close cover (see Figure 25e).

During the power-off, the On Board Control Procedure (OBCP) “Close Cover” closed automatically the GIADA cover, despite its actual position. Since the cover was already closed, the new close cover operation resulted (as expected) in a continuous cover bunching over the cover support. This is the reason of the status of the two reed-switches shown in Figure 25d and Figure 25e, in which the reed switch indicating the Cover-Open position remains always not active and the other is active several time.

The in depth analysis of the reed switch signal indicates that, at the end of the Commissioning 1, the GIADA cover remained partially open. This conclusion is confirmed by the result of the COVER OPEN command sent at first GIADA power on during the Commissioning 2 (Figure 25f).

Commissioning 2: At the end of one of the tests foreseen in the Commissioning 2 (Pointing 1), an anomalous behaviour for the cover mechanism has been observed. The GIADA cover, already closed by a previous Close Cover command, received an automatically OBCP Close Cover at the end of the test. The second close cover command resulted unexpected: the cover reversed its movement and it came to the open position. This is in line with the status of the two reed-switches in Figure 25g. This behaviour was recovered by a dedicate action, as shown in Figure 25h, performed few hours after the Pointing 1.

The same behaviour occurred during the Close Cover operation at the end of Payload Checkout 7 (Figure 26b). In this case, the recovery action (Figure 26c) was performed ten days after the end of GIADA timeline.

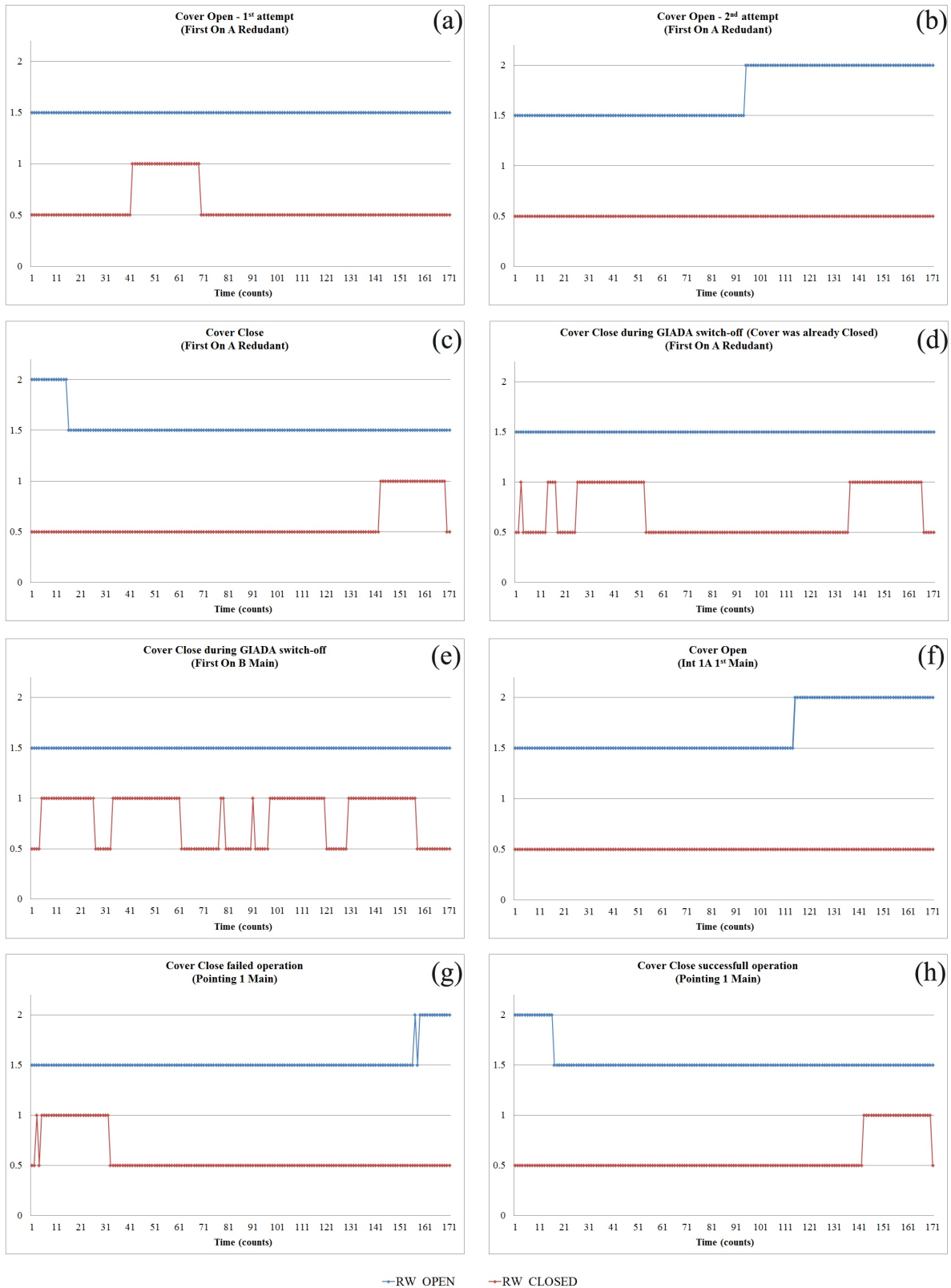


Figure 25: Plots describing the Cover Report during the non-nominal behaviours. (a) First OPEN failed command during the First ON A Redundant; (b) Second OPEN, successful command, (c), (d) and (e) multi CLOSED command producing the partial opening of GIADA Cover; (f) First Cover Opening during Commissioning 2: the absence of RW_CLOSED activation signal shows that GIADA cover remained partially open between Commissioning 1 and Commissioning 2; (g) COVER CLOSED command during Pointing 1 producing the opening of the COVER and (h) the recovery operation to close the cover during Pointing 1.

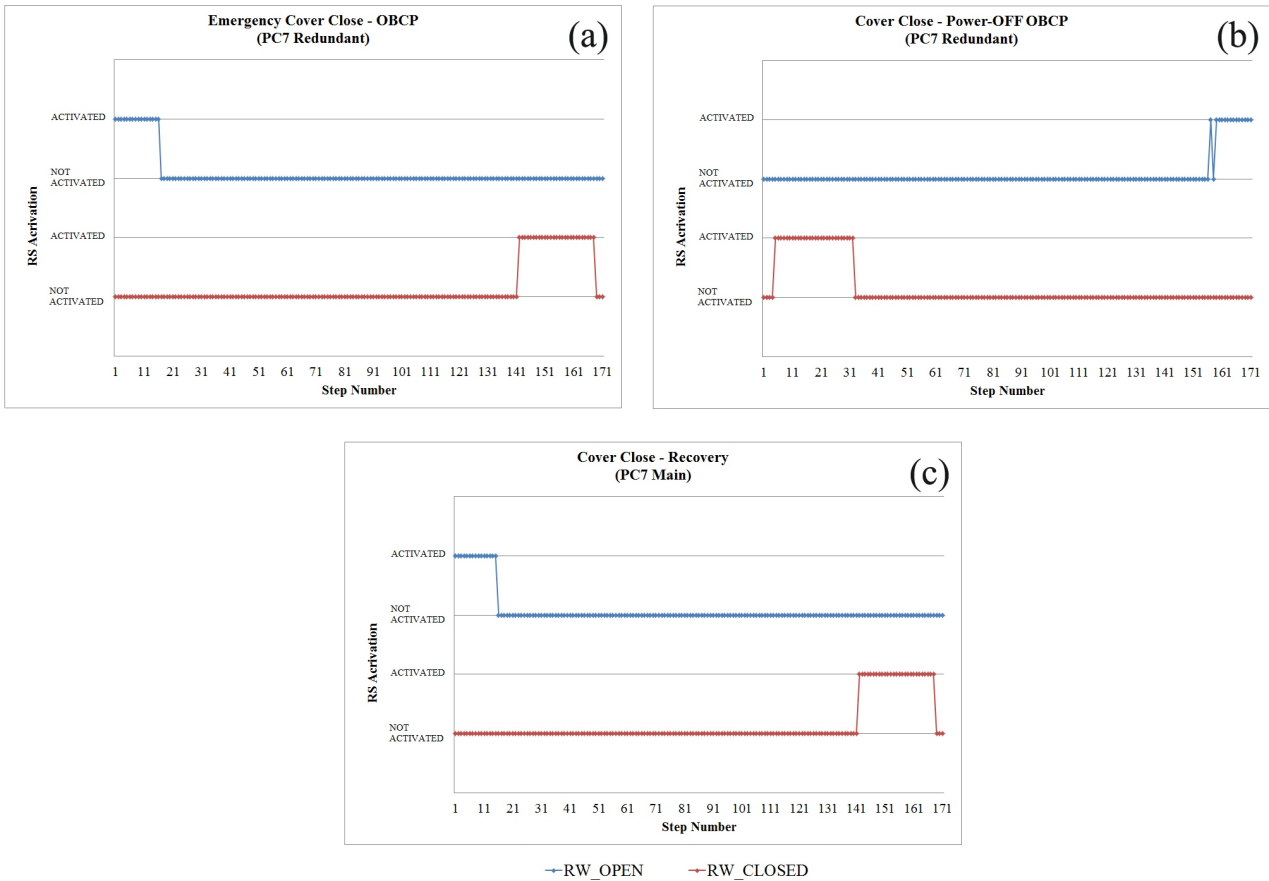


Figure 26: The anomalous behaviour during the PC 7: During the power-off, the GIADA cover is automatically closed by the OBCP Close Cover, a further command Close Cover reversed the motor movement and the Cover came to the open position (b). Ten days after the GIADA Team executed a dedicate Recovery section to evaluate the instrument status and perform the Close Cover (c).

4.2.2 Data Analysis

To monitor how the measurement subsystems behaviour evolved during the cruise phase, the calibration data produced by GDS, IS and MBS systems were analysed. In fact, for each subsystem, benchmark data can be obtained independently from actual dust grain detections.

The data downloaded by the spacecraft, are raw telemetry data. ESA Space Operations Centre after a first processing for each instrument saves them as *Data Disposition System (DDS)* in binary format. The DDS files are then distributed to each instrument team. Once GIADA team has downloaded these data, they are converted into *Planetary Data System (PDS)* format, defined by NASA, containing the engineering parameters in decimal format (Aronica, 2009). Data analysis reported in the present work was performed on PDS files, using the National Instruments DIAdem 2010 software.

Micro Balances System

Concerning the MBS, for each QCM the trend of its frequency and the stability vs. temperatures (QCM heating procedure) were analysed.

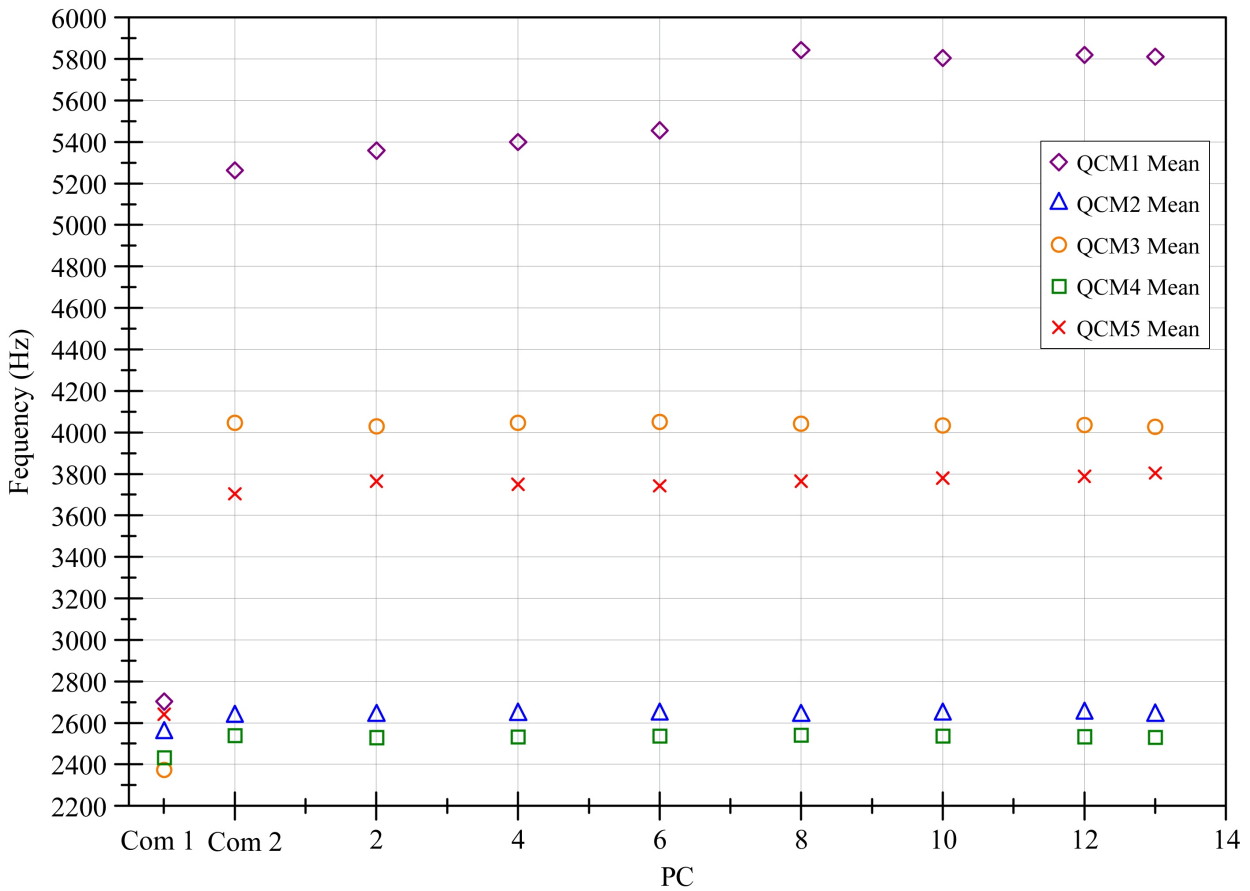


Figure 27: Frequency mean values for the five QCMs measured during the payload tests performed in the cruise phase before the hibernation (Della Corte et al. 2014).

Figure 27 shows QCMs frequency values for each switch on during the Cruise Phase. For *QCM1*, *QCM3* and *QCM5*, we can observe two significant increments of frequency. The first variation has occurred in the elapsed time (169 days) between the last switch off during Commissioning 1 and the first switch on during Commissioning 2 (Table 10); the second increment, concerning only *QCM1*, occurred at the end of PC7, when GIADA cover remained open for ten days. These increments are calculated considering the nominal value of sensibility reported in section 2.3. To correctly evaluate the frequency increase, the QCM readings were scaled taking into account the frequency vs. temperatures dependency. The results of these analyses are reported in Table 12 and are directly connected with the cover behaviour described in the previous section (3.2.1).

These frequency increments have been interpreted as due to mass deposition on the QCM sensors. The collected mass probably consisted in low volatility material. Dedicated heating cycles, during Commissioning 2 for each QCM, in order to remove or to reduce the contamination were performed (see Figure 28 right). Further heating cycles have been performed during the following PCs: the

highest temperature reached was about 80 °C. No significant frequency decrease has been observed following these actions, indicating that no evaporation of the material occurred. The microbalance that collected the greatest amount of contamination is *QCM1*, whose sensitive surface is exposed in the +X direction. This can be explained by the cover mechanism design: in case of partial closing, such as those actually occurred (described in section 3.2.1), internal surfaces in the +X direction are the more exposed.

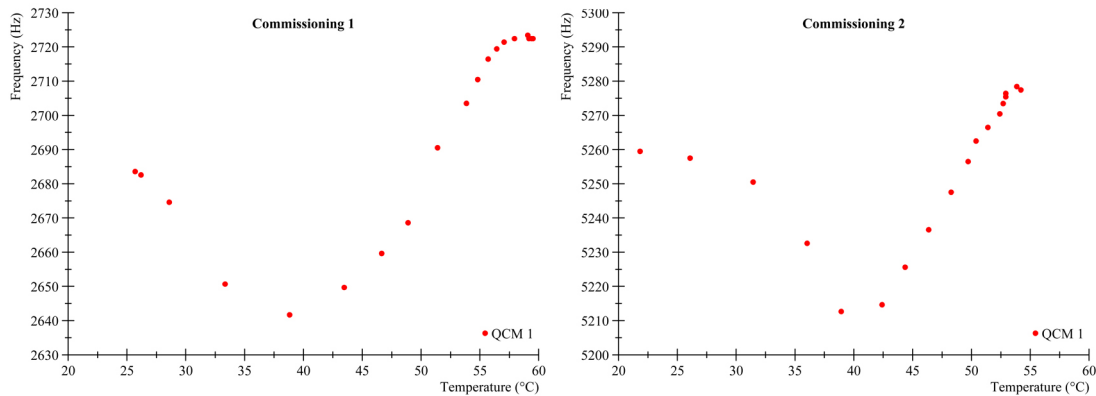


Figure 28: Frequency behaviour vs Temperature for QCM 1 during heating process: data acquired during Commissioning 1 (Left) and Commissioning 2 (Right), (Della Corte et al. 2014).

Considering the microbalances sensitivity, we have calculated the deposited mass for every QCMs in the reported events whose results are summarized in Table 12.

| | QCM 1 (+X) | QCM 2 (+Y) | QCM 3 (-X) | QCM4 (-Y) | QCM5 (+Z) |
|--|----------------------|----------------------|----------------------|----------------------|----------------------|
| Comm. 1 (Hz) | 2683 | 2543 | 2377 | 2443 | 2638 |
| Comm. 2 (Hz) | 5258 | 2613 | 4063 | 2557 | 3690 |
| Δv (Hz) | 2575 | 70 | 1686 | 114 | 1052 |
| $\Delta M/day$ (g/day) | $7.67 \cdot 10^{-8}$ | $2.11 \cdot 10^{-9}$ | $5.08 \cdot 10^{-8}$ | $3.43 \cdot 10^{-9}$ | $3.17 \cdot 10^{-8}$ |
| M_{tot} (g) | $1.31 \cdot 10^{-5}$ | $3.56 \cdot 10^{-7}$ | $8.58 \cdot 10^{-6}$ | $5.80 \cdot 10^{-7}$ | $5.35 \cdot 10^{-6}$ |
| PC7 Main (Hz) | 5417 | 2605 | 4082 | 2633 | 3672 |
| PC7 Recovery (Hz) | 5743 | 2595 | 4090 | 2633 | 3666 |
| Δv (Hz) | 326 | -10 | 8 | 0 | -6 |
| $\Delta M/day$ (g/day) | $9.81 \cdot 10^{-9}$ | - | - | - | - |
| M_{tot} (g) | $1.66 \cdot 10^{-6}$ | - | - | - | - |

Table 12: Frequency variation for the five QCMs between Commissioning 1 and Commissioning 2 (up) and between PC7 Redundant and PC7 Recovery (down). The two rows highlighted in gray show the contamination estimated on the micro balances during the two phases: the mass is calculated considering the nominal value of sensibility for the QCM MK21 equal to $5.09 \cdot 10^{-9}$ g/Hz. Before to evaluate the frequency increase, we scaled the QCM readings taking into account the frequency vs. temperatures dependency (Della Corte et al. 2014).

It is possible, even if highly unlikely, that the mass collected by the microbalances consisted in interplanetary or interstellar dust particles (*Grün et al., 1997*). Most probably the mass collected has to be attributed to the deposition of volatile contaminants released by the spacecraft: ROSINA, the mass spectrometer on board Rosetta, measured the gas diffused by the spacecraft contributing to maintain a relatively permanent thin gas cloud around it (*Schläppi et al. 2010*).

Despite the probable contamination, the five QCMs maintained a nominal behaviour and functionality. The only minor consequence is that the most contaminated microbalance, *QCM1*, reduced its theoretical dynamical range of about 2%. The frequency increment does not affect the sensor calibration and its behaviour vs temperature; as an example, in Figure 29 the frequency vs temperature trend is shown for *QCM4* before and after mass deposition: the curves remained identical, showing only a frequency translation. The same behaviour has been observed for all the QCMs.

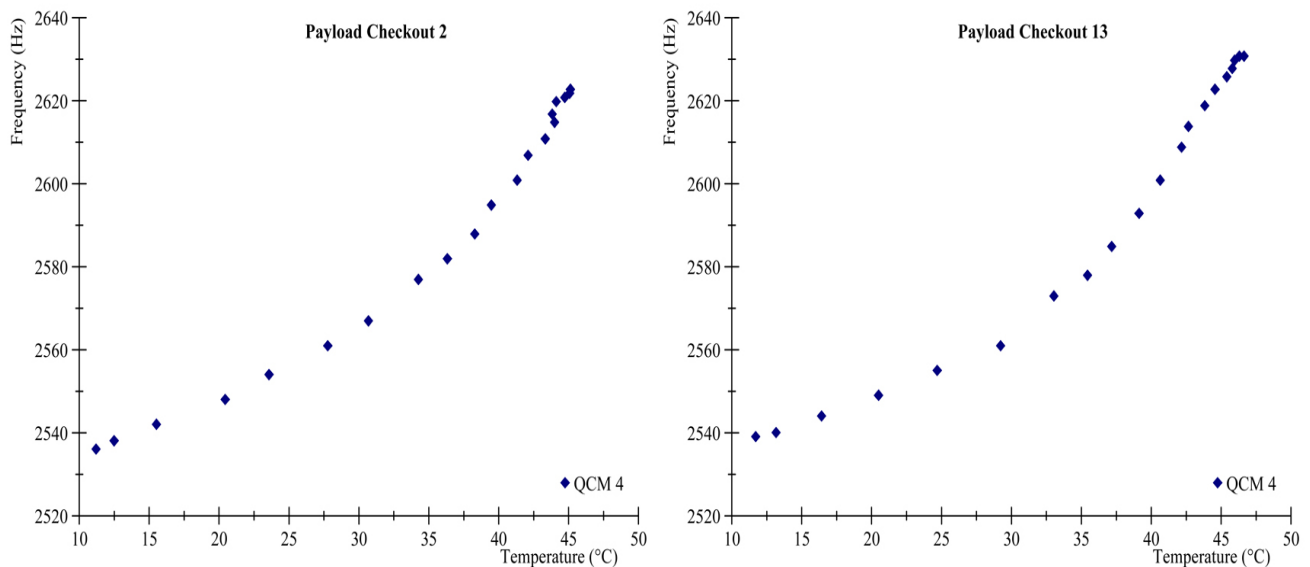


Figure 29: Frequency behaviour vs Temperature for QCM 4 during heating process: data acquired during PC 2 (Left) and PC 13(Right), (*Della Corte et al. 2014*).

For each QCM we also studied the frequency vs. temperature dependency for an extended temperature range, i.e. utilizing the MBS data collected during all the heating cycles performed; as an example in Figure 30 this dependence for QCM 2 is reported.

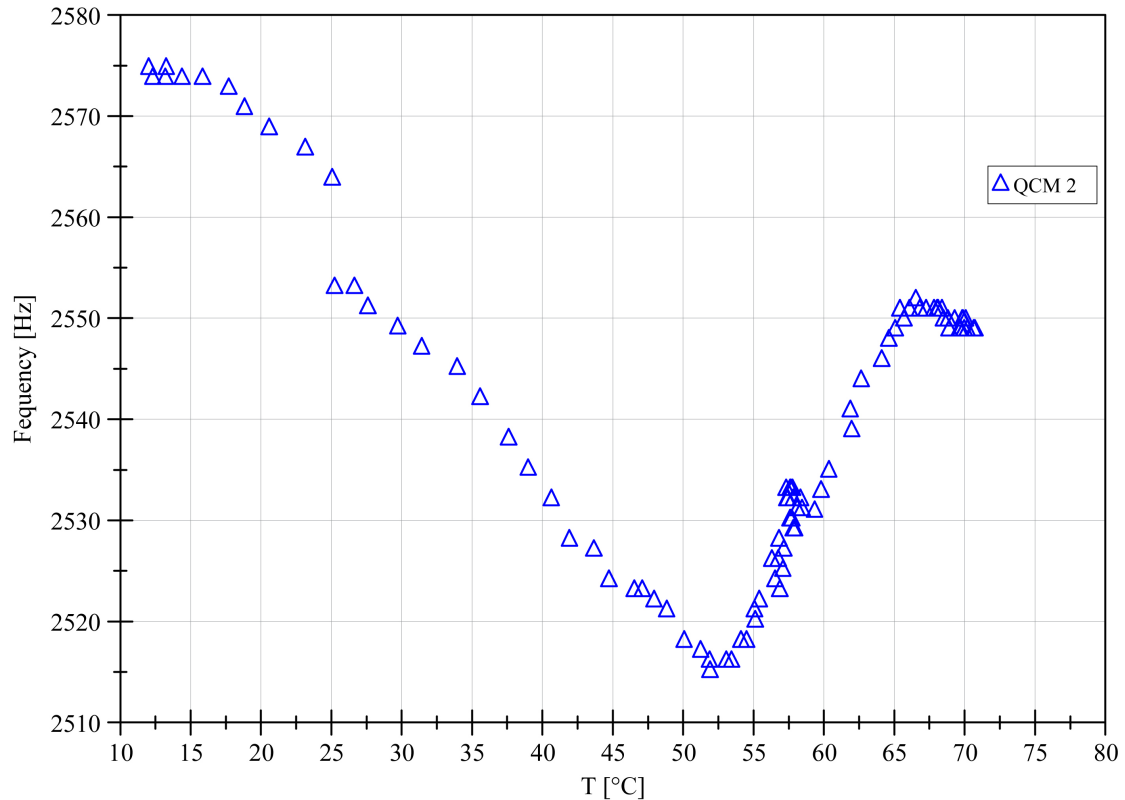


Figure 30: Frequency vs. temperature trend for the QCM 2 plotted following the data collected during the whole cruise phase (Della Corte et al. 2014).

Impact Sensor subsystem

As described in session 2.2, the Impact Sensor (IS) subsystem is equipped with an internal calibrator (PZT Cal) that produces a pulse of fixed amplitude exciting the sensitive plate. In particular, as established in the GIADA software, the PZT Cal stresses the aluminium plate by means of 4 stimuli of 10 V repeated every 5 minutes during the self-calibrations performed in each PC. By means of the internal calibrator, we can check two IS parameters: the sensitivity and the impact induced wave propagation. Figure 31 displays the mean value of the signals recorded by the five piezoelectric sensors (left panel) and the wave propagation time delays induced by the activation of the internal calibrator during the cruise phase (right panel). It is evident that during Commissioning 1 and Commissioning 2 the low signals of PZT3 and PZT5 are due to an incorrect assessment of their detection thresholds. Between PC0 and PC2, new threshold values have been tested to solve this issue. After the last thresholds updating, performed before PC2, the recorded PZT3 and PZT5 amplitudes and time delays remained quite stable during the following payload checkouts. Figure 31 (right) shows that the incorrect assessment of the detection thresholds affected also the measurement of the time delays for PZT3 and PZT5.

The IS subsystem shows good response stability with respect to the temperature sensors. In fact, comparing the different PZTs signal values between PC7 (IS plate temperature reached 49 °C) and PC2 (IS plate temperature of about -4 °C), there are not significant differences.

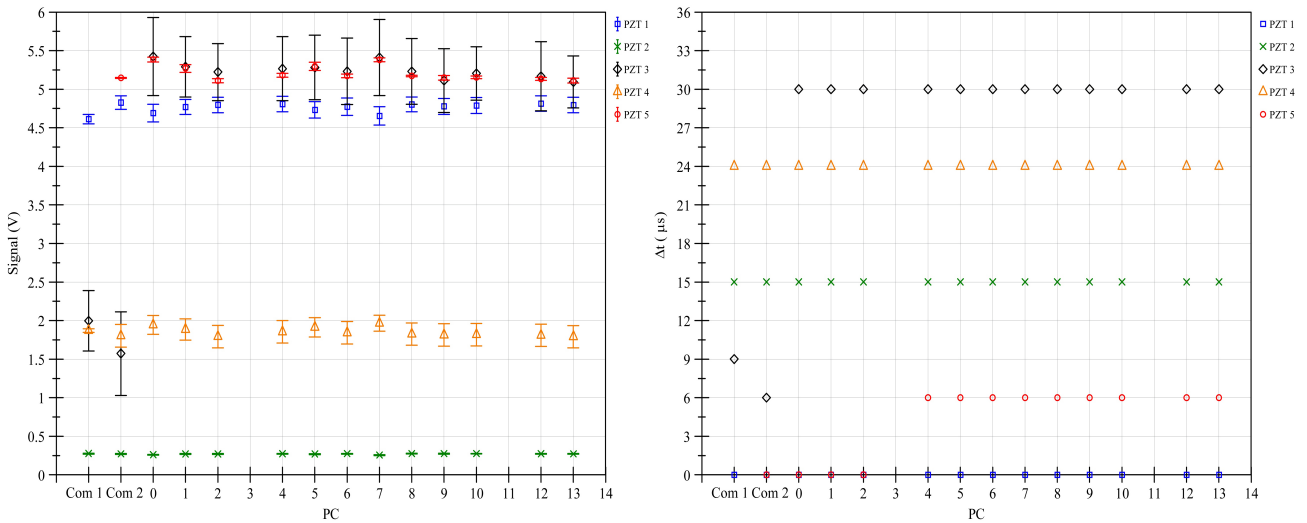


Figure 31: (Left) Mean values of the signal detected by the five piezoelectric sensors following the stimulation of the internal calibrator during the various Payload Checkouts. (Right) Time delays recorded by the five piezoelectric sensors: due to the geometric configuration of the PZT sensors, the delay recorded by PZT1 is always equal to zero. Variability in the delays recorded for PZT 3 and PZT 5 is due to the incorrect threshold values used until PC 2 (Della Corte et al. 2014).

Grain Detection System

The analysis performed to characterize the GDS subsystem during the cruise phase is focused on the calibration data collected both during the normal PCs and Commissioning Phase. In order to evaluate the effects of the sunlight on the GDS subsystem during the Commissioning 2 and during PC6, special pointing sessions have been performed: data collected during these sections showed the behaviour of the GDS with respect to Sun Aspect Angle (SAA), i.e. the angle formed between the spacecraft Z-axis (which is parallel to the Z-axis of GIADA) and the Sun direction in the XZ plane. To study this issue a spacecraft slew has been performed to produce a controlled variation of the angle formed between the spacecraft-Sun direction and the GIADA Z-axis, with step of 5°, in the XZ plane. For each angle the recorded signal of the two GDS receivers was analysed. The behaviour of the GDS signal with respect to SAA is reported in Figure 12. We can notice that the Left channel (red circles) is saturated between 30° and 75°, while the Right channel (blue rhombus) is saturated for angle up to 75°. In this angle's range the saturation is probably due to the large amount of Sun light that, directly or by multi reflection, strikes the receivers. Indeed this amount of light, collected by the receivers, generates a signal higher than the span of the GDS receiver's first amplification stage. As explained in section 2.1 the GDS receivers Proximity Electronics performs

an AC coupling dedicated to eliminate the DC contribution to the signal. Since this coupling occurs after the first amplification stage, it results ineffective in case of high level direct solar illumination at Sun distances $< 2\text{AU}$ (Della Corte et al., 2014).

In conclusion these analyses show that the signal of the Left receiver results saturated for angles $\geq 25^\circ$ and $\leq 80^\circ$, while the Right channel signal is saturated for angles $\leq 80^\circ$.

These results are useful for the definition of the operational constraints, which will be used as reference to plan the GIADA observations during the scientific phase of the mission.

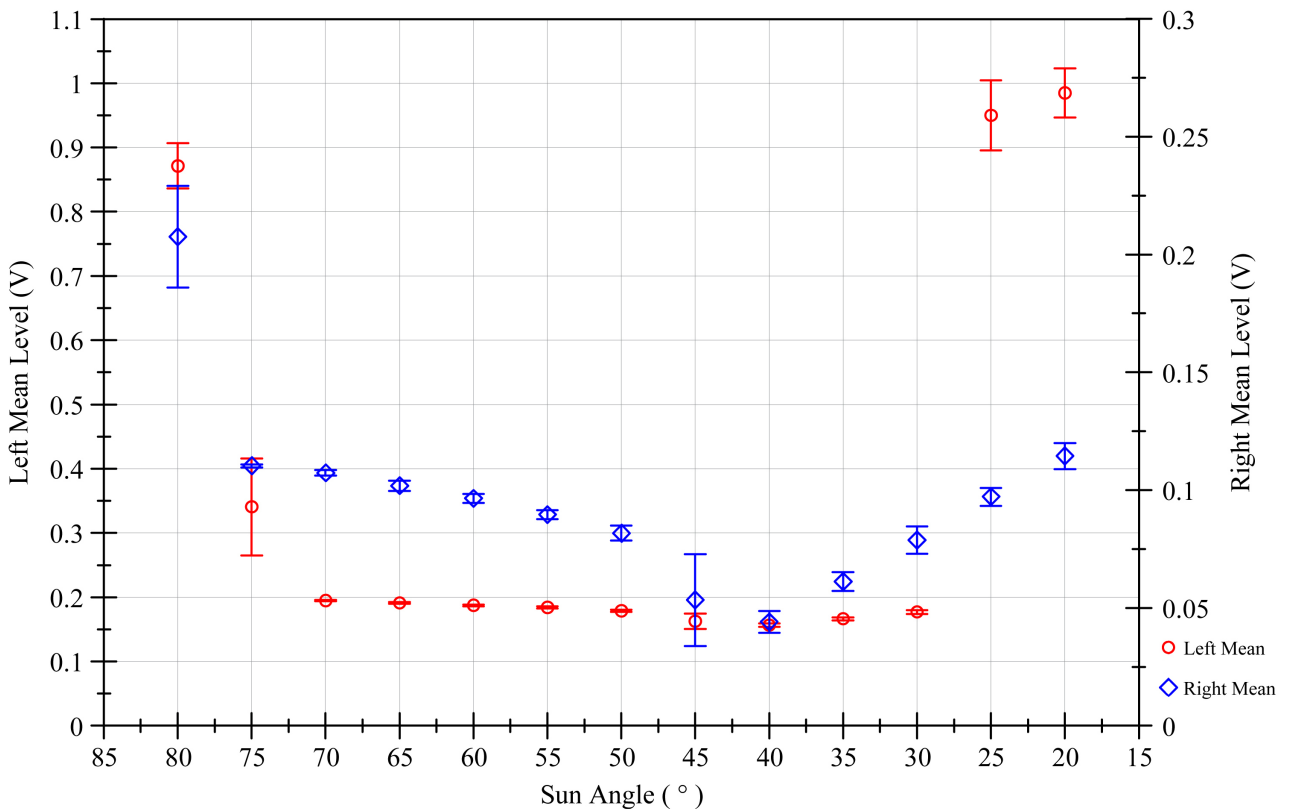


Figure 12: The GDS calibration data obtained during the spacecraft Pointing Test: to evaluate the effect of the direct sunlight on GDS, several calibrations have been commanded during the spacecraft slewing. The data plotted are the GDS output vs. Sun Aspect Angle, i.e. the angle formed between the spacecraft Z-axis and the Sun direction in the XZ plane. The GDS Left channel is saturated when the angle between the S/C-Sun direction and the Z-axis ranges between 30° and 75° , i.e. when the sunlight points directly into the GDS receivers. (Della Corte et al. 2014)

The parameters considered for the GDS performances evaluation during the Cruise Phase are:

- The laser light monitor signal;
- The noise level for the two optical receivers devoted to detect the particle scattering light.

Lasers emission:

In order to evaluate the lasers light emission, the measurements of the monitoring photodiode included in the laser package, named *Light Monitor*, were analysed. Table 13 reports the minimum

and maximum temperatures recorded for the four lasers during the Cruise Phase with the corresponding laser emissions.

The linear dependence between the emitted light and the laser temperature is confirmed by the data, as an example the behaviour of *Laser 1* as a function of temperature is shown in Figure 32. The trend curve confirms the nominal performance of the laser.

| | T_{min} [°C] | Signal level of Light Monitor [V] | T_{Max} [°C] | Signal level of Light Monitor [V] | Light monitor signal dependence on temperature* [V/°C] |
|----------------|-------------------|--------------------------------------|-------------------|--------------------------------------|--|
| <i>Laser 1</i> | -5.6 | 0.518 | 47.9 | 0.383 | - 0.0025 |
| <i>Laser 2</i> | -6.2 | 0.540 | 47.8 | 0.412 | - 0.0023 |
| <i>Laser 3</i> | -5.6 | 0.643 | 48.9 | 0.473 | - 0.0031 |
| <i>Laser 4</i> | -5.9 | 0.623 | 48.4 | 0.496 | - 0.0023 |

Table 13: Evaluation for the four lasers light emissions with respect to the temperature dependence. All the lowest lasers temperatures have been recorded during PC13, while the highest ones are recorded during PC7. (*) The data collected during the whole Cruise Phase show a linear trend vs. Temperature: in the last column, the values of the angular coefficients of the best fit are reported (Della Corte et al. 2014).

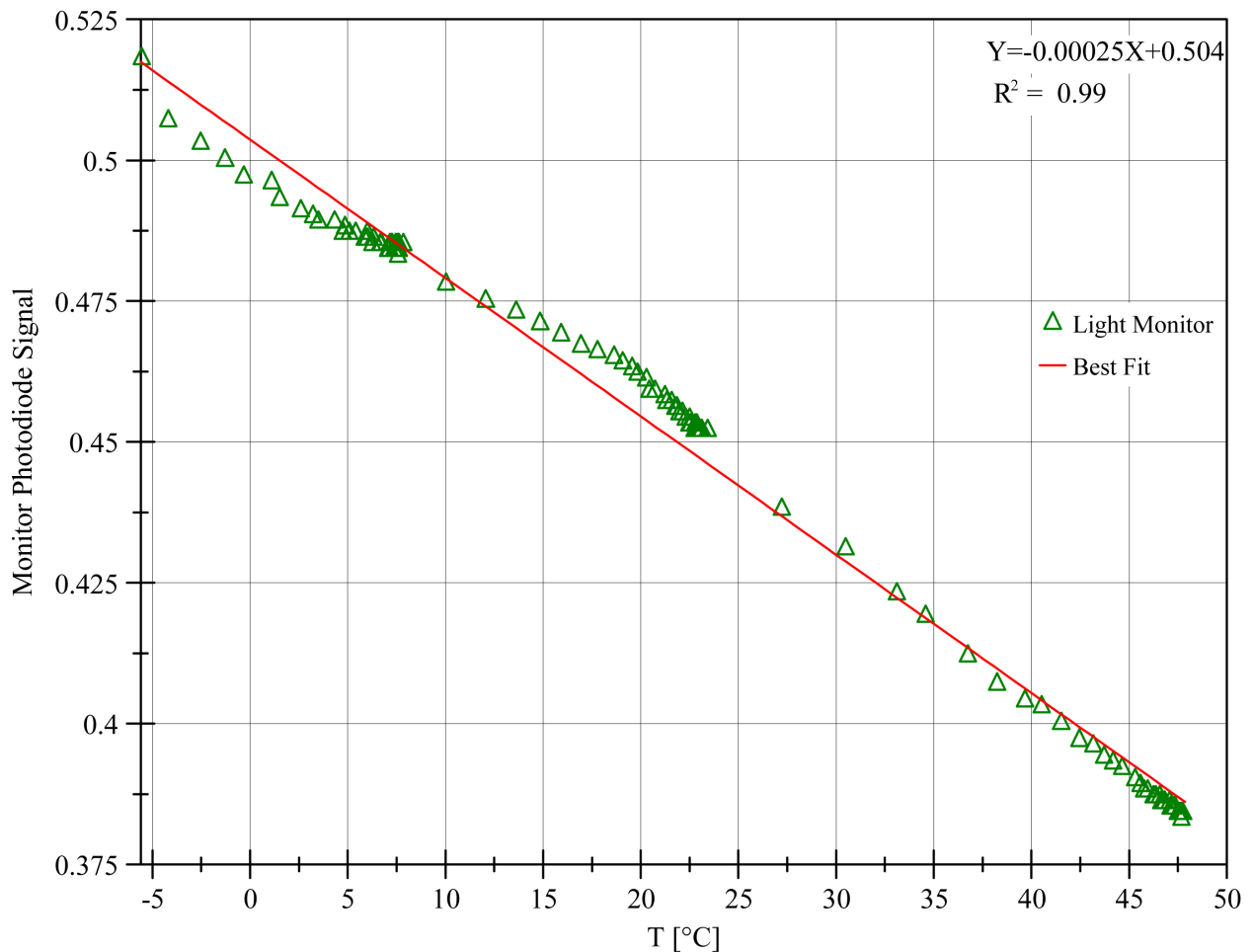


Figure 32: Laser 1 light monitor signal vs. Temperature. The experimental points show an approximately linear dependence between the emitted light and the laser temperature (Della Corte et al. 2014).

GDS receivers

The data analysis of the noise level in the two GDS receivers channel shows a good stability of the sub-systems with respect to the value measured during on ground calibration. As GDS detection performances are related to the channel noise level, we can deduce that the particle detection capability remained almost unvaried during the Cruise Phase. The Payload Checkouts executed during the whole Cruise Phase have been performed with several Sun Angle Aspect vs Z-axis of the spacecraft. Due to these different configurations, as explained in previous section, in five PCs (*PC0*, *PC1*, *PC5* and *PC9*, see Figure 23) the Sun light saturated the detector acquisition chain (see Figure 33b). Figure 33a displays the mean level with the standard deviation for the two GDS receivers, the Right (blue rhombus) and the Left (red circles), as a function of the various PCs when the channels were not saturated. For the left GDS receiver, the slight increasing could be connected with a higher laser emission resulting from lower temperatures reached during *PC10*, *PC12* and *PC13*. This variation modifies only the range of optical cross section measurements, slightly reducing its upper limit.

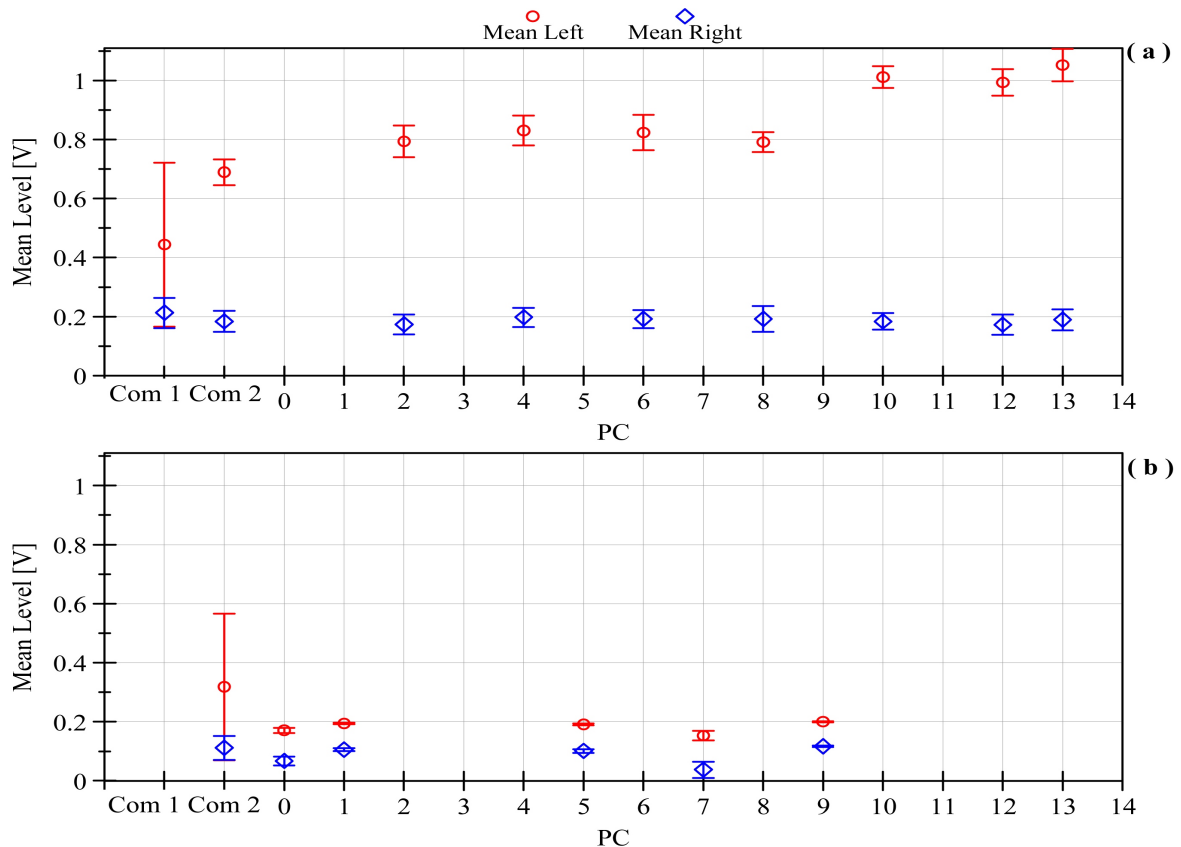


Figure 33: Mean values of the GDS receivers' signals collected during the Cruise Phase: (a) Values for the PCs where the signal is non saturated for the spacecraft geometric configuration; (b) Values for the PCs where the signal is saturated because of the Sun light (Della Corte et al. 2014).

GDS+IS Cruise Phase events

During the Cruise Phase GIADA recorded only three “GDS+IS events”. These recorded events were object of an in depth analysis demonstrating that these are not due to actual dust detection but are generated by electronic noise. For each single event, the dust particle velocity using the GDS laser-curtain crossing time and the time of flight between GDS and IS was derived (Table 14). The obtained velocities have dynamically unrealistic values; therefore these events are incompatible with the passage of actual dust particle. Indeed, the probability to detect a single grain-event, considering a typical PC period of about 12 hours, and taking into account the known interplanetary and interstellar dust fluxes for the size ranges detectable by GIADA (Grün et al., 1997), is about $< 10^{-5}$. The number of false GDS + IS events that had occurred in the whole cruise phase is low and these events are easily identifiable. As a consequence the impact of the false GDS+IS detections on the scientific measurements can be neglected.

| | GDS crossing time [μ s] | GDS velocities measurement [m/s] | GDS+IS time of flight [μ s] | GDS+IS velocities measurement [m/s] |
|-----------------|---------------------------------|---|-------------------------------------|--|
| Commissioning 1 | 30 | 100 | 33720 | 2.97 |
| Commissioning 2 | 30 | 100 | 52520 | 1.90 |
| PC8 | 30 | 100 | 20300 | 4.93 |

Table 14: GDS + IS events measured by GIADA during the cruise phase: the velocities derived using the two times (GDS crossing time and GDS + IS time of flight) are incompatible with a dust grain detection event (Della Corte et al. 2014).

5. Calibration Activity on GIADA Proto-Flight Model

In preparation to the rendez-vous with the 67P/CG, an extended calibration activity on the GIADA Proto Flight Model (PFM), i.e. the spare instrument of the GIADA *in-flight*, was planned. GIADA was already calibrated during the pre-launch calibration campaign ran until 2002 (Mazzotta-Epifani et al., 2002; Esposito et al., 2002). The aim of the extended calibration was to create a complete characterization of the sub-systems behaviour with respect to a large database of dust compositions that will be used for the analysis of the GIADA *in-flight* data acquired during the comet phase. The extended calibration activity was run using a wide set of cometary dust analogs selected after the knowledge acquired on cometary dust composition, thanks to the NASA/Stardust mission. Considering the asteroid-like mineralogy recorded in Comet Wild 2 samples (Zolensky et al., 2006; Brownlee et al., 2006; Rotundi et al., 2014) and the knowledge obtained by the analysis of Interplanetary Dust Particles (Rietmeijer, 2002), a list of natural mineral has been selected as cometary dust analogues of 67P/CG (Table 15).

| Class | Material | Structural Formula | Type |
|-----------------------------|---------------------------|---|----------------------|
| Nesosilicate | Forsterite | $Mg_{1.90}Fe_{0.10}Si_{1.00}O_4$ | crystals – amorphous |
| Nesosilicate | Fayalite | $Fe_{1.75}Mg_{0.13}Mn_{0.02}Si_{1.00}O_4$ | crystals – amorphous |
| Sorosilicate | Melilite | $Ca_{1.61}Na_{1.40}Al_{0.41}Mg_{0.51}Fe_{0.08}Si_{1.99}O_7$ | crystals |
| Inosilicate | Enstatite | $Mg_{1.80}Fe_{0.20}Si_{2.00}O_6$ | crystals – amorphous |
| Tectosilicate | Alkali-feldspar | $Na_{0.05}K_{1.04}Al_{10.5}Si_{2.95}O_8$ | crystals |
| Tectosilicate | Anorthite | $Ca_{0.97}Na_{0.08}Al_{1.88}Si_{2.10}O_8$ | crystals |
| Phyllosilicate | Serpentine | $Mg_{2.75}Fe_{0.15}Cr_{0.02}Al_{0.20}Si_{1.89}O_7$ | crystals – amorphous |
| Phyllosilicate | Talc | $Mg_{3.06}Si_{3.97}O_{11}$ | crystals – amorphous |
| Phyllosilicate | Kaolinite | $Al_{2.01}Si_{2.00}O_7$ | amorphous |
| Sulphide | Pyrrhotite | $Fe_{0.98}S$ | crystals |
| Oxide | Corundum | $Al_{2.00}O_3$ | amorphous |
| Ice-analog/coating material | Sodium Hexafluorosilicate | Na_2SiF_6 | crystals |
| Coating material | Amorphous carbon | — | amorphous |

Table 15: List of the terrestrial materials with the relative stoichiometric mineral composition (Ferrari et al., 2014) used as cometary dust analogues during the extended calibrations activity performed on the GIADA Proto-Flight Model (Della Corte et al., 2014).

The selected mineral analogues were prepared by grinding bulk mineral samples and sieving the powder to obtain samples selected in size taking into account the GIADA GDS and IS sub-systems

sensitivities. Four distinct size classes were obtained: $20 \mu\text{m} < \varnothing < 50 \mu\text{m}$, $50 \mu\text{m} < \varnothing < 100 \mu\text{m}$, $100 \mu\text{m} < \varnothing < 250 \mu\text{m}$ and $250 \mu\text{m} < \varnothing < 500 \mu\text{m}$. The minimum grain size detectable by GDS is not a fixed value, it depends on the optical properties of the specific material of the grain crossing the laser curtain. Pre-launch calibrations established a lower limit for grain diameter equal to $120 \mu\text{m}$ for carbon particles and $60 \mu\text{m}$ for silicate particles. One of the aims of the extended calibration phase was to better characterize the range of grain sizes detectable by GIADA exploring grain sizes down to $20 \mu\text{m}$ in diameter, i.e. smaller than the GDS expected detection limit.

The cometary dust analogues are divided into four families: i) particles without a coating material; ii) particles covered by amorphous carbon; iii) particles covered by the Na_2SiF_6 , used as water-ice analogue; iv) particle covered by both amorphous carbon and Na_2SiF_6 . Evaporating a solution of deionized water and Na_2SiF_6 on mineral dust particles produced the Na_2SiF_6 coating. Mineral grains were also sputtered with amorphous carbon: in an atmospheric controlled chamber a high energy Nd-YAG pulsed laser hits a carbon target vaporising it; a thin layer of amorphous carbon is consequently deposited on the mineral grains formerly placed on a substrate in the chamber. Cometary dust analogues were characterized by FE-SEM/EDS (Ferrari et al., 2014) and IR micro-spectroscopy prior to be used for GIADA calibration activity. Single grains were shot into the GIADA PFM with velocities ranging from 1 to 100 m/s, i.e. the expected velocities of the dust grains ejected from the cometary nucleus (Fink and Rubin, 2012; Fulle et al., 2010) (Figure 34).

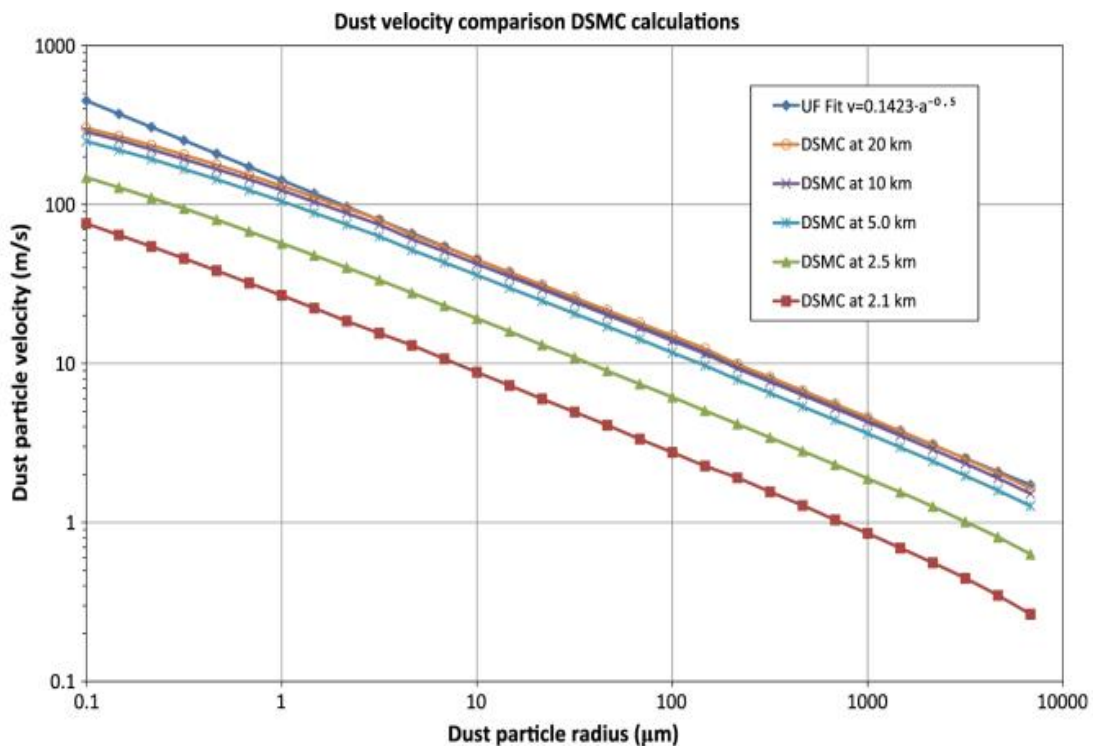


Figure 34: Results of DSMC calculations versus particle sizes for dust particle velocities at five distances from the nucleus centre (nucleus radius of 2 km). Dust particles decouple from the gas at about 10–20 km from the nucleus and reach the terminal velocity. For illustrative purposes is reported a simple fit to the velocity at 20 km from the nucleus

using the approximation $v \text{ (m/s)} = 0.1423a^{-0.5}$, a being the particle radius in m. This simple expression fits the dust velocity quite fine except for particles smaller than $1 \mu\text{m}$ (Fink and Rubin, 2012).

About one hundred of particles for each cometary analogue type were launched into the GIADA PFM in order to obtain a statistical meaningful number of measures necessary to evaluate the calibration curves of the sub systems.

In this chapter I will describe the calibration setup, the preparatory tests performed on the IS and GDS sub systems of the GIADA PFM, the calibration of the GDS using cometary dust analogues and the obtained results.

5.1 GIADA Calibration Setup

In order to reduce any possible instrument contamination the GIADA PFM, placed over an optical bench near to a Leica MC205 Optical Microscope, is hosted in a clean room class 100 in our laboratory where all the operations and activities, described in this chapter, have been performed.

The calibration activities on the GIADA PFM are performed on two GIADA sub-systems: the GDS and the IS. Taking into account the dimensions and the amount of the particles to be used for the calibration, we developed an innovative micromanipulation system able to capture, move and shoot particles with size in the range $20\div 500 \mu\text{m}$. The Electrostatic Micromanipulator (EM) is able to capture, manipulate and shoot these small particles by means of the electrostatic interaction between its probe and the particles themselves. The EM tool is mounted on a X-Y-Z micrometric slides assembly equipped with a 360° rotational stage and it is placed on an optical bench between the Leica MC205 microscope and the GIADA PFM (see Figure 35). This configuration allows a full control on the EM probe positioning and permits to characterize the dimension of the particle before capturing it. These measures are useful to correlate the signal detected by the GIADA sub-systems to the actual particle dimension.

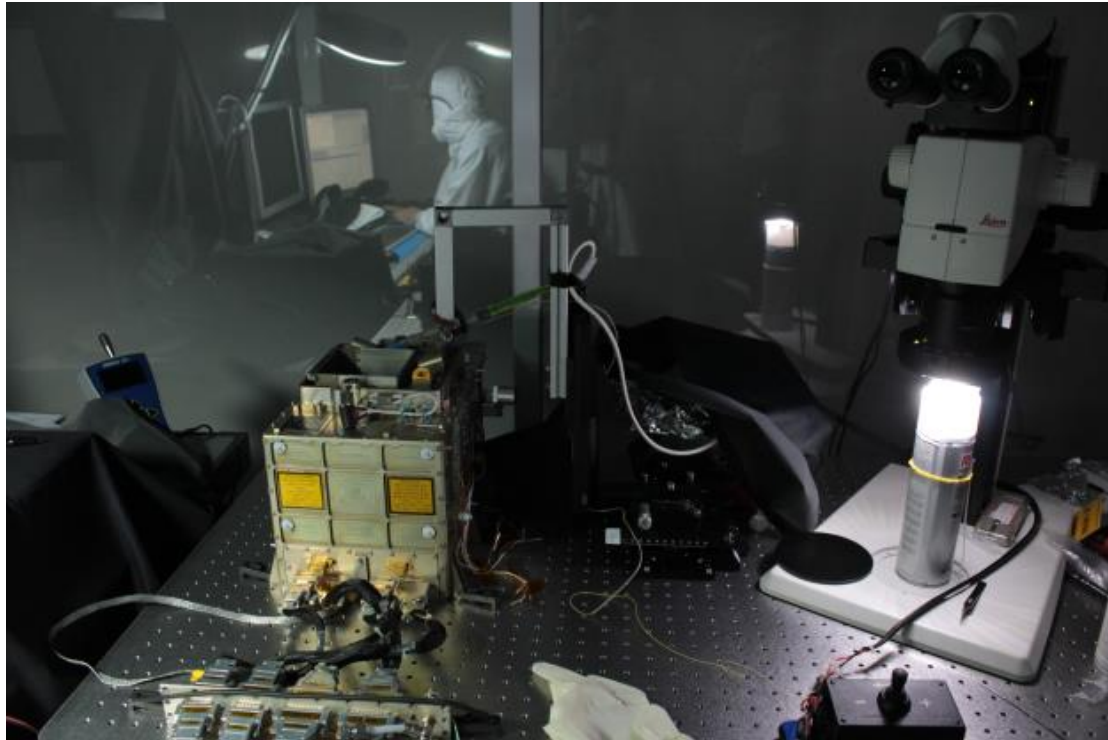


Figure 35: Set-up used for the GIADA PFM calibration. After having measured it under the microscope the grain is captured with the EM, moved over the GIADA baffle and shot.

This arrangement allowed defining the following calibration procedure:

- (1) Particles of a certain type and size, selected for GIADA calibration, are placed on a slide under the Leica MC205 Optical Microscope;
- (2) The particle to be shot into the GIADA PFM is selected and imaged at high resolution using the microscope equipped with a Leica IC80HD camera;
- (3) By means of the Leica Las V3.6 software the particle are is measured;
- (4) The particle is captured and shot inside the GIADA PFM;
- (5) The launch is considered valid if at least one of the two GDS receivers records a signal (GDS detection).

All the operation and the data acquisition of GIADA PFM are managed using the Electrical Ground Support Equipment (EGSE) software. The EGSE communicates with GIADA PFM by means of the Spacecraft Interface Simulator (SIS), i.e. the Rosetta spacecraft simulator.

5.1.1 The Electrostatic Micromanipulator

This device was developed with the aim to facilitate and speed up the calibration process on the GIADA PFM using cometary dust analogues. The device probe is composed by two adjacent thin glass needles, which are electrified producing a dipole (Figure 36). The distance between the two tips is 3.0 ± 0.1 mm (Figure 36). A silvered copper wire, with section of $250 \mu\text{m}$, is inserted into

each hollowed needle; to prevent the entering of dust grains into the needles, we sealed off the tips used to pick up the particles. Connecting one wire to the output of a High Voltage power Supply (HVS) and the other one to its reference (connected to the ground), an electric dipole is created between the two needles when the HVS is operating. Our laboratory tests showed that a short activation of power supply suffices to electrify the needles; in fact, once the probe is electrified, we need to switch off the HVS and then to approach the probe to the particle in order to pick it up.

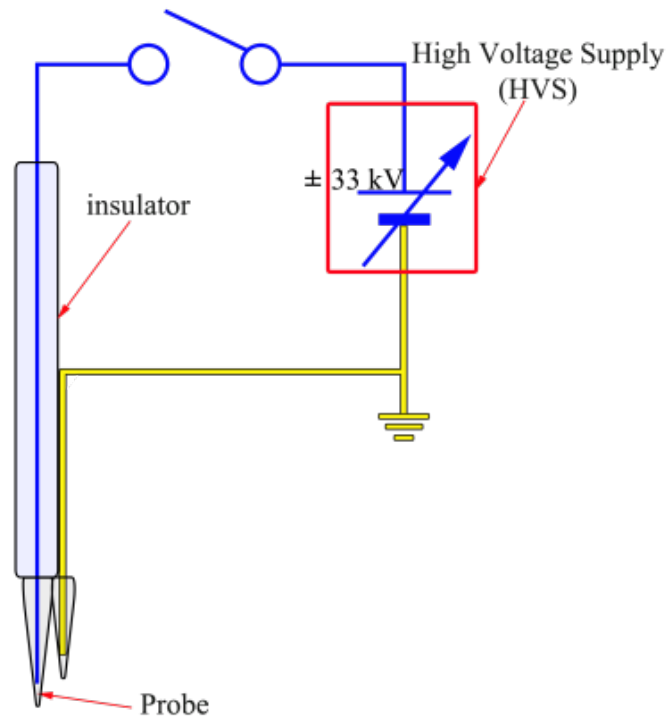


Figure 36: Electric scheme of the Electrostatic Micromanipulator (EM).

Because of the different intrinsic dielectric properties of the materials chosen, we used two different HVSs, one able to reach voltages between 0 and -33 kV and the other able to reach voltages between 0 and $+33$ kV. All the materials selected as cometary analogues, reported in Table 15, have been manipulated and launched using both positive and negative voltages.

5.1.2 Working Principle of the Electrostatic Micromanipulator

Switching on the HVS for few seconds, by means of a switch joystick, an electrostatic dipole is created between the two tips. Then, approaching the electrified probe to a particle ($\leq 500 \mu m$), the dielectrophoresis force is able to capture it. The dielectrophoresis force acting on a particle is given by:

$$F = \mathbf{n} \int_S \frac{1}{2} \epsilon_0 \epsilon_r (\mathbf{n} \cdot \mathbf{E})^2 dS \quad (5.1)$$

where ϵ_0 is the permittivity of free space, ϵ_r is the relative permittivity, S is the surface of the particle, \mathbf{n} is a unit normal vector of particle boundary and \mathbf{E} is the electrostatic field, whose magnitude can be determined by using the Poisson and the conservation of charge laws (Kawamoto, 2009). Once the particle is captured, we can shoot it simply by turn-on again the HVS with a voltage of the same sign used to capture the grain. In fact, when the particle lies on the tip of the electrified probe, the particle is charged with the same electric sign of HVS voltages used to electrify the tips. Therefore, once the HVS is reactivated, a repulsive Coulomb force is been created between the probe and the grain, and consequently the particle is shot.

The voltages and the polarity we used to electrify the needles and to pick up the particles depend on the material and size. The power supplies, ranging between 0 and ± 33 kV, have allowed the manipulation of the whole set of materials selected as cometary dust analogues.

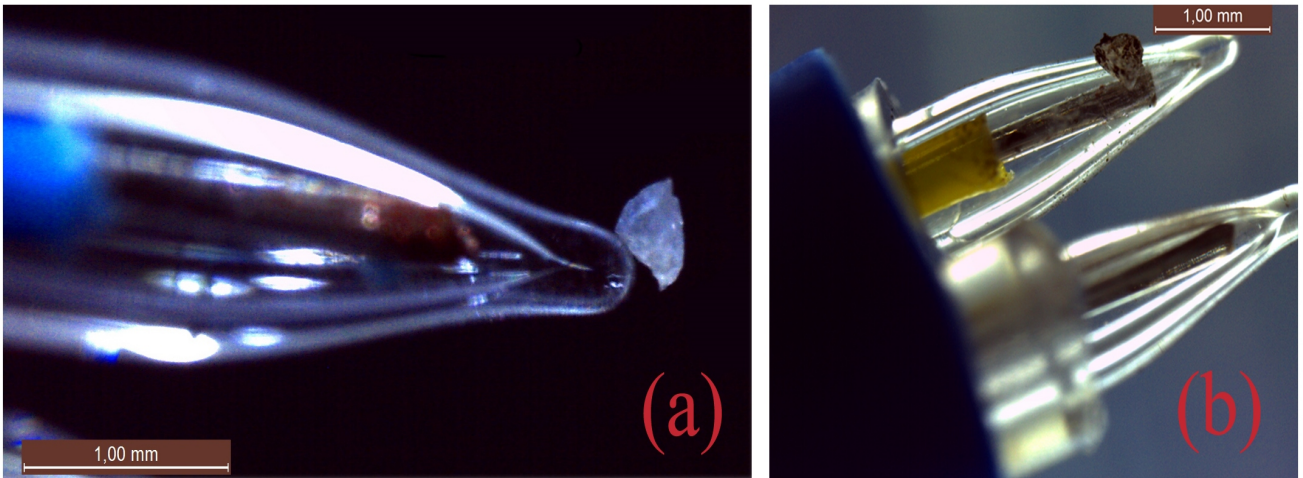


Figure 37: Two particles captured by the EM during our tests: a monomineralic grain of alkali-feldspar (a) and a grain of alkali-feldspar with amorphous carbon coating (b)

5.1.3 Electrostatic Micromanipulator Tests

Before using the electrostatic device for the extended calibration phase on the GIADA PFM, we performed some tests on the GIADA Structural/Thermal Model (STM) and on the IS-Development Model (DM), with the aim to verify its functionality and usability. In particular, we carried out two kinds of tests:

1. A series of tests on the GIADA STM, simulating the calibration on GIADA PFM. We

reproduced the setup to verify that the particles, shot by the EM, would have actually impacted the sensitive area of the IS. A graph paper, covered by an adhesive and transparent film, reproduces the IS surface and is able to stick the shot particles. A typical result of these tests is shown in Figure 38: considering twenty shot particles, only three impacted outside the sensitive surface. We verified that, in the worst case, the particles impacting outside the IS sensitive area, are 25% of the total shot grains.

2. A series of tests on the IS-DM (Figure 39 Left) have been conducted in order to check that the particles shot by the EM are actually detected. Figure 39 Right shows typical IS signals produced by a particle shot by the EM and impacting on the IS plate.

These preliminary laboratory tests have confirmed the proper functioning of the Electrostatic Micromanipulator.

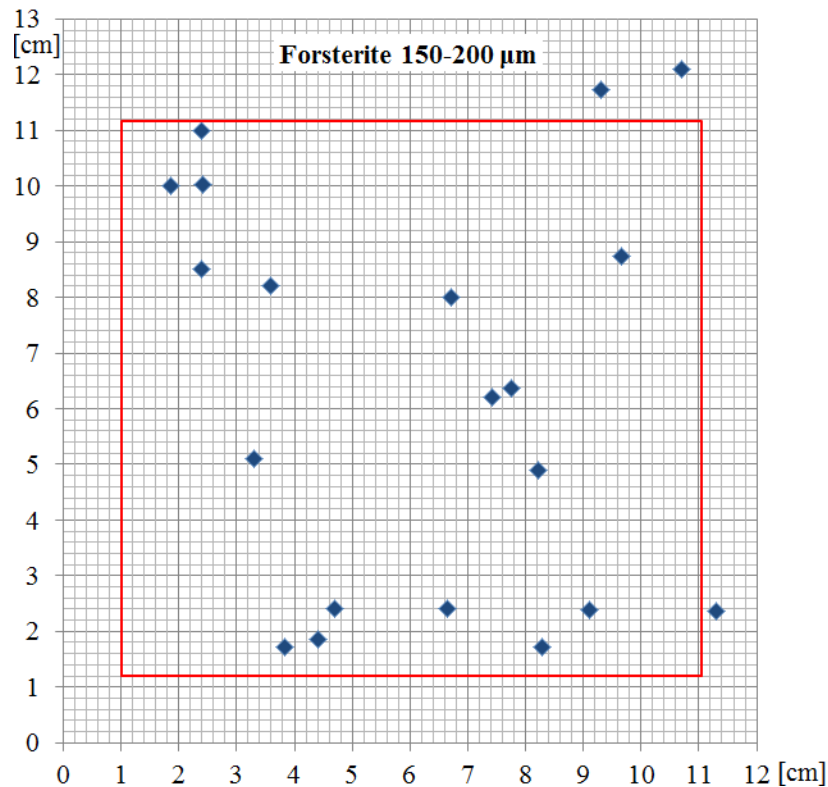


Figure 38: Impact positions of twenty Forsterite particles (blue points) in the size range 150-200 μm shot by the EM during a test on the GIADA STM. The red square represents the sensitive surface of the Impact Sensor.

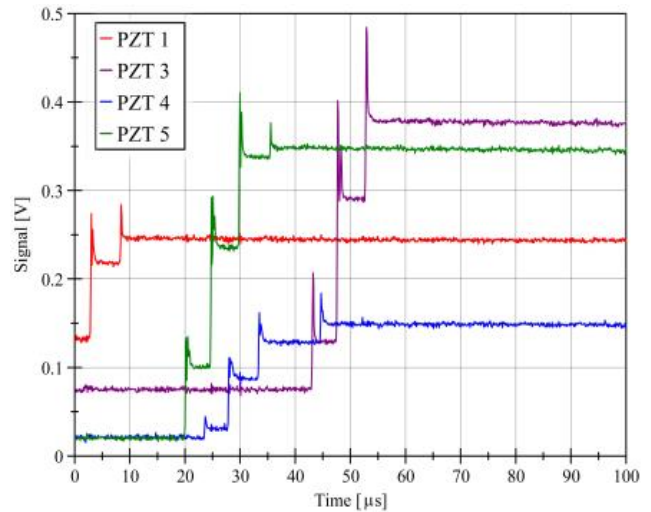
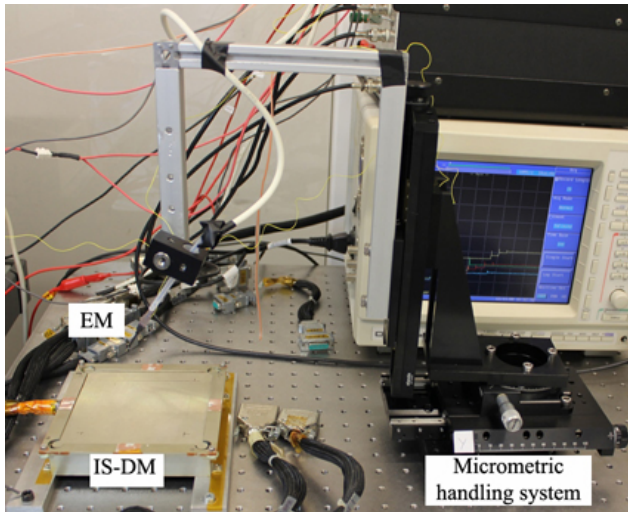


Figure 39: Left: the test performed using the Electrostatic Manipulator on the IS-DM in order to verify that the shot particles are detected by the sub-system. Right: Signals produced by IS sub-system as result of the impact of a forsterite grain particle (150-200 μm) shot by EM. The PZT2 signal is not acquired.

The first test performed using the EM to shoot particle into the GDS sensitive area showed that the velocity measured by the GDS are in the range $v_{\text{GDS}} = (1 \div 20) \text{ ms}^{-1}$. Considering the plots shown in Figure 34, we can notice that these velocities are coherent to those expected for cometary particles with diameter in the range 250-500 μm , but they are too low for smaller particles. In order to extend the velocity range used for the calibration activities, we decided to use a different shooting device to shoot particle with diameter $< 250\mu\text{m}$. This device is an air gun (Figure 40) already used during the GIADA pre-flight calibration (Mazzotta-Epifani, 2000).

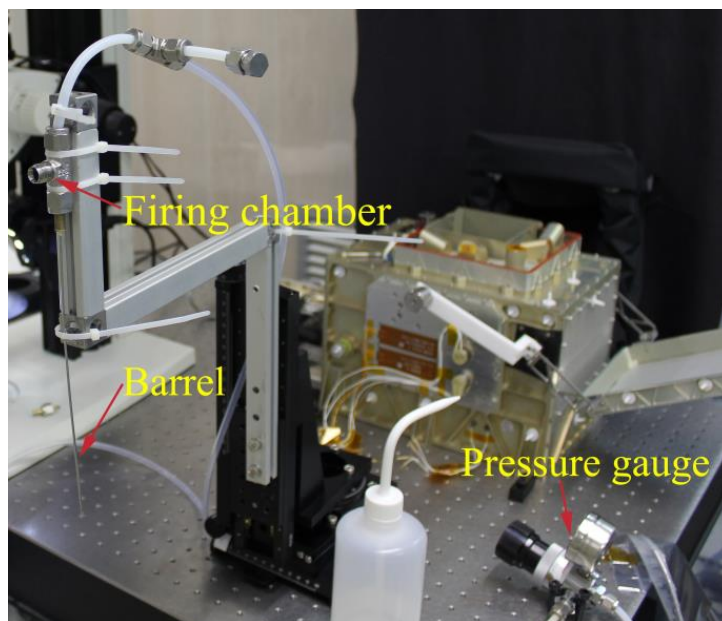


Figure 40: The compressed air gun used during the calibration activities to shoot particles smaller than 250 μm with velocities of $\approx (20 \div 100) \text{ ms}^{-1}$.

Each dust grain to be shot is picked up by a small metallic needle mounted on a cylindrical frame. After the capture, the needle with the stuck particle is connected to the firing chamber (Figure 40), exposing the dust grain to the airflow connected to the high pressure air circuit by mean of Teflon pipes. A pressure gauge allows setting the shooting pressure to values between 0 to 4bar. A dedicated valve, commanded by a button, activates the air flux that shoots the grain through a thin barrel into GIADA. Using this device we verified that the grain are shot with velocities $v_{GDS} = (20 \div 100) \text{ ms}^{-1}$.

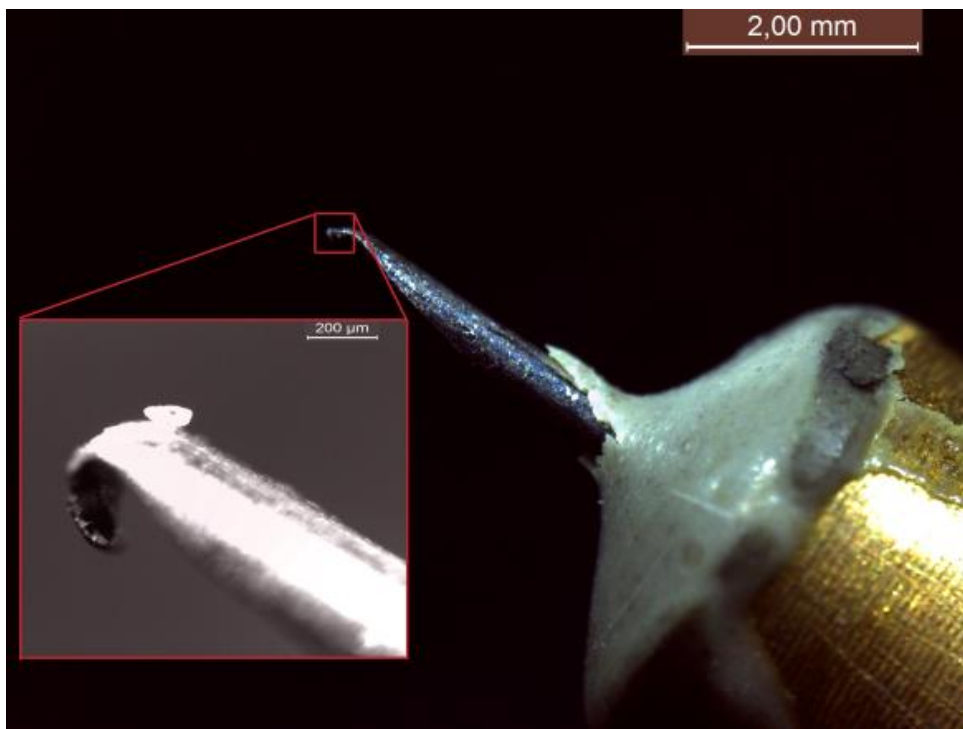


Figure 41: A picture of the metallic needle mounted on the cylindrical metallic frame of the compressed air gun, with the detail of a small alaki-feldspar particle captured.

5.2 Preparatory analyses on the IS and GDS

Before the starting the extended calibration activity using newly selected and prepared cometary dust analogues, an in depth study of the IS and GDS sub-systems responsivity was carried out. The responses as a function of a fixed stimulus of the IS and the GDS were studied. The analyses carried out resulting in two new empirical methods to reconstruct the impact position of a grain, for the IS, and the crossing position of the GDS laser curtain. These are key issues to scale the signal detected

by the two sub-systems using the sensitivity maps measured in 2002, during the pre-launch calibrations (Mazzotta-Epifani et al., 2002; Esposito et al., 2002).

5.2.1 Analyses on the IS sub-system

As explained in Chapter 2, both GIADA PFM (operating in our laboratory) and GIADA on board Rosetta, have an internal stimulator (PZT Calibrator, Figure 42) able to provide a pulse of known amplitude exciting the IS plate. This calibrator allows checking the IS responsivity and it is also used to study the behaviour of the GIADA *in-flight* IS during all the mission phases (see chapter 3). The data analysis performed on the IS, about the time delays recorded during all the Payload Checkouts (Figure 31), showed a stable behaviour. Nevertheless the recorded time delay, particularly for PZT2, resulted too short with respect to the geometrical configuration and the expected theoretical values.

The theoretical time delay values, as a consequence of a stimulus, can be obtained considering the exact position of the PZT Calibrator ($X=32$ mm, $Y=92$ mm in the reference frame shown in Figure 42), the position of the five PZT sensors under the IS plate (see Figure 42), and the wave propagation speed equal to 1711 ± 60 m/s (Esposito, 2001).

We recall that when a PZT detects the wave induced by a grain impact or, in this case by the PZT Calibrator (PZT_{Cal}), the ASP starts clocks to compute the propagation time of the flexural wave generated in the IS plate. These clocks are stopped when the other PZTs detect the event (the signal produced by the transducers is greater of a threshold set by a telecommand), and have a time resolution of $3\mu s$.

Due to the geometrical configuration (Figure 42), the first PZT detecting the wave produced by the PZT_{Cal} is always the PZT1. Therefore to evaluate the theoretical time delay, for each PZTs, we calculated the distance from the four PZTs and PZT1. In Table 16 the relative distances from the PZT1 and each other PZT and the relative theoretical time delay obtained are reported.

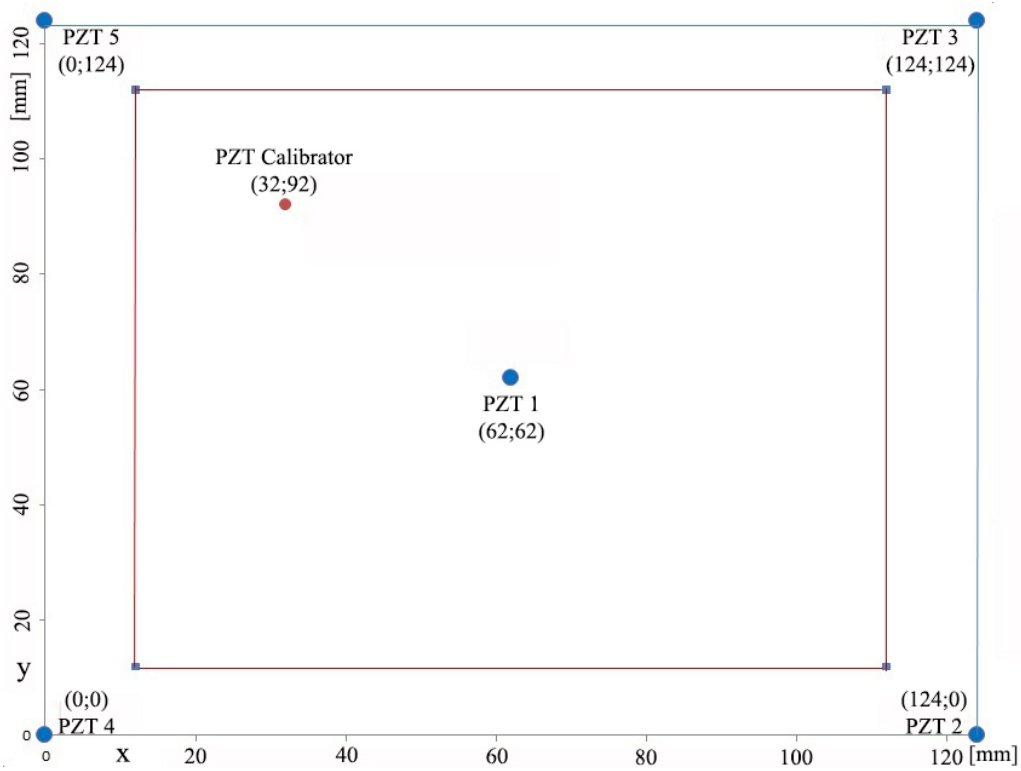


Figure 42: The Impact Sensor with the arrangement of the five piezoelectric sensors (PZTs).

| <i>Distance between PZT_{cal} and each PZTs</i> | | | | |
|--|--------------------------------|--------------------------------|--------------------------------|--------------------------------|
| r_1 (mm) | r_2 (mm) | r_3 (mm) | r_4 (mm) | r_5 (mm) |
| 42,4 | 130,1 | 97,4 | 97,4 | 45,3 |
| Δr_1 (mm) | Δr_2 (mm) | Δr_3 (mm) | Δr_4 (mm) | Δr_5 (mm) |
| 0,0 | 87,7 | 55,0 | 55,0 | 2,8 |
| <i>Theoretical delays evaluated considering the wave propagation speed $v = 1.711\text{mm}/\mu\text{s}$</i> | | | | |
| Δt_1 (μs) | Δt_2 (μs) | Δt_3 (μs) | Δt_4 (μs) | Δt_5 (μs) |
| 0 | 51 (48, 54)* | 30 (27, 33)* | 30 (27, 33)* | 0 (3)* |

Table 16: r_x is the relative distances between the PZT_{cal} and the different sensors. Δr_x is the difference between these distance (r_x) and the constant value r_1 , which represents the distance between the calibrator and the closer PZT sensor. The theoretical time delays, Δt_x , are calculated considering the wave propagation speed estimated in Esposito (2001). These values are normalized considering that the IS Proximity Electronics has a time step of 3 μs . * The values in the parentheses are the possible time delays taking into account the incertitude and the time step.

The time delay measured during the whole Cruise Phase for the five PZTs are summarized in Table 17.

| $\Delta t_1 (\mu s)$ | $\Delta t_2 (\mu s)$ | $\Delta t_3 (\mu s)$ | $\Delta t_4 (\mu s)$ | $\Delta t_5 (\mu s)$ |
|----------------------|----------------------|----------------------|----------------------|----------------------|
| 0 | 15 | 24 | 30 | 6 |

Table 17: Time Delays measured during the whole Cruise Phase, as a consequence of PZT_{cal} stimuli of 10V.

We performed a series of test devoted to investigate this aspect using the GIADA PFM and stimulating with the internal calibrator the IS sensitive surface with stimuli of different amplitude. The thresholds configuration used for these tests is identical to those used on the GIADA *in-flight*. As reported in Table 18, the delays recorded by the five PZT sensors, as on the GIADA *in-flight*, are quite different with respect to the theoretical ones, particularly for PZT2.

| PZT_{cal.} = 5V stimuli | | | | | |
|---|----------------------|----------------------|----------------------|----------------------|----------------------|
| | $\Delta t_1 (\mu s)$ | $\Delta t_2 (\mu s)$ | $\Delta t_3 (\mu s)$ | $\Delta t_4 (\mu s)$ | $\Delta t_5 (\mu s)$ |
| Mode | 0 | 27 | 33 | 33 | 9 |
| Mean values & standard deviations | 0 | 26,1 ± 1,4 | 33,0 ± 0,0 | 33,0 ± 0,0 | 9,5 ± 1,1 |
| Discrepancies with theoretical results | 0 | 24 | 3 | 3 | 9 |
| PZT_{cal.} = 8V stimuli | | | | | |
| | $\Delta t_1 (\mu s)$ | $\Delta t_2 (\mu s)$ | $\Delta t_3 (\mu s)$ | $\Delta t_4 (\mu s)$ | $\Delta t_5 (\mu s)$ |
| Mode | 0 | 21 | 33 | 30 | 6 |
| Mean values & standard deviations | 0 | 21,0 ± 1,9 | 33,1 ± 1,8 | 28,9 ± 2,5 | 5,0 ± 2,4 |
| Discrepancies with theoretical results | 0 | 30 | 3 | 0 | 6 |
| PZT_{cal.} = 10V stimuli | | | | | |
| | $\Delta t_1 (\mu s)$ | $\Delta t_2 (\mu s)$ | $\Delta t_3 (\mu s)$ | $\Delta t_4 (\mu s)$ | $\Delta t_5 (\mu s)$ |
| Mode | 0 | 21 | 33 | 33 | 9 |
| Mean values & standard deviations | 0 | 19,7 ± 4,1 | 34,5 ± 2,1 | 32,8 ± 0,8 | 8,8 ± 0,8 |
| Discrepancies with theoretical results | 0 | 30 | 3 | 3 | 9 |

Table 18: The time delays recorded by each PZT generated by the PZT_{cal} stimuli of different amplitude: 5V, 8V and 10V.

In order to investigate the origin of the discrepancies between the theoretical and experimental time delays, we studied the time delays versus PZT thresholds behaviour. All these tests were performed fixing the PZT_{cal} stimulus at 10 V. This is the stimulus amplitude used for the GIADA *in-flight* self-

calibrations during the whole Cruise Phase. The results of these tests are reported in Table 19. In particular, we notice that for PZT2 the discrepancies between the theoretical and experimental time delays decrease increasing the value of the thresholds. All the tests performed show that the PZT2 records time delays shorter than those expected.

| <i>Thresholds: PZT 1 = 80 mV; PZT 2 = 200 mV; PZT 3 = 200 mV; PZT 4 = 40 mV; PZT 5 = 80 mV</i> | | | | | |
|---|-----------------------------|-----------------------------|-----------------------------|-----------------------------|-----------------------------|
| | Δt_1 [μs] | Δt_2 [μs] | Δt_3 [μs] | Δt_4 [μs] | Δt_5 [μs] |
| Mode | 0 | 30 | 33 | 33 | 3 |
| Discrepancy with theoretical results | 0 | 21 | 3 | 3 | 3 |
| <i>Thresholds: PZT 1 = 80 mV; PZT 2 = 220 mV; PZT 3 = 220 mV; PZT 4 = 40 mV; PZT 5 = 80 mV</i> | | | | | |
| | Δt_1 [μs] | Δt_2 [μs] | Δt_3 [μs] | Δt_4 [μs] | Δt_5 [μs] |
| Mode | 0 | 30 | 33 | 33 | 3 |
| Discrepancy with theoretical results | 0 | 21 | 3 | 3 | 3 |
| <i>Thresholds: PZT 1 = 80 mV; PZT 2 = 280 mV; PZT 3 = 260 mV; PZT 4 = 50 mV; PZT 5 = 100 mV</i> | | | | | |
| | Δt_1 [μs] | Δt_2 [μs] | Δt_3 [μs] | Δt_4 [μs] | Δt_5 [μs] |
| Mode | 0 | 36 | 33 | 33 | 3 |
| Discrepancy with theoretical results | 0 | 25 | 3 | 3 | 3 |
| <i>Thresholds: PZT 1 = 80 mV; PZT 2 = 360 mV; PZT 3 = 260 mV; PZT 4 = 50 mV; PZT 5 = 150 mV</i> | | | | | |
| | Δt_1 [μs] | Δt_2 [μs] | Δt_3 [μs] | Δt_4 [μs] | Δt_5 [μs] |
| Mode | 0 | 42 | 33 | 33 | 3 |
| Discrepancy with theoretical results | 0 | 9 | 3 | 3 | 3 |

Table 19: Mode of the time delays recorded by PZT sensors varying their thresholds. In particular we can notice how the discrepancies between the theoretical and experimental time delays of PZT2 decrease increasing the thresholds.

The PZT2 behaviour was deeply studied by mean of a series of tests performed applying different threshold values and stimulating the IS plate with the PZT_{Cal} set at different amplitudes. In Figure 43 and in Table 20 the obtained results are reported.

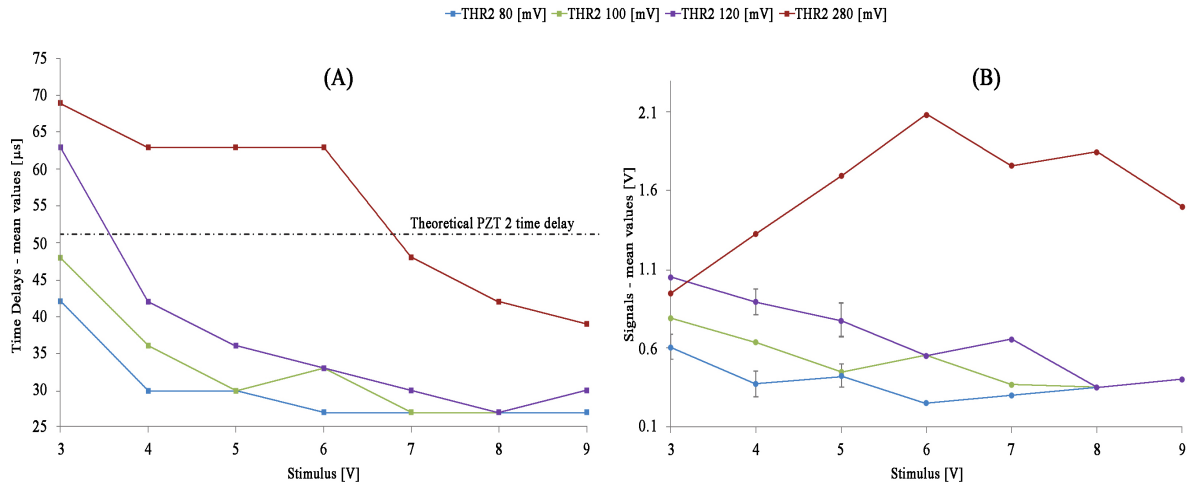


Figure 43: Time delays (A) and signals (B) recorded by the PZT2 sensor vs PZT_{Cal} stimulus, at different thresholds.

| Stimulus [V] | THR 2 = 80 mV | THR 2 = 100 mV | THR 2 = 120 mV | THR 2 = 280 mV |
|--------------|-------------------------|-------------------------|-------------------------|-------------------------|
| | <i>Time Delays [μs]</i> | <i>Time Delays [μs]</i> | <i>Time Delays [μs]</i> | <i>Time Delays [μs]</i> |
| 3 | 42 | 48 | 63 | 69 |
| 4 | 30 | 36 | 42 | 63 |
| 5 | 30 | 30 | 36 | 63 |
| 6 | 27 | 33 | 33 | 63 |
| 7 | 27 | 27 | 30 | 48 (42) |
| 8 | 27 | 27 | 27 | 42 |
| 9 | 27 | 30 | 30 | 39 |

Table 20: Time delays recorded by the PZT2 sensor during the test using the internal calibrator with stimuli of different amplitude. The values for different thresholds are reported. The theoretical delay of the PZT2 sensor is $(51 \pm 3) \mu s$.

Observing Figure 43 we notice that the signal recorded by PZT2 (panel B), with the threshold sets to values lower than 280 mV, decreases with the PZT_{Cal} stimulus increasing. Instead, for threshold set to 280 mV the signal raises up linearly until a 6 V stimulus, then reverses its trend, starting to decrease. The signal detected for each amplitude stimulus resulted too low with respect to those detected by the other PZTs. The panel A of Figure 9 and Table 20 stress as the time delay recorded, with low threshold values, always result too short respect to the theoretical one. With high threshold value and for stimuli of 7V we can obtained a time delay close to the theoretical one.

All these considerations led us to conclude that PZT2 is affected by cross-talk, i.e. a signal detected by another channel that creates an undesired effect on the PZT2 channel.

So, in order to obtain acceptable time delays with respect to the theoretical ones and thus reducing the cross-talk effects, a possible solution is to set the PZT2 threshold to high values, 280mV during all tests (Figure 43, Table 20). In this way, PZT2 will be the last PZT sensor to detect the stimulus,

as expected by the geometrical configuration. Unfortunately a high threshold prevent the detection of low signals. Taking into account all these issues we decided to set the PZT2 threshold to 80mV, but for the impact position definition, as explained in the following, we used the delays recorded by PZT2 only when their values are equal to zero (impact position near the PZT2).

As reported in Esposito (2000), the response of the five PZTs sensors is not uniform upon the aluminium plate, because of the dissipative forces during the wave propagation. So, for a given stimulus, the response of each sensor depends on the impact position. The map of the IS response to a fixed momentum was realized during the pre-flight calibrations, when the IS aluminium plate was stimulated with a constant impulse over a grid of 90 x 90 points (Esposito, 2000).

For a correct data analysis is therefore necessary to take into account the non-uniformity of the IS plate. For this reason, first of all it is pivotal to determine the coordinates of the point where the particle impacted. As reported by Esposito (2000), an analytical method to reconstruct the impact position from three of the five time delays recorded by GIADA was used:

$$p^* = \begin{cases} x_{stim} = A + r_0 B \\ y_{stim} = C + r_0 D \end{cases} \quad (5.2)$$

where

$$r_0 = \frac{-(2AB+2CD-E) \pm \sqrt{(2AB+2CD-E)^2 - 4(B^2+D^2-1)(A^2+C^2-F)}}{2(B^2+D^2-1)} \quad (5.3)$$

and A, B, C, D, E and F are coefficients that depend on the configuration used to calculate the impact positions. The best configuration to determine univocally the impact position on the aluminium plate (Figure 44) is the one that considers three PZT sensors arranged along three corners (Esposito, 2000). For these configurations the coefficients A, B, C, D, E and F are reported in Table 21. In principle, using this analytical method we could obtain four identical solutions within the error incertitude.

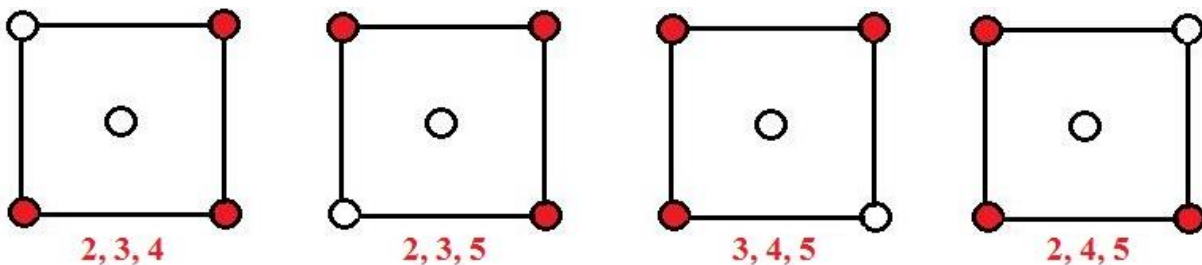


Figure 44 The four best configurations of the PZT sensors for the determination of the impact position.

| | | | | |
|--|-----------|-----------|-----------|-----------|
| | PZT 2,3,4 | PZT 2,3,5 | PZT 3,4,5 | PZT 2,4,5 |
|--|-----------|-----------|-----------|-----------|

| | | | | |
|---|--|--|--|--|
| A | $a + \frac{\Delta r_2^2 - \Delta r_3^2}{4a}$ | $a + \frac{\Delta r_5^2 - \Delta r_4^2}{4a}$ | $a + \frac{\Delta r_5^2 - \Delta r_4^2}{4a}$ | $a + \frac{\Delta r_2^2 - \Delta r_3^2}{4a}$ |
| B | $\frac{\Delta r_2 - \Delta r_3}{2a}$ | $\frac{\Delta r_5 - \Delta r_4}{2a}$ | $\frac{\Delta r_5 - \Delta r_4}{2a}$ | $\frac{\Delta r_2 - \Delta r_3}{2a}$ |
| C | $a + \frac{\Delta r_3^2 - \Delta r_4^2}{4a}$ | $a + \frac{\Delta r_3^2 - \Delta r_4^2}{4a}$ | $a + \frac{\Delta r_2^2 - \Delta r_5^2}{4a}$ | $a + \frac{\Delta r_2^2 - \Delta r_5^2}{4a}$ |
| D | $\frac{\Delta r_3 - \Delta r_4}{2a}$ | $\frac{\Delta r_3 - \Delta r_4}{2a}$ | $\frac{\Delta r_2 - \Delta r_5}{2a}$ | $\frac{\Delta r_2 - \Delta r_5}{2a}$ |
| E | $2\Delta r_2$ | $2(\Delta r_3 + \Delta r_5 - \Delta r_4)$ | $2\Delta r_2$ | $2\Delta r_2$ |
| F | Δr_2^2 | $\Delta r_3^2 + \Delta r_5^2 - \Delta r_4^2$ | Δr_2^2 | Δr_2^2 |

Table 21: Values of the coefficients present in the relations (4.8) and (4.9) when the three sensors are used in the calculation of the impact position are respectively arranged in configurations.

5.2.2 The Time Delays Map

In order to test the analytical method ability to reconstruct the particle impact position, we performed a dedicated test on the GIADA PFM IS sub-system. We identified a matrix of 10x9 points with a 10 mm steps, starting in the position (X=17 mm, Y=17 mm) with respect to the reference system reported in Figure 45, to test the IS with a repeatable solicitation. We dropped at least 10 glass spherical particles with diameters of 500µm on each position. Being the test exclusively dedicated to impact position reconstruction we used only glass spheres and not cometary dust analogues in order to reduce the uncertainty due to the shape of the impacting grain.

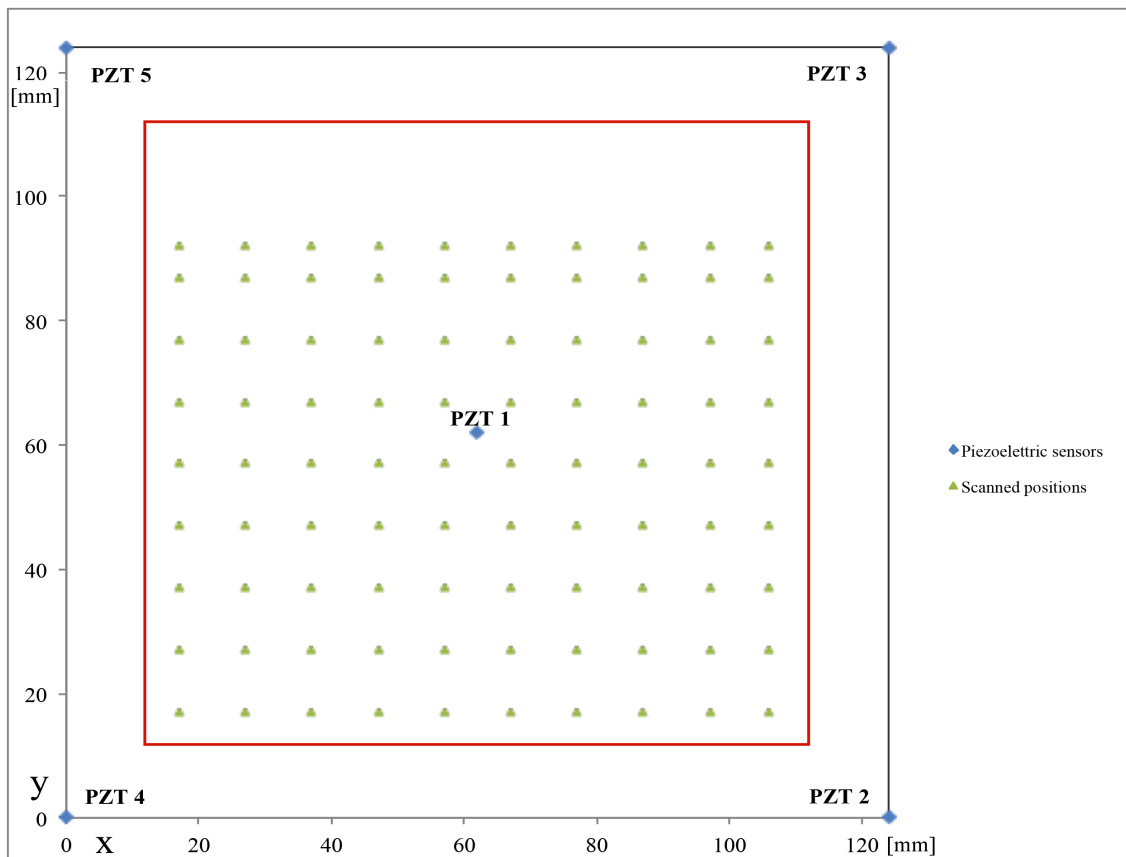


Figure 45: The positions (green triangles) on the IS plate where we dropped the glass spheres to study the IS response.

In Figure 46 it is shown the setup used to build-up the IS time delays map. A plastic straw, 13 cm long with an internal diameter of 1 mm, is fixed to the manual-handling tool used for the EM. At the top of the straw, a small funnel facilitates the insertion of the glass sphere that will then fall down to impact the aluminium plate. During the spheres dropping the lower part of the straw is kept steadily at 1-2 mm over the aluminium plate. The impact position is known with a good accuracy maintaining the height from which the sphere fall and the related impulse constant. Due to the particle geometry, dimension and material used to stimulate the aluminium plate, when the sphere impact the IS plate GIADA electronic records several “events” generated by particle multiple bounces. Actually, in our analysis we considered only the time delays related to the first event, because they are related to the first interaction between the particle and the IS plate.

We collected, for each analysed position and each PZT sensor, ten values of time delays due to the impinging particles and we evaluated the mode values (Figure 47).

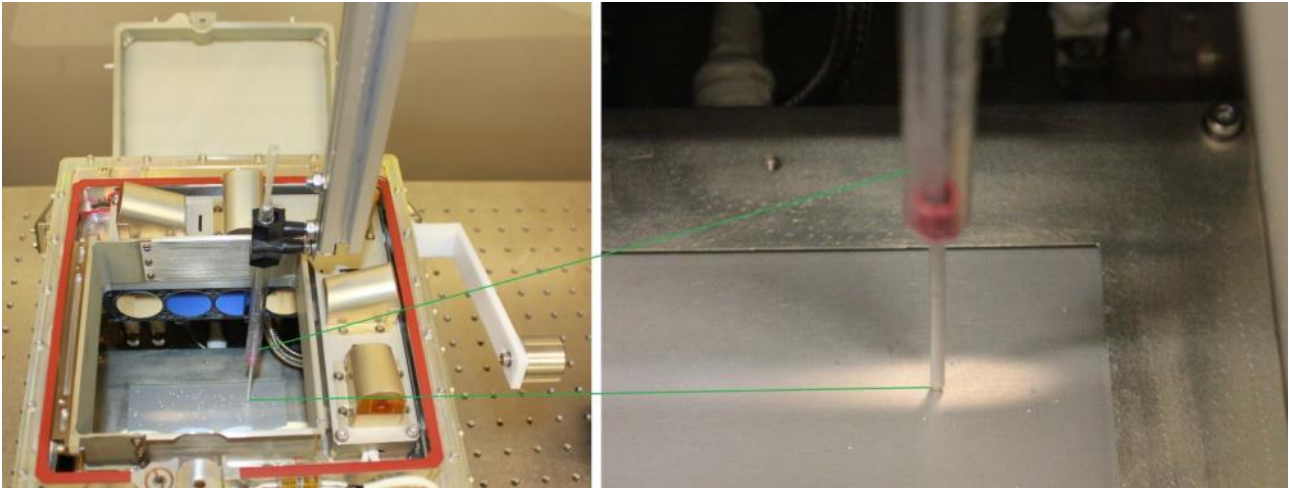


Figure 46: The device used for the IS calibration. A plastic straw fixed to a manual micromanipulator at a certain distance from the IS plate is used to drop glass spheres ($\varnothing = 500 \mu\text{m}$) on the sensitive surface.

| | PZT1PART | PZT1AMPL [v] | PZT1TIME [μs] | PZT2PART | PZT2AMPL [v] | PZT2TIME [μs] | PZT3PART | PZT3AMPL [v] | PZT3TIME [μs] | PZT4PART | PZT4AMPL [v] | PZT4TIME [μs] | PZT5PART | PZT5AMPL [v] | PZT5TIME [μs] |
|------|----------|--------------|---------------|----------|--------------|---------------|----------|--------------|---------------|----------|--------------|---------------|----------|--------------|---------------|
| 1 | Detected | 9.4375 | 0 | Detected | 9.5187 | 0 | Detected | 5.1542 | 12 | Detected | 8.0832 | 12 | Detected | 6.7173 | 36 |
| 2 | Detected | 9.4317 | 0 | Detected | 9.51 | 0 | Detected | 5.711 | 12 | Detected | 8.2688 | 15 | Detected | 6.4621 | 36 |
| 3 | Detected | 8.0252 | 0 | Detected | 9.742 | 0 | Detected | 7.886 | 21 | Detected | 3.3446 | 18 | Detected | 4.8758 | 45 |
| 4 | Detected | 9.8058 | 0 | Detected | 9.6811 | 0 | Detected | 8.756 | 21 | Detected | 4.2668 | 15 | Detected | 4.9744 | 39 |
| 5 | Detected | 9.4114 | 0 | Detected | 9.4839 | 0 | Detected | 8.3761 | 18 | Detected | 8.4602 | 18 | Detected | 6.291 | 36 |
| 6 | Detected | 5.6675 | 0 | Detected | 9.8116 | 3 | Detected | 7.9237 | 24 | Detected | 2.4485 | 18 | Detected | 3.4345 | 48 |
| 7 | Detected | 9.7594 | 0 | Detected | 9.6579 | 0 | Detected | 9.0547 | 21 | Detected | 4.7018 | 15 | Detected | 5.5283 | 39 |
| 8 | Detected | 9.568 | 0 | Detected | 9.597 | 0 | Detected | 7.2915 | 18 | Detected | 6.0271 | 15 | Detected | 6.7985 | 39 |
| 9 | Detected | 5.9198 | 0 | Detected | 9.8145 | 3 | Detected | 6.1141 | 21 | Detected | 2.5906 | 21 | Detected | 3.2808 | 48 |
| 10 | Detected | 9.51 | 0 | Detected | 9.5767 | 0 | Detected | 7.9382 | 18 | Detected | 6.8043 | 18 | Detected | 5.0556 | 36 |
| Mean | | 8.654 | 0 | Mean | 9.639 | 0.6 | Mean | 7.421 | 18.6 | Mean | 5.500 | 16.5 | Mean | 5.342 | 40.2 |
| STD | | 1.507 | 0 | STD | 0.116 | 1.2 | STD | 1.260 | 3.7 | STD | 2.228 | 2.4 | STD | 1.205 | 4.7 |
| MODE | | 0 | 0 | MODE | 0 | 0 | MODE | 21 | 21 | MODE | 15 | 15 | MODE | 36 | 36 |

Figure 47: The Excel sheet shows an example of the data collected for the IS calibration by the GIADA PFM electronic. We register ten “useful” events for each fixed position, in this example the position being (77 mm, 17 mm). For each PZT sensor, we determine the mode of the recorded delays.

The obtained dataset links the time delays measured by each PZTs to defined positions (X,Y). We applied the analytical method (Esposito, 2000) to reconstruct the impact positions, verifying that the values obtained with this method have an error in positioning reconstruction greater than 5 cm. The failure of the analytical method in reconstructing the impact position with a required accuracy led us to develop a new empirical method that finally does reconstruct the impact position with much higher precision and much shorter elaboration time with respect to the method developed by Esposito (2000). The new method has been implemented developing a specific tool (Lucarelli, 2013) that couples the impact position with the actual delays measured during the GIADA calibration campaign performed in 2002. In order to test the new method we performed an

additional scan on the IS area. The experimental configuration and the setup was the same as the one already used for the previous test described above, the only difference introduced are the number of scanned positions, i.e. 25, and the selected step between two adjacent points, i.e. 25 mm (Figure 48). The results of the additional test are synthesized in Table 22, where the real impact positions, the positions derived by the analytical method and those obtained with the new empirical method are reported.

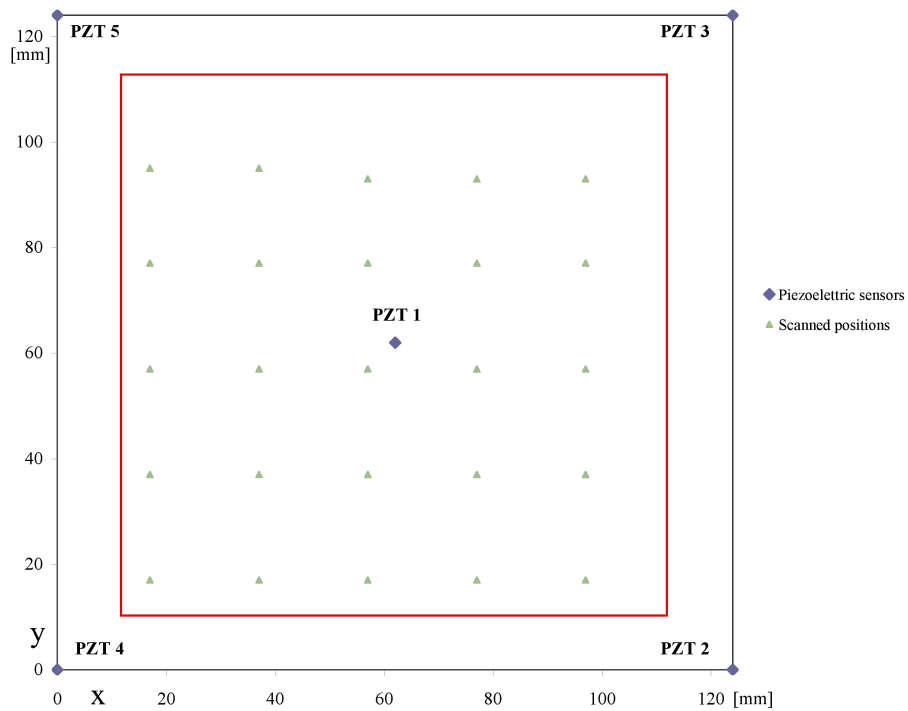


Figure 48: The positions (green rhombus) on the IS plate where we dropped the glass spheres to study the IS response and to verify the capability in reconstructing the impact positions of the newly developed empirical method.

| Real Impact Positions | | ANALYTICAL METHOD ($v=1,711 \text{ mm}/\mu\text{s}$) | | | | | | | | New Method | |
|-----------------------|--------|--|--------|---------------|--------|---------------|--------|---------------|--------|------------|--------|
| | | Comb: 2, 3, 5 | | Comb: 2, 3, 4 | | Comb: 3, 4, 5 | | Comb: 2, 4, 5 | | | |
| X [mm] | Y [mm] | X [mm] | Y [mm] | X [mm] | Y [mm] | X [mm] | Y [mm] | X [mm] | Y [mm] | X [mm] | Y [mm] |
| 17 | 17 | 55,7 | 44,6 | 51,6 | 108,6 | 104,6 | 91,9 | 137,8 | 30,1 | 18,9 | 24,5 |
| 17 | 37 | 58,7 | 51,4 | 57,5 | 89,0 | 90,4 | 82,6 | 100,5 | 47,3 | 17,2 | 39,0 |
| 17 | 57 | 62,0 | 62,0 | 62,0 | 72,9 | 72,1 | 72,1 | 72,9 | 62,0 | 19,6 | 54,9 |
| 17 | 77 | 66,4 | 84,9 | 65,6 | 62,0 | 43,7 | 62,0 | 46,3 | 81,4 | 45,6 | 106,0 |
| 17 | 95 | 71,4 | 94,4 | 69,1 | 58,6 | 35,0 | 57,5 | 40,8 | 87,0 | 34,7 | 105,9 |
| 37 | 17 | 55,3 | 51,6 | 52,3 | 98,9 | 92,4 | 88,4 | 105,5 | 46,7 | 18,5 | 36,3 |
| 37 | 37 | 65,4 | 54,5 | 66,2 | 79,7 | 88,4 | 76,9 | 94,4 | 52,6 | 30,7 | 38,1 |
| 37 | 57 | 54,9 | 58,6 | 54,0 | 73,7 | 68,7 | 72,4 | 69,5 | 58,1 | 33,9 | 56,6 |
| 37 | 77 | 62,0 | 72,9 | 62,0 | 58,4 | 46,9 | 57,9 | 48,5 | 71,8 | 49,9 | 92,4 |
| 37 | 95 | 57,8 | 79,7 | 58,0 | 73,3 | 52,1 | 73,8 | 52,5 | 79,0 | 42,3 | 109,9 |
| 57 | 17 | 52,2 | 48,5 | 50,3 | 70,0 | 72,4 | 68,7 | 74,5 | 45,8 | 23,6 | 54,5 |
| 57 | 37 | 55,8 | 41,0 | 54,0 | 73,7 | 86,1 | 71,0 | 94,8 | 33,2 | 45,4 | 37,1 |
| 57 | 57 | 59,0 | 36,7 | 58,3 | 65,7 | 87,3 | 65,0 | 96,2 | 27,8 | 52,7 | 36,0 |
| 57 | 77 | 58,7 | 51,4 | 58,4 | 62,0 | 69,3 | 62,0 | 70,0 | 50,3 | 28,1 | 92,2 |
| 57 | 93 | 78,7 | 78,7 | 75,1 | 48,9 | 45,3 | 45,3 | 48,9 | 75,1 | 57,7 | 96,2 |
| 77 | 17 | 42,3 | 26,4 | 36,0 | 62,0 | 76,6 | 62,0 | 83,6 | 10,8 | 102,8 | 42,9 |
| 77 | 37 | 39,7 | 43,5 | 31,7 | 80,6 | 71,8 | 75,5 | 75,3 | 37,3 | 35,4 | 52,4 |
| 77 | 57 | 62,0 | 28,0 | 62,0 | 51,1 | 85,9 | 52,9 | 93,2 | 18,0 | 93,3 | 64,3 |
| 77 | 77 | 79,1 | 53,7 | 78,5 | 49,2 | 74,2 | 48,8 | 73,7 | 54,0 | 78,7 | 91,4 |
| 77 | 93 | 79,7 | 57,8 | 77,3 | 39,1 | 57,5 | 35,0 | 58,3 | 58,5 | 73,3 | 101,1 |
| 97 | 17 | 31,1 | 4,2 | 12,7 | 67,3 | 87,3 | 65,0 | 129,1 | -89,4 | 105,3 | 29,5 |
| 97 | 37 | 40,3 | 19,9 | 32,1 | 62,0 | 80,3 | 62,0 | 92,3 | -5,7 | 100,8 | 39,4 |
| 97 | 57 | 56,3 | 29,7 | 55,2 | 54,3 | 81,3 | 55,8 | 87,5 | 20,0 | 79,3 | 86,5 |
| 97 | 77 | 75,2 | 49,8 | 74,8 | 45,5 | 70,3 | 44,9 | 70,0 | 50,3 | 77,0 | 99,4 |
| 97 | 93 | 85,3 | 48,8 | 82,6 | 33,6 | 66,7 | 29,4 | 66,0 | 50,7 | 83,6 | 106,6 |

Table 22: The impact positions derived by means of the analytical method (Esposito, 2002) and those obtained with the new method elaborated. The real impact positions are reported in the first two columns on the left.

Figure 49 shows that the new method identifies 68% of the real impact positions, within an error of 2.5 cm, thus an important improvement compared to the 24% of impact position reconstructed, within the same error of 2.5 cm, with the analytical method.

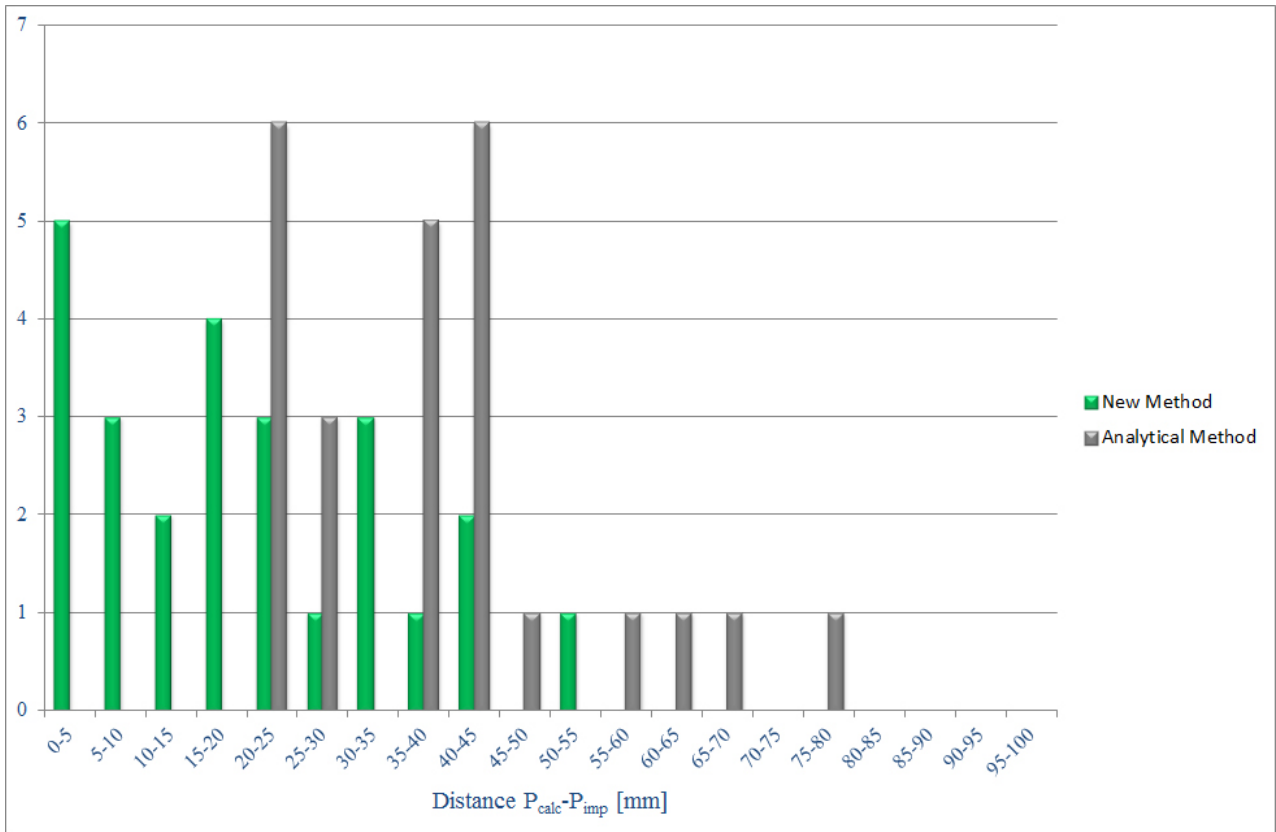


Figure 49: Histogram of the distances between the real and the calculated impact positions derived by using alternatively the analytical method (grey area) and the new developed method (green area). impact.

Taking into account the good results obtained on the data collected during the activities performed on the GIADA PFM Impact Sensor in laboratory, we decided to implement this method also for the analysis of the data that we come from GIADA *in-flight*. The newly developed method will correctly define the cometary grains impact positions and will allow us to apply the right sensitivity map correction coefficient to the detected signal.

5.2.3 Preparatory activity on the GDS sub-system

The Grain Detection System of the GIADA PFM was analysed in order to verify its sensitive area. The whole sensitive GDS area was mapped by means of a thin glass needle (\varnothing 4 μm) acting as stimulator to characterize the GDS response. As shown in Figure 50, the glass needle is fastened to the manual handling system allowing a full control on the positioning of the stimulator.

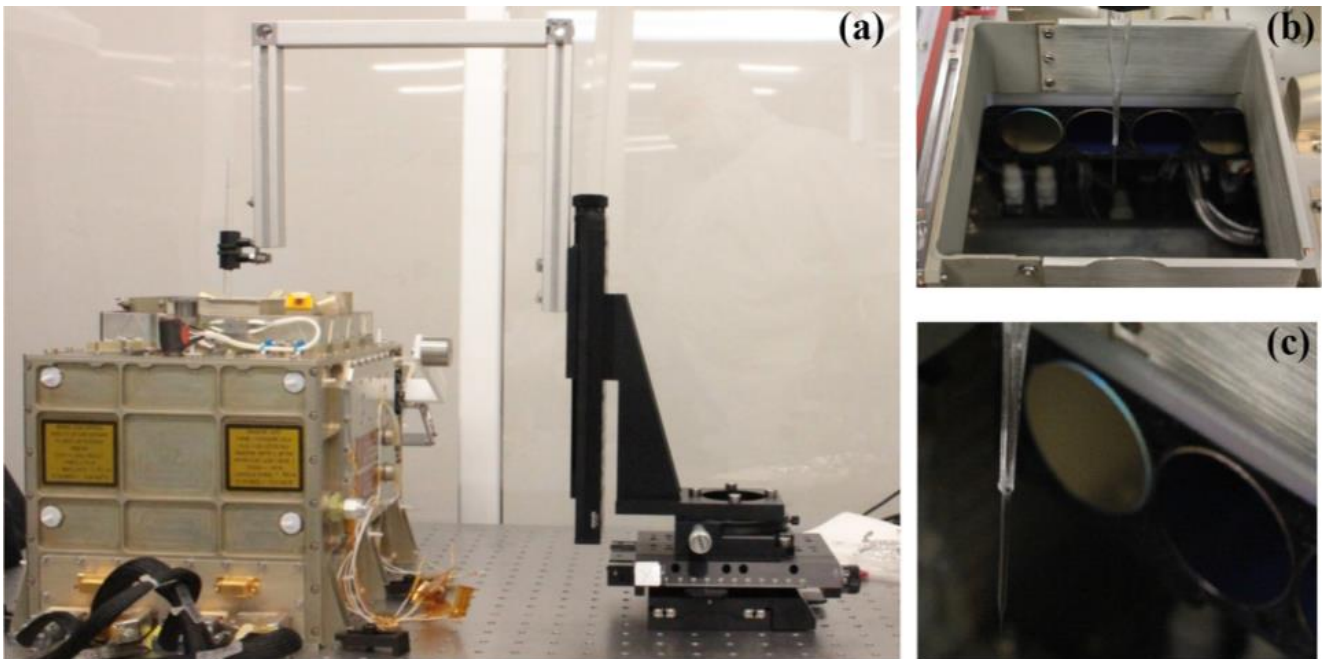


Figure 50: (a) GIADA PFM and the micromanipulator are placed on an optical bench. The GDS sensitive area stimulator is fastened to the micrometric manual handling. (b) The glass needle crossing the laser curtain during the tests performed. (c) a close-up view of the glass needle positioned within the laser curtain.

The mapped area into the GIADA PFM GDS sensitive area is a square of [(13x13)+13] number of points with a 7 mm step; the starting position of the scans is fixed in the reference system (Figure 51) at (7 mm, 7 mm) coordinates. We realized two different “parallel” maps, for each of the GDS receivers (Left and Right), inserting the needle at two different depths within the laser curtain. All the performed tests, described in this chapter, were conducted with the four lasers supplied by a current of $I=0.74A$ (medium power configuration) and pulsed at 100 kHz. The thresholds of the GDS receiver for all the tests were: THR Left = 1.1198 V, THR Right = 0.8781 V.

The test procedure was planned as follow:

1. GDS switched on, the glass needle penetrates into the laser curtain, in the position (14 mm, 21 mm), till when two receivers detect a signal of about 5V, at least. The needle depth within the laser curtain is selected following this criterion.
2. The needle is moved in each of the pre-selected position. For each position we acquired the signal recorded by both the GDS receivers (Left and Right) for about 10 s;

- For each pre-selected position the Left and Right mean values of the signals, recorded during the 10 s acquisition, are taken as the values to be used for the GDS maps.

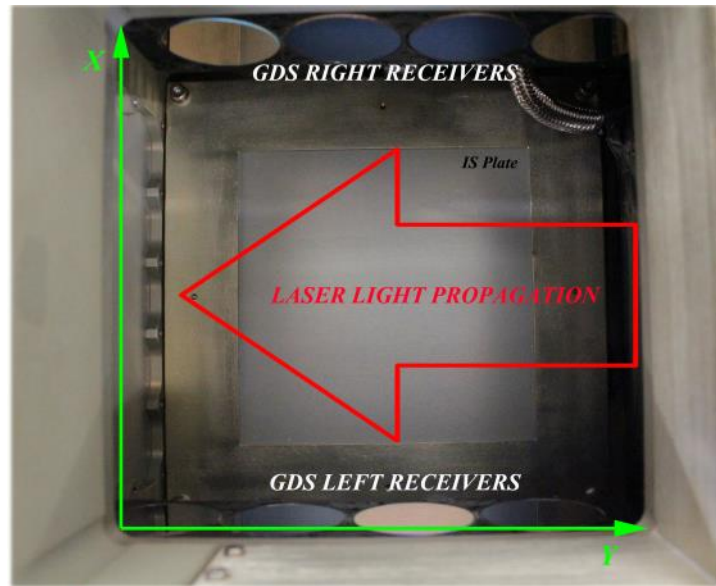


Figure 51: Baffle of GIADA PFM viewed from the top. The picture shows the reference system used in the tests and the direction of the laser propagation.

We obtained, for each GDS receiver (Left and Right), a map of the mean values of the signal scattered from the glass needle and detected by the receivers (Figure 52)

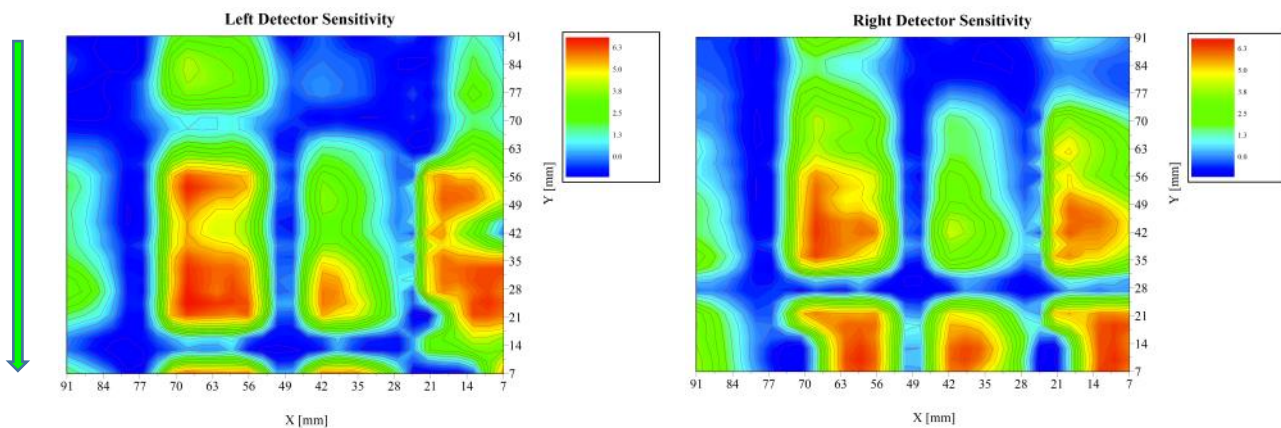


Figure 52: Left Detector Sensitivity map (left panel) and Right Detector Sensitivity map (right panel), obtained by mean of the glass needles acting as stimulator deeply inserted into laser curtain. In blue colour are represent the areas where there are no signal; red areas represent the regions where the signal is saturated (6.9375V). The green arrow on the left shows the direction of the laser propagation.

The false colour maps (Figure 52) shows several red zones, i.e. saturated signal (6.9375V), while the blue areas are related to the regions where the GDS receivers do not detect any signal. The false

colour maps obtained are quite similar to those measured during the pre-flight calibrations on the GIADA in-flight model (Mazzotta-Epifani, 2000).

Given the high number of areas where the signal is saturated present in the first two GDS maps, we decided to run a new scan on the GDS sensitive area using the same pre-selected positions but with a different depth of needle penetration inside the laser curtain (Figure 53). The depth was selected when the registered signal was about 3V in position (14mm, 21mm).

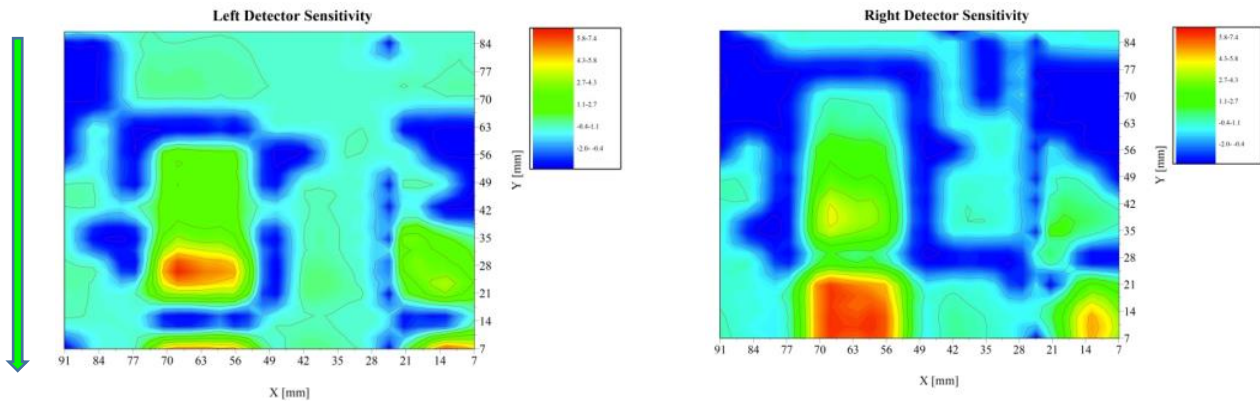


Figure 53: Left Detector Sensitivity map (left panel) and Right Detector Sensitivity map (right panel). The stimulator crosses the laser curtain in order to reduce the saturated areas. Indeed we can notice a great reduction of saturated areas but also an increase of the regions where the signal is not detected. The green arrow shows the direction of the laser propagation.

The sensitivity maps of the two GDS receivers suggested a linear dependence between the detected signal and the needle penetration depth. In order to verify this linear dependence we decided to scan the GDS area along the Z axis. We selected two positions along the propagation of the light emitted by the more intense laser ($x=63$ in Figure 53). Considering the reference system used in our analysis and shown in Figure 51, the selected positions are: Position 1 (63 mm; 28 mm), in front of the second Left Winston Cone, and Position 2 (63 mm; 69 mm), in front of the third Right Winston Cone.

For each position:

1. We identified the lower value of Z where one of the two receivers (Left or Right) started to detect the signal (acquired for about 10s) produced by the stimulator;
2. The scan on Z is performed moving down the glass needle along the Z axis with steps of 50 μm and acquiring the signal for about 10s, for each depth;
3. The scan is stopped when the Left or the Right receiver starts to detect a signal of 0 V, after the plateau at 6.9375V.

The results of these analyses are reported in Figure 54; the plotted values are the means of the 10 s acquisitions signals. As shown in Figure 54, there is a linear dependence between the GDS signal and the penetration depth of the glass needle in the range between the thresholds and the saturation values. The slopes (i.e. the angular coefficients) of these linear trends are different for the two series of receivers. We conclude that there is not uniformity, along the sensitive area, in the response between Left and Right receivers. This only apparently negative aspect can be actually used to improve the information to be retrieved from the GDS measurements. Indeed exploiting the non uniformity response we developed an empirical method that provides information about the grain crossing position within the laser curtain. Such information represents a very important improvement because allow us to identify the areas where the grain transits and to scale the signal using the mean values calculated in a smaller region of the sensitivity map, measured during the pre-flight calibrations. In fact, until now, we had no chance to define the crossing position of a grain entering the GIADA baffle and we had to scale the detected signal considering the mean value of the whole sensitivity maps.

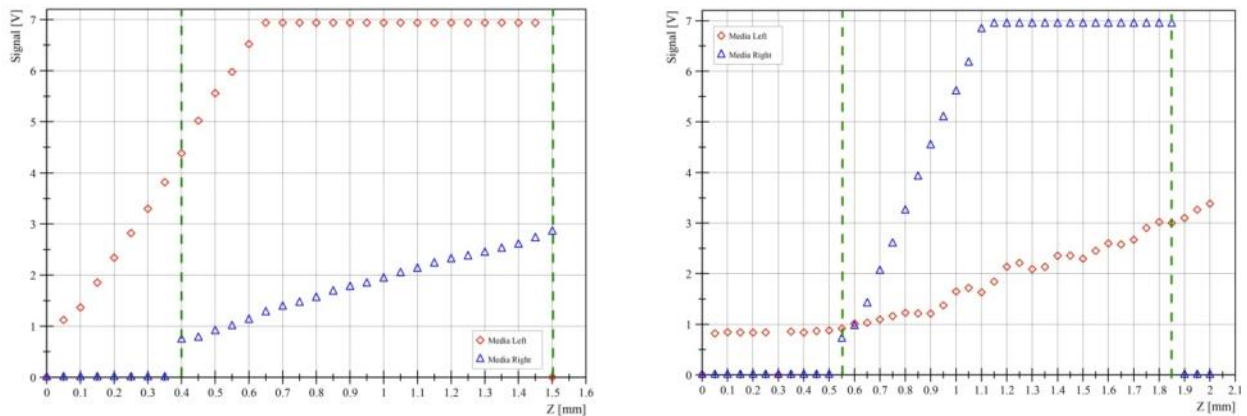


Figure 54: Signal detected by left receivers (red diamonds) and right receivers (blue triangle) vs penetration depth of the glass needle into the laser curtain. Left panel shows signal measured in Position 1 (63mm, 28mm), while the right panel shows the signal measured in Position 2 (63mm,69mm). For each position, we can see that the response curve is a straight line between the thresholds and the saturated values.

The new method is based on the creation of an angular coefficient ratios maps, evaluated for each pre-selected position. When a grain (launched in GIADA PFM or collected by GIADA *in-flight*) is detected by both Left and Right receivers, the ratio between the signals detected by the Left and Right receivers (S_{left}/S_{right}) could give us information on the dust grain crossing positions.

Considering a matrix of 13x12 points, with a step of 7 mm and starting from the position (7 mm,7 mm) we characterized the slopes of the response curves of the Left and Right receivers. In particular, for each (X, Y) position and for each receiver (Left or Right), we acquired the GDS

Minimum and Maximum signal (S_{\min} and S_{\max}) by varying the height Z of the needle and recording the respective values of Z_{\min} and Z_{\max} . We stress here that the acquired S_{\max} has values lower than the saturation limit (6.9375V). For each Z , the signal is acquired for 10 s, and for the analysis we used mean values calculated over the 10 s.

Once obtained S_{\min} and S_{\max} , and the respective Z_{\min} and Z_{\max} , we have calculated the angular coefficients of the straight line passing for Z_{\min} and Z_{\max} , for both GDS receivers: m_{left} and m_{right} . The further step was the estimation of the ratio $m_{\text{left}}/m_{\text{right}}$, for each scanned position: Figure 55 shows how the ratios $m_{\text{left}}/m_{\text{right}}$ spread over the sensitive area of the GDS.

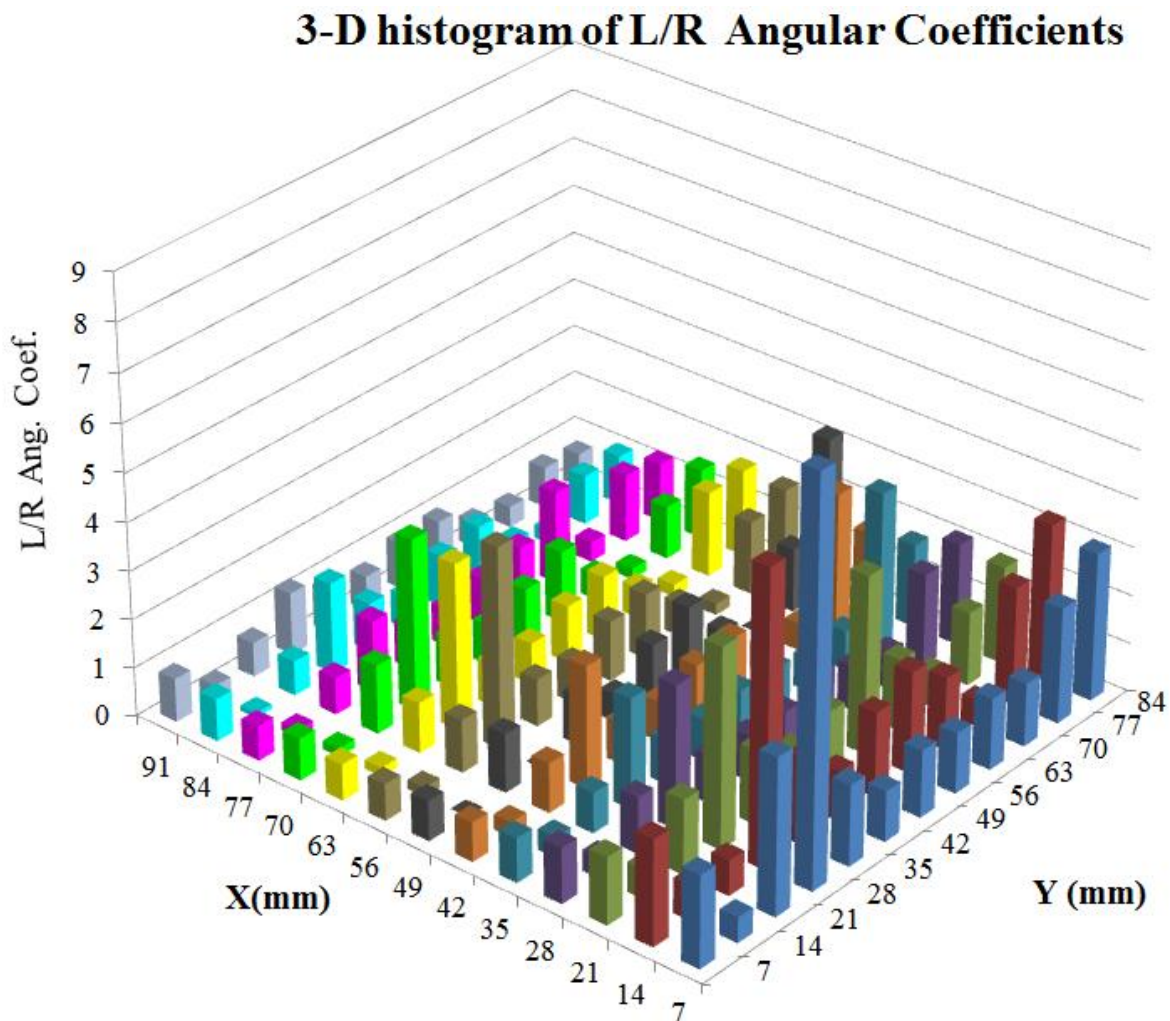
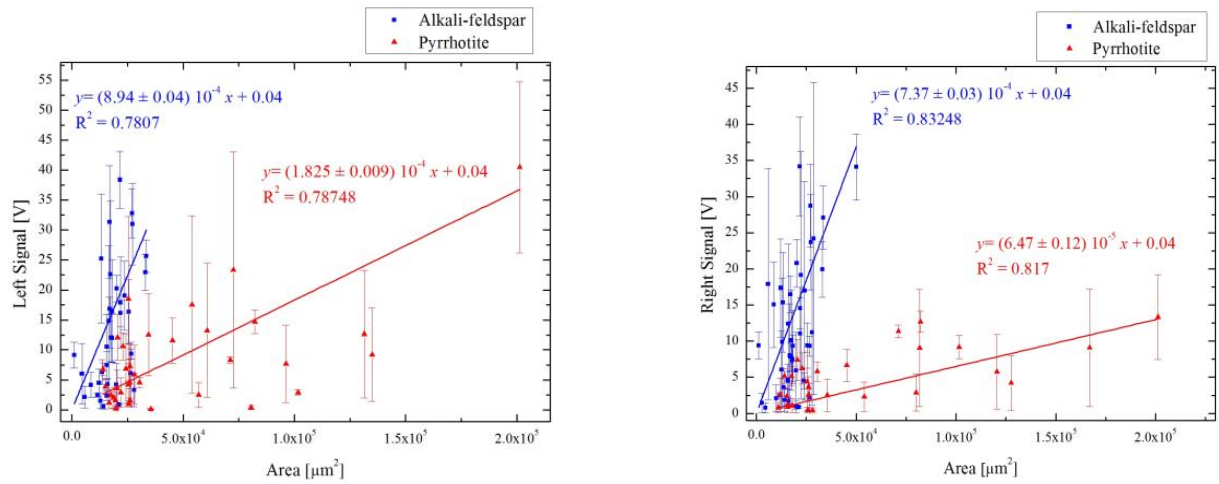


Figure 55: Spread of the ratio $m_{\text{left}}/m_{\text{right}}$, over the GDS sensitive area . For each X-Y position the value of the ratio $m_{\text{left}}/m_{\text{right}}$ is plotted.

5.3 Calibration of GDS using cometary dust analogues

6. After the preparatory activities described above, we performed the calibration of the GDS sub system using the cometary dust analogues reported in (Table 15). The final aim of this activity was to obtain an extended database of subsystem behaviour with respect to the materials that will be crucial for the interpretation of the data collected by GIADA in-flight.
7. During the calibration phase we used the following configuration for the GDS: four lasers supplied by $I=0.74A$ and pulsed at 100 kHz; the thresholds set to THR Left = 1.488V, THR Right =1.244V values.
8. To calculate the calibration curves of the GDS, we used the configuration described in section 4.1.2.
9. The signal detected have been scaled using the sensitivity maps measured during the pre-flight calibration: for particles detected by both GDS receivers we used the L/R Angular Coefficient map (Figure 55) to identify the crossing position, then the signals were scaled considering the mean value of the sensitivity map calculated for the identified positions; for grains detected only by one of the receivers we scaled the signal, considering the whole GDS sensitivity area. In Figure 56 we report the curves obtained for two cometary analogues: the alkali-feldspar and the pyrrhotite. We note that the trend of the two curves, as expected, have different slopes (Table 23). This is due to the different optical properties of the two materials: the alkali-feldspar is a bright material, while the pyrrhotite is a dark material (Figure 57). Indeed the slope of the fit for the bright material is steeper than the one for the dark material: for the Left receivers it is 5 times higher, while in the case of the Right receivers we have even much higher difference up to 11 times. The coefficients of determination R^2 for both receivers show good correlation between the data and the best fit.



11. **Figure 56:** Area vs GDS signal registered for the alkali-feldspar and the pyrrhotite and the relative best fits. The left panel reports the behaviors measured by the Left receivers, while the right panel those measured by the Right receivers.

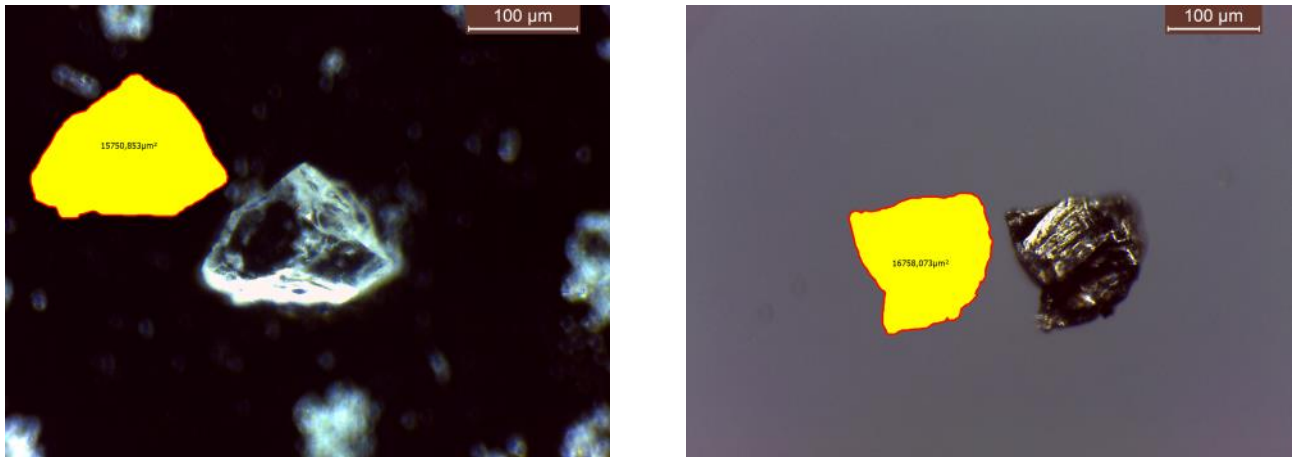


Figure 57: Two images taken with the Leica MC205 Microscope using the Leica IC80HD camera. An alkali-feldspar belonging to the size class 50-100μm with the measured relative area (left) and a pyrrhotite of the 50-100μm size range and its measured relative area (Right).

| <i>Cometary dust Analogues</i> | <i>Best Fit Left</i> | R^2 <i>Left</i> | <i>Best Fit Right</i> | R^2 <i>Right</i> |
|--------------------------------|--|----------------------|--------------------------------------|-----------------------|
| Alkali-feldspar | $y = (8.94 \pm 0.04)10^{-4}x + 0.04$ | 0.78 | $y = (7.37 \pm 0.03)10^{-4}x + 0.04$ | 0.83 |
| Pyrrhotite | $y = (1.825 \pm 0.009)10^{-4}x + 0.04$ | 0.79 | $y = (6.47 \pm 0.12)10^{-5}x + 0.04$ | 0.82 |

Table 23: Results of the best fit calculated for the two selected cometary dust analogues.

In order to obtain the calibration curves, i.e. Signal vs Area, we inverted the best-fit curves obtained during the calibration activity. The obtained calibration curves are given as follows:

| <i>Cometary dust Analogues</i> | <i>Calibration Curves Left</i> | <i>Calibration Curves Right</i> |
|--------------------------------|---|---|
| Alkali-feldspar | $y_1 = (1.12 \pm 0.05)10^3 x_1 - (44.7 \pm 0.02)$ | $y_1 = (1.357 \pm 0.005)10^3 x_1 - (54.2 \pm 0.02)$ |
| Pyrrhotite | $y_2 = (5.48 \pm 0.02)10^3 x_2 - (219 \pm 1)$ | $y_2 = (1.55 \pm 0.03)10^4 x_2 - (618 \pm 11)$ |

Table 24: Calibration Curves for the two selected cometary dust analogues.

The calibration curves are plotted in Figure 58 they show that the discrepancy between the left and right curves for the brighter material (Alkali-feldspar) is much smaller in comparison with the discrepancy in the curves for the darker material (Pyrrhotite).

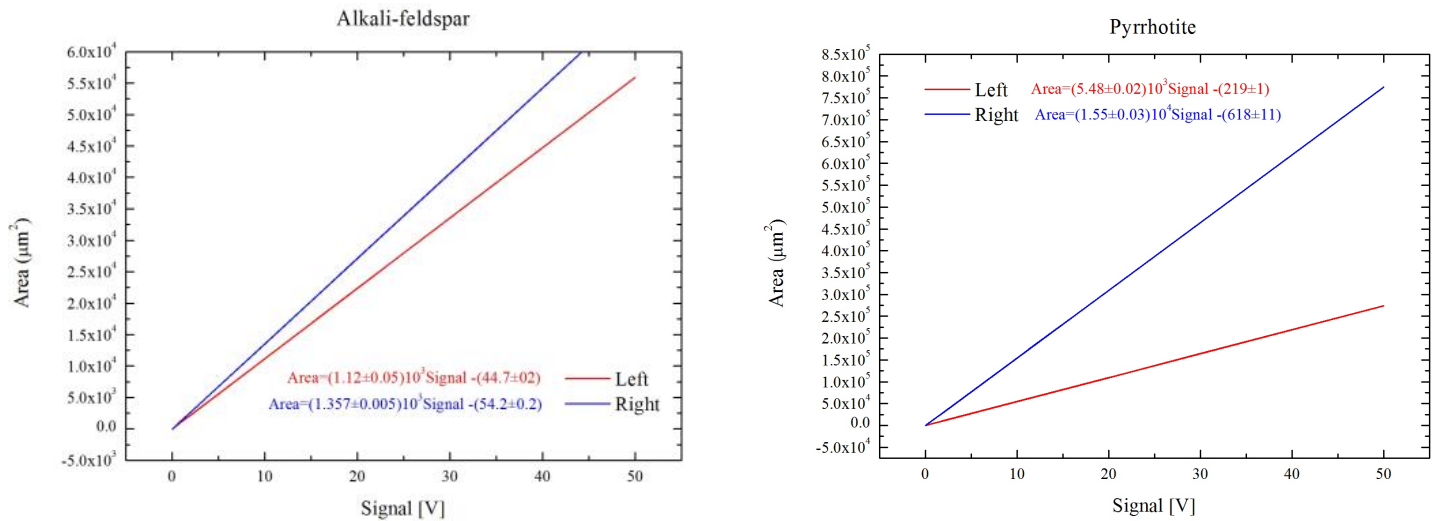


Figure 58: Plots of the Calibration Curves for the Alkali-feldspar (Left) and Pyrrhotite (Right).

Using the additional data provided by other instruments on board of Rosetta, e.g. COSIMA, information on the composition of the grain material can be inferred and therefore integrated with the information of the derived calibration curves will allow us to estimate the area of a grain entering in GIADA *in-flight* with more accuracy.

Utilizing the L/R Angular Coefficients map we improved the accuracy on the valuation of the signal detected by the GDS receivers. In the following we report the results of a test performed with 2 of the particles used for the extended calibration that verifies the improvement in the cross section measurement.

Considering two particles with known area, launched in GIADA during the extended calibration activity, we can demonstrate that, applying the reconstruction technique to scale the signal, leads to a better estimation of the area in comparison with the case obtained without reconstruction (Table 25). We applied the two methodologies of cross section measurement by means of calibration curves. We indicate with “new” the measurement obtained with the identification of the crossing position by means of the angular coefficient ratios and with “old” the measurement obtained without the crossing position reconstruction.

| <i>Material</i> | <i>Measured Area by means of microscope</i> [μm^2] | $S_{left} (new)$ [V] | $S_{right} (new)$ [V] | <i>Evaluated Area</i> _{Left} [μm^2] | <i>Evaluated Area</i> _{Right} [μm^2] |
|-------------------------------|---|----------------------|-----------------------|---|--|
| <i>Pyrrhotite</i> | 82,688 | 14.98±1.92 | 12.7±1.5 | 80,227±10,522 | 196,232±23,250 |
| | | $S_{left} (old)$ [V] | $S_{right} (old)$ [V] | | |
| | | 8.42±7.5 | 10.9±7.5 | 129,892±116,250 | 59,513±50,416 |
| <i>Alkali-feldspar</i> | 16,971 | $S_{left} (new)$ [V] | $S_{right} (new)$ [V] | <i>Evaluated Area</i> _{Left} [μm^2] | <i>Evaluated Area</i> _{Right} [μm^2] |
| | | 16.83±1.96 | 16.49±2.57 | 18,860±2,139 | 22,322±3,487 |
| | | $S_{left} (old)$ [V] | $S_{right} (old)$ [V] | | |
| | | 12.3±10.4 | 11.6±10.3 | 13,371±11,648 | 15,687±13,977 |

Table 25: Estimation of areas starting from the calibration curves.

The results reported in the Table 11 show that:

The new approach to scale the signal detected by the GDS receivers allows a better estimation of the measured area. At least one of the receivers, reaches the exact measured value with less than 10% (Alakali-feldspar) inaccuracy, further analyses will be carried out to investigate if a method to individuate the more reliable measurement between the 2 receivers can be conceived; whereas in the case of non reconstruction of crossing position, the best approximation cannot be better than 30% (Pyrrhotite).

When the measured area is better approximated without reconstruction, the error of this approximation is much higher than in the case with reconstruction. Nevertheless even for example the case of the alkali-feldspar where the old method appeared to be a good evaluation, the error is very high. This confirms the goodness of the n the “new” method proposed here.

6. Conclusions

Cometary activity is the reason of forming a relatively dense coma of dust plus gas and a long dust and plasma tails, which extend for tens of millions of km away from the nucleus. Main aims of past and current comet space missions are: 1) Determining the source of active regions on the nucleus; 2) Studying the link between the circum-nuclear coma (i.e. the unbound, free-expanding gas + dust envelope embedding the nucleus up to distances of about 50 km) and the physico-chemical properties of the nucleus surface (i.e. the coma source); 3) Monitoring cometary activity events, e.g. dust jets, that can give clues on the rotational state of the nucleus and the size distribution of the particles.

The evolution of the coma driven by gas and dust motion can only be well understood by studying the dynamical properties of the dust particles: their velocity, mass, numerical density and size distribution. Despite the results obtained by several space missions on comets, there is still a lack of information on the dust environment in the proximity of the nucleus. There are no direct measurements of dust dynamical properties in the close vicinity of the nucleus, so that any current estimation of the cometary mass losses remains hardly reliable. GIADA, on board the ESA/Rosetta spacecraft, is on its way to fill the gap of missing knowledge on the dynamical properties of cometary dust with its measurements.

Rosetta will encounter comet 67P/CG on May 2014, after a long travel that lasted 10 years. Starting from Rosetta launch and until its hibernation, several periodic payload checkouts were performed in order to verify the instruments health and to execute routinely their maintenance. The data produced by the three GIADA measurement sub-systems (IS, GDS and MBS) during the checkouts were analysed in order to monitor the GIADA health status.

Data analyses have been focused on the most critical elements of GIADA:

- Cover mechanism;
- Measurement sub-systems.

The GIADA Cover is a critical component of the instrument, as its malfunction may compromise GIADA performances. Data analysis of the cover mechanism activations showed some non-nominal behaviour during Commissioning 1, Commissioning 2 and at the end of Payload Checkout 7. During these operations an unexpected behaviour of the mechanism caused partial closures of the Cover. As a consequence three of the five QCMs resulted contaminated by low volatile contaminants probably released by the spacecraft. However, the five QCMs maintained an unaltered nominal sensitivity and functionality. The only minor consequence is that the most

contaminated microbalance, *QCMD*, reduced its theoretical dynamical range of about 2%. We want to stress here that no degradation in the performance of the cover mechanism actually occurred, but rather a slight modification in its behaviour, which since it is now well characterized will not be a major issue. We planned an interactive commissioning devoted to the first Cover activation after the hibernation. This commissioning is scheduled for 6th of April 2014. The results obtained during this test and the Cover behaviour characterized during the cruise phase, will be used to plan the Cover operations for the remaining phases of the mission.

For what concerns the analyses of the GDS and IS GIADA sub systems we reached the following results:

5. The characterization of the light emission for each laser as a function of the temperature.
6. The monitoring of the GDS receivers signal with respect to the Sun-spacecraft relative geometry.
7. The verification of a good stability of the IS PZT sensors with respect to the sensors temperature.

The GDS and IS sub-systems maintained a nominal behaviour with respect to the temperature. Moreover the results obtained for the GDS receivers as a function of the Sun Aspect Angle, allowed us to define the actual operational constraints that will be a reference for the GIADA observation planning.

In preparation to the rendez-vous with the 67P/CG, an extended calibration activity was performed on the GIADA Proto-Flight Model (PFM), operating in a clean room in our laboratory. The work resulted in the achievement of a database of response curves of the GDS and IS sub-systems, which will be used for the analysis of the data that GIADA *in-flight* will collect during the comet phase.

Considering the asteroid-like mineralogy recorded in the Comet Wild 2 samples (Flynn et al., 2006; Zolensky et al., 2006; Keller et al., 2006, Brownlee et al., 2006; Rotundi et al., 2008; Rotundi et al., 2014) and the knowledge obtained by the analysis of Interplanetary Dust Particles (Rietmeijer, 2002), several natural minerals have been selected as cometary dust analogues.. Single grains of these selected materials, with diameter ranging from 20 μm to 500 μm , were shot into the GIADA PFM with velocities in the range 1-100 ms^{-1} , i.e. the expected velocities for cometary grains emitted from a nucleus. In order to facilitate and speed up the calibration on the GIADA PFM, an innovative Electrostatic Micromanipulator was designed and assembled. The tests performed on this device have confirmed its proper functioning, demonstrating its capability to shoot particles in the range (250÷500) μm with velocities $v_{\text{GDS}} = (1\div 20) \text{ms}^{-1}$. To launch particle smaller than

250 μm , with higher velocity, a compressed air gun, already used during the pre-flight calibrations, was used..

A series of tests were performed on the GDS and IS sub systems, in order to verify the systems responsivity as a function of fixed stimulus.

The analyses performed using the IS internal calibrator demonstrated that PZT2 mounted on GIADA PFM is affected by *cross talk*. From the analyses of the time delays measured during the Cruise Phase, resulted evident that this effect occurs also on the PZT2 mounted on the GIADA *in-flight* Model, this behaviour will be verified by dedicated session during the GIADA re-commissioning. The tests performed on the whole sensitive plate of the IS, using spherical glass particles of 500 μm , allowed us to create a dataset that links the time delays measured by each PZTs to a defined position (X, Y). Using this database and the IS sensitivity map, calculated during the pre-flight calibration, a new empirical method was developed to reconstruct the impact position. This new method allows us to improve the precision of the impact position reconstruction: it is able to identify the 68% of the impact positions, within an error of 2.5 cm, really a positive results, especially when compared to the 24% reached with the analytical method used during the pre-flight calibrations.

The study of the GDS sensitive area, depicted in Chapter 4, highlighted a non-uniform response of the two GDS receivers (Left and Right) vs a fixed stimulus. In particular, we verified that in each tested position of the illuminated area of the GDS the response of each receiver has a linear behaviour vs stimulus magnitude, but with different slopes. We studied this apparently negative aspect creating a map of the ratios between the Angular Coefficients obtained from the receivers' response to fixed stimuli. This map allows us, in case of a grain detected by both receivers, to identify a small region in which the grain crosses the GDS sensitive area. In this way the detected signal can be scaled using the mean values of the sensitivity maps calculated in this small region, reducing the uncertainty on the signal. Previously we had no chance to define the crossing positions of a grain entering into GIADA and accordingly we had to scale the detected signal considering the mean values and relative standard deviations of the whole sensitivity maps.

The calibration with cometary dust analogue grains was performed on the GDS sub-system. The experimental curves Area (particle cross section) vs GDS Signal were obtained for both GDS receivers (Left and Right) using different cometary dust analogue grains. The best-fit parameters of a linear regression are reported in Table 9.

| <i>Cometary dust Analogues</i> | <i>Best Fit Left</i> | <i>R² Left</i> | <i>Best Fit Right</i> | <i>R² Right</i> |
|--------------------------------|--|---------------------------|--------------------------------------|----------------------------|
| Alkali-feldspar | $y = (8.94 \pm 0.04)10^{-4}x + 0.04$ | 0.7807 | $y = (7.37 \pm 0.03)10^{-4}x + 0.04$ | 0.83248 |
| Pyrrhotite | $y = (1.825 \pm 0.009)10^{-4}x + 0.04$ | 0.78748 | $y = (6.47 \pm 0.12)10^{-5}x + 0.04$ | 0.817 |

Table 23: Results of the best-fit calculated for two selected cometary dust analogues.

The trends of the two curves, as expected, have different slopes; this is due to the different optical properties of the two materials used: the alkali-feldspar is a bright material, while the pyrrhotite is a dark material. The coefficients of determination R^2 for both receivers show good correlation between the data and the best-fit.

The calibration curves Signal vs Area, are obtained by inverting the best-fit curves estimated during the calibration activity. The obtained calibration curves are reported in Table 10:

| <i>Cometary dust Analogues</i> | <i>Calibration Curves Left</i> | <i>Calibration Curves Right</i> |
|--------------------------------|--|--|
| Alkali-feldspar | $y_1 = (1.12 \pm 0.05)10^3x_1 - (44.7 \pm 0.02)$ | $y_1 = (1.357 \pm 0.005)10^3x_1 - (54.2 \pm 0.02)$ |
| Pyrrhotite | $y_2 = (5.48 \pm 0.02)10^3x_2 - (219 \pm 1)$ | $y_2 = (1.55 \pm 0.03)10^4x_2 - (618 \pm 11)$ |

Table 24: Calibration Curves for the two selected cometary dust analogues.

The evaluated calibration curves, combined with the auxiliary data on composition provided by other instruments on board Rosetta, e.g. COSIMA, will allow us to better estimate the grain area and consequently the size of a grain entering into GIADA *in-flight*.

Using the L/R Angular Coefficients map we considerably improved the accuracy on the valuation of the signal detected by the GDS receivers. Considering a particle with known area launched in GIADA PFM during the extended calibration activity we have demonstrated that, applying the reconstruction technique to scale the signal, a better estimation of the area was achieved with respect to the case obtained without reconstruction.

In conclusion, the work performed in the framework of my PhD course, described in this thesis, resulted in a significant improvement on the measurement accuracy of the GIADA sub systems.

All the results obtained with this work will be critical for the interpretation of the data that will be collected by GIADA *in-flight* during the scientific phase of the mission.

7. REFERENCES

1. **Aronica A.**, “La missione ROSETTA: Analisi dei dati di GIADA in volo durante la fase di crociera”, *PhD thesis, University “Federico II” of Naples*, **2009**.
2. **Barber P.W., Hill S.C.**, “Light scattering by particles: computational methods”, *World Scientific Publishing Co. Pte. Ltd.*, Singapore, **1990**.
3. **Belyaev N.A., Kresak L., Pittich E.M., Pushkraev A.N.**, “ Catalogue of Short-Period Comets”, *Astron. Inst. Slovak Academy of Sciences*, Bratislava, **1986**.
4. **Bessel F. W.**, Bemerkungen über mögliche Unzulänglichkeiten der die Anziehungen allein berücksichtigenden Theorie der Kometen. Von Herrn Geheimen-Rath u Ritter Bessel. *Astron. Nachr.*, 13, 345–350, **1836**.
5. **Bibring J.P., Rosenbauer H., Boehnhardt H., et al.**, “The ROSETTA Lander PHILAE investigations”, *Space Sci. Rev.*, vol.128, pp.205-220, **2007**.
6. **Biermann L.**, Kometenschweife und solare Korpuskularstrahlung. *Z. Astrophys.*, 29, 274–286, **1951**.
7. **Bohren C.F., Huffman D.R.**, “Absorption and scattering of light by small particles”, *John Wiley & Sons, inc.*, New York, **1983**.
8. **Bonnet R.M.**, “The New Mandatory Scientific Programme for ESA”, *ESA Bulletin* 43, 8-13, **1985**.
9. **Brownlee D., Tsou P., Aléon J., et al.**, “Comet 81P/Wild 2 Under a Microscope”, *Science*, Vol.314, no. 5806, pp.1711-1716, December 15, **2006**.
10. **Clapp S. S.**, *Air Force Cambridge Research Laboratories Report*, AFCRL-64-98, **1963**.
11. **Colangeli L., Lopez Moreno J.J., Palumbo P., et al.**, in *ROSETTA ESA’s Mission to the Origin of the Solar System*, Eds. Schulz, R., Alexander, C., Boehnhardt, H. & Glassmeier, K. H. (Springer), pp. 243, **2009**.
12. **Colangeli L., Lopez-Moreno J.J., Palumbo P., et al.** “The Grain Impact Analyser and Dust Accumulator (GIADA) Experiment for the Rosetta Mission: Design, Performances and First Results”, *Space Science Reviews*, vol.128, issue 1-4, pp.803-821, **2007**.
Comets II, Eds. M. C. Festou, H. U. Keller, H. A. Weaver. University of Arizona
13. **Della Corte V., Rotundi A., Accolla M., Sordini R., et al.**, “GIADA: its status after the ROSETTA cruise phase and on-ground activity in support of the encounter with comet 67p/Churyumov-Gerasimenko”, *Journal of Astronomical Instrumentation* 1350011, pp.11, doi: 10.1142/S2251171713500116, **2014**.
14. **Doody D., Stephan G.**, “Basics of space flight”, *Diane Fisher Ed.*, 2013 Edition, Section 1, Chap. 1, <http://www2.jpl.nasa.gov/basics/bsf1-3.php>, **1993**.
15. **Duncan M.J., Levison H.F., Dones L.**, “Dynamical Evolution of Ecliptic Comets”,

16. **Esposito F.**, “Il Sensore d’Impatto dello strumento GIADA per la misura della quantità di moto di grani cometari dalla sonda spaziale ESA ROSETTA”, *PhD thesis, University “Federico II” of Naples*, 2001.
17. **Esposito F.**, Colangeli L., Della Corte V., et al., “Physical aspect of an “impact sensor” for the detection of cometary dust momentum onboard the “Rosetta” space mission”, *Adv. Space Res.* 29, 1159-1163, **2002**.
18. **Farinella P., Davis D.R.**, “Short-period comets: Primordial bodies or collisional fragments?”, *Science*, vol.273, pp.938-941, **1996**.
19. **Ferrari M.**, Della Corte V., Rotundi A., Rietmeijer F.J.M., “Single minerals, carbon- and ice-coated single minerals for calibration of GIADA onboard ROSETTA to comet 67P/Churyumov-Gerasimenko”, *Planetary and Space Science*, (under review), **2014**.
20. **Festou M.C.**, Keller H.U., Weaver H.A., “A brief conceptual history of cometary science”, *Comets II*, M. C. Festou, H. U. Keller, and H. A. Weaver (eds.), University of Arizona Press, Tucson, 745, pp.3-16, **2004**.
21. **Fink U., Rubin M.**, “The calculation of $A f \rho$ and mass loss rate for comets”, *Icarus* 221, pp.721-734, **2012**.
22. **Flynn G.J.**, et al., “Elemental Compositions of Comet 81P/Wild 2 Samples Collected by Stardust”, *Science*, vol.314, issue 5806, pp.1731-1735, December 15, **2006**.
23. **Fulle M.**, Colangeli L., Agarwal J., Aronica A., Della Corte V., Esposito F., E. Grün, M. Ishiguro, R. Ligustri, J. J. LopezMoreno, E. Mazzotta Epifani, G. Milani, F. Moreno, P. Palumbo, J. Rodríguez Gómez, A. Rotundi, “Comet 67P/Churyumov-Gerasimenko: the GIADA dust environment model of the Rosetta mission target”, *Astronomy and Astrophysics*, Vol. 522, id.A63, **2010**.
24. **Grewing M.**, Praderie F., Reinhard R., “*Exploration of Halley's Comet*”, Springer-Verlag, 1988 investigations. *Space Sci. Rev.*, Vol.128. pp.205–220, **1988**.
25. **Grün E.**, Staubach P., Baguhl M., Hamilton D.P., Zook H.A., Dermott S., Gustafson B.A., Fechtig H., Kissel J., Linkert D., Linkert G., Srama R., Hanner M.S., Polanskey C., Horanyi M., Lindblad B.A., Mann I., McDonnell J.A.M., Morfill G.E. and Schwehm G., “South-North and Radial Traverses through the Interplanetary Dust Cloud”, *Icarus*, 129:270-288, **1997**.
26. **Ishiguro M.**, “Cometary dust trail associated with Rosetta mission target: 67P/Churyumov-Gerasimenko”, *Icarus* 193, pp.96-104, **2008**.
27. **Jewitt D., Luu J.**, “Discovery of the candidate Kuiper belt object 1992 QB₁”, *Nature* 362, 730-732, doi:10.1038/362730a0, April 22, **1993**.
28. **Kawamoto H.**, “Manipulation of single particles by utilizing electrostatic force”, *Journal of Electrostatics*, vol. 67, pp. 850–861, **2009**.

29. **Keller H. U.**, Kramm R., Thomas N., “Surface features on the nucleus of Comet Halley”, *Nature*, vol.331, pp.227–231, **1988**.
30. **Keller L.P.**, et al., “Infrared Spectroscopy of Comet 81P/Wild 2 Samples Returned by Stardust”, *Science*, vol.314, issue 5806, pp.1728-1731, **2006**.
31. **Kelley M. S.**, Wooden D.H., Tubiana, C., et al., “Spitzer Observations of Comet 67P/Churyumov-Gerasimenko at 5.5-4.3 AU from the Sun” *The Astronomical Journal*, vol.137, issue 6, pp.4633-4642, **2009**.
32. **Lamy P.L.**, Davidsson B.J.R., Groussin O., Gutierrez P., Jorda L., Kaasalainen M., Lowry S. and Toth, I., “A Portrait of the Nucleus of Comet 67P/Churyumov-Gerasimenko”, *Space Science Reviews*, 128 (1-4), pp.23-66, **2007**.
33. **Lamy, P.L.**, Toth, I., Davidsson, B.J.R., et al. “The nucleus of Comet 67P/Churyumov-Gerasimenko”, in *Rosetta. ESA’s mission the Origin of the Solar System*, ed. R. Schulz, C. Alexander, H. Boehnhardt, & K. H. Glassmeier (Springer), **2009**.
34. **Landau L.D., Lifšits E.M.**, “Theory of elasticity”, Theoretical Physics Vol. 7, **1995**.
lichkeit der die Anziehungen allein berücksichtigenden Theorie der Kometen. Von Herrn Geheimen-Rath u Ritter Bessel. *Astron. Nachr.*, 123, 345-350, **1836**.
35. **Lucarelli F.**, “Sviluppo di software dedicati alla previsione delle prestazioni e all’interpretazione dei dati scientifici di strumenti per missioni spaziali: applicazione all’ambiente di polvere cometario per la missione dell’Agenzia Spaziale Europea, Rosetta”. *Master Degree thesis, University “Parthenope” of Naples*, **2013**.
36. **Mazzotta-Epifani E.**, “La missione spaziale ROSETTA verso la cometa 46P/Wirtanen: sviluppo, realizzazione e test del sistema di rivelazione grani GDS per lo strumento GIADA”, *PhD thesis, University “Federico II” of Naples*, **2000**.
37. **Mazzotta-Epifani E.**, Bussoletti E., Colangeli L., et al., “The grain detection system for the GIADA instrument: design and expected performances”, *Adv. Space Res.* 29, pp.1165-1169, **2002**.
38. **McDonnell J.A.M.**, “Calibration studies on a piezoelectric sensing diaphragm for the detection of micrometeorites in space”, *Journal of Scientific Instruments (Journal of Physics E)*, 2, Series 2, **1969**.
39. **Morbidelli A., Brown M.E.**, “The Kuiper Belt and the Primordial Evolution of the
40. **Morbidelli A., Brown M.E.**, “The Kuiper Belt and the Primordial Evolution of the
of Arizona Press, Tucson, p. 175–191, **2004**.
41. **Oort J. H.**, “The structure of the cloud of comets surrounding the solar system and a hypothesis concerning its origin”, *Bull. Astr. Inst. Netherl.*, 11, 91–110, **1950**.
42. **Palomba E.**, Colangeli L., Palumbo P., et al., “Performance of microbalances for dust flux measurement”, *Adv. Space Res.* 29, 1155-1158, **2002**.
43. **Rayman M.D.**, “The successful conclusion of the Deep Space 1 Mission: important results without a flashy title”, *Space Technology* 23, pp185–196, **2003**.

44. **Reinhard R.**, “The Giotto Encounter with Comet Halley”, *Nature*, 321:313-318, **1986**.
45. **Rietmeijer F.J.M.**, “The earliest chemical dust evolution in the solar nebula”, *Chemie der Erde*, 62, 1-45, **2002**.
46. **Rietmeijer, F.J.M.**, Nuth III, J. A., “Grain sizes of ejected comet dust: Condensed dust analogs, interplanetary dust particles and meteors”, *Colangeli, L., Mazzotta Epifani, E., Palumbo, P. (eds.), The New ROSETTA Targets - Observation, simulations and instrument performances. Astrophys. Space Sci. Library, Kluwer Academic Publishers*, pp.97-110, **2004**.
47. **Rotundi A.**, Rietmeijer F.J.M., “Carbon in Meteoroids: Wild 2 Dust Analyses, IDPs and Cometary Dust Analogues”, *Earth Moon Planet. Springer Science + Business Media*, doi 10.1007/s11038-007-9218-7, **2008**.
48. **Rotundi A.**, Rietmeijer F.J.M., Ferrari M., Della Corte V., Baratta G.A., Brunetto R., Dartois E., Djouadi Z., Merouane S., Borg J., Brucato J.R., Le Sergeant d’Hendecourt L., Mennella V., Palumbo M.E., Palumbo P., “Two refractory Wild2 terminal particles from a carrot-shaped track characterized combining MIR/FIR/Raman micro-spectroscopy and FE-SEM/EDS analyses”, *Meteoritics & Planetary Science*, doi: 10.1111/maps.12274, **2014**.
49. **Schläppi B.**, Altwegg K., Balsiger H., et al., “Influence of spacecraft outgassing on the exploration of tenuous atmospheres with in situ mass spectrometry”, *Journal of Geophysical Research*, vol.115, A12313, doi: [10.1029/2010JA015734](https://doi.org/10.1029/2010JA015734), **2010**.
50. **Sengoku A.**, “On lunar gravitaitonal potential recovery from SELENE satellites”, *Proc. 30th Symposium on Celestial Mechanics*, 30, 131–136, **1998**.
51. **Snodgrass C.**, Meech K., Hainaut O., “The nucleus of 103P/Hartley 2, target of the EPOXI mission”, *Astronomy & Astrophysics*, Vol.516, pp.4, doi: [10.1051/0004-6361/201014790](https://doi.org/10.1051/0004-6361/201014790), June **2010**.
Solar System”, *Comets II, Eds. M. C. Festou, H. U. Keller, H. A. Weaver. University*
52. **Vincent J.B.**, Lara L.M., Tozzi G.P., Lin Z.Y., Sierkes H., “Spin and activity of comet 67P/Churyumov-Gerasimenko”, *Astronomy & Astrophysics*, 549, A121, doi: 10.1051/0004-6361/201219350, **2013**.
53. **Von Rosenvinge T.T.**, Brandt J.C., Farquhar R.W., “ International Cometary Explorer mission to comet Giacobini-Zinner”, *Science*, vol.232, no.4748, pp.353-356, April 18, **1986**.
54. **Weaver H. A.**, A’Hearn M.F., Arpigny C., Boice D.C., Feldman P.D., Larson S.M., Lamy P., Levy D.H., Marsden B.G., Meech K.J., Noll K.S., Scotti J.V., Sekanina Z., Shoemaker C.S., Shoemaker E.M., Smith T.E., Stern S.A., Storrs A.D., Trauger T., Yeomans D.K., Zellner B., “The Hubble Space Telescope observing campaign on comet P/Shoemaker-Levy 9”, *Science*, Vol. 267, **1995**.
55. **Weissman P.R.**, Asphaug E., Lowry S.C., Structure and Density of Cometary Nuclei”, *Comets II, Part IV: The Nucleus*, Michel Festou, H. Uwe Keller, and Eds., University of Arizona Press, pp.337-357, **2004**.

56. **Weissman P.R.**, Stern S.A., “Physical processing of cometary nuclei”, *Workshop on Analysis of Returned Comet Nucleus Samples*, S. Chang, ed., pp.119–166. NASA CP- 10152, Washington, DC, **1998**.
57. **Welford W.T., Winston R.**, “High collection nonimaging optics”, *Academic Press, Inc.*, San Diego, California (US), **1989**.
58. **Whipple F.L.**, “A Comet Model I. The Acceleration of Comet Encke”, *Astrophysical Journal* 111, 375-394, **1950**.
59. **Winston R.**, “Light collection within the framework of geometrical optics”, *JOSA*, 60, 2, 245, **1970**.
60. **Wissler S.**, Rocca J., Kubitschek D., “Deep Impact comet encounter: design, development and operations of the big event at Tempel 1”, *Pasadena, CA: Jet Propulsion Laboratory, National Aeronautics and Space Administration*, **2005**.
61. **Wurm K.**, “Die Natur der Kometen”, *Mitt. Ham. Sternwarte* 8, no.51, **1943**.
62. **Zolensky M.E.**, et al., “Mineralogy and Petrology of Comet 81P/Wild 2 Nucleus Samples”, *Science*, vol.314, issue 5806, pp.1735-1739, **2006**